

# Combined Study of Local Spectroscopy and Macroscopic Electronic Transport of the Correlated Honeycomb Spin-Orbit Mott Insulator $\text{Na}_2\text{IrO}_3$

Dissertation

zur Erlangung des mathematisch-naturwissenschaftlichen Doktorgrades

"Doctor rerum naturalium"

der Georg-August-Universität Göttingen

im Promotionsstudiengang Physik

der Georg-August University School of Science (GAUSS)

vorgelegt von

**Thomas Engelbert Dziuba**

aus Gehrden

Göttingen, 2021

### **Betreuungsausschuss**

PD Dr. Martin Wenderoth

IV. Physikalisches Institut, Georg-August-Universität Göttingen

Prof. Dr. Philipp Gegenwart

Experimentalphysik VI, Universität Augsburg

Prof. Dr. Stefan Mathias

I. Physikalisches Institut, Georg-August-Universität Göttingen

### **Mitglieder der Prüfungskommission**

Referent: PD Dr. Martin Wenderoth

IV. Physikalisches Institut, Georg-August-Universität Göttingen

Korreferent: Prof. Dr. Stefan Mathias

I. Physikalisches Institut, Georg-August-Universität Göttingen

### **Weitere Mitglieder der Prüfungskommission**

Prof. Dr. Philipp Gegenwart

Experimentalphysik VI, Universität Augsburg

Prof. Dr. Hans-Christian Hofsäss

II. Physikalisches Institut, Georg-August-Universität Göttingen

PD Dr. Salvatore Manmana

Institut für Theoretische Physik, Georg-August-Universität Göttingen

Prof. Dr. Michael Seibt

IV. Physikalisches Institut, Georg-August-Universität Göttingen

Tag der mündlichen Prüfung: 14. Oktober 2021



## Inhalt

1	Introduction.....	1
2	Bulk Sodium Iridate: Structural and Electronic Properties.....	3
2.1	Bulk Crystal Structure.....	3
2.2	Bulk Electronic Structure.....	4
2.2.1	Crystal Field Splitting and Trigonal Distortion in $\text{Na}_2\text{IrO}_3$ .....	5
2.2.2	Spin-Orbit Coupling in $\text{Na}_2\text{IrO}_3$ .....	7
2.2.3	Hubbard Repulsion in $\text{Na}_2\text{IrO}_3$ .....	8
2.3	Experimental Findings on the Bulk Mott Gap of $\text{Na}_2\text{IrO}_3$ .....	11
3	Sodium Iridate Surface: Structural and Electronic Properties.....	13
3.1	$\text{Na}_2\text{IrO}_3$ Surface Structure.....	13
3.2	Topology and Topologically Protected Conductive States in Solids.....	15
3.3	Theoretical Predictions of Non-Trivial Topology for $\text{Na}_2\text{IrO}_3$ .....	18
3.4	$\text{Na}_2\text{IrO}_3$ Surface Electronic Properties.....	21
4	Supplementary Experimental Data of $\text{Na}_2\text{IrO}_3$ .....	25
4.1	Electronic Transport Properties of the $\text{Na}_2\text{IrO}_3$ Bulk.....	25
4.2	Chemical Instability of $\text{Na}_2\text{IrO}_3$ in Air.....	26
4.3	Surface Modification due to Effusion of Na from the $\text{Na}_2\text{IrO}_3$ Bulk to the Surface.....	27
5	Introduction to the Experimental Methods.....	28
5.1	Sample Synthesis of $\text{Na}_2\text{IrO}_3$ .....	28
5.2	Sample Pre-Characterization via XRD and SQUID.....	29
5.3	Sample Preparation.....	30
5.3.1	Sample Preparation for STM Measurements.....	31
5.3.2	Sample Preparation for Transport Measurements.....	31
5.4	Crystal Cleaving.....	33
5.5	Scanning Tunnelling Microscopy.....	34
5.5.1	STM Theory.....	35
5.5.2	Role of the STM Tip Orbital.....	37
5.5.3	Constant Current Topography.....	38
5.5.4	Scanning Tunnelling Spectroscopy.....	39
5.5.5	Barrier Height Spectroscopy.....	40
5.5.6	Experimental STM Setup.....	41
5.5.7	STM Measurement Electronics.....	42
5.6	Transport Measurements.....	43
5.7	Applicable Transport Phenomena.....	45

5.7.1	Metallic Conduction .....	46
5.7.2	Electrical Transport in Semiconductors and Mott Insulators.....	47
5.7.3	Hopping Conduction and Variable Range Hopping .....	50
5.7.4	Effect of Electron-Electron Correlation on Variable Range Hopping .....	53
5.7.5	Transport Properties of Topologically Protected Boundary States.....	54
6	Scanning Tunnelling Microscopy and Spectroscopy on the Freshly Cleaved Na <sub>2</sub> IrO <sub>3</sub> Surface.....	57
6.1	The Chemical Stability on the Na <sub>2</sub> IrO <sub>3</sub> Surface in UHV and In-Situ Modifications of the STM Tip	57
6.2	Impact of Tip Modifications on the dI/dV-Spectra Taken on the Na <sub>2</sub> IrO <sub>3</sub> Surface.....	64
6.3	Generic Spectral Types Found on the Na <sub>2</sub> IrO <sub>3</sub> Surface .....	71
6.3.1	Spectral Type 1 – Open Spectral Gap .....	72
6.3.2	Spectral Type 2 – Symmetric In-Gap States .....	76
6.3.3	Spectral Type 3 – Linear Band Gap Closing .....	80
6.4	Robustness of the Surface In-Gap States .....	88
6.5	STM Measurements on Na <sub>2</sub> IrO <sub>3</sub> at 8 K Using Optically Excited Charge Carriers.....	89
7	Macroscopic Transport Measurements .....	93
7.1	Electronic Transport of Uncleaved Na <sub>2</sub> IrO <sub>3</sub> .....	93
7.2	Discussion of the Na <sub>2</sub> IrO <sub>3</sub> Bulk Electronic Properties in the Context of STM/STS and Transport Measurements.....	103
7.3	Conductance of the Freshly Cleaved Na <sub>2</sub> IrO <sub>3</sub> Surface .....	106
7.4	The Effect of Air Dosing on the Surface Conductance .....	111
8	Discussion of the Na <sub>2</sub> IrO <sub>3</sub> Surface Electronic Properties in the Joint Context of STM/STS and Transport Measurements.....	114
9	Summary and Outlook.....	118
10	Bibliography.....	121
11	Danksagung .....	129
12	Curriculum Vitae.....	130

# 1 Introduction

The search for novel phenomena that exceeds and interconnects our existing knowledge is at the heart of every scientific effort. Physics, and particularly solid-state research, is no exception. If anything, the technological advancements of the last decades have made the need for new concepts even more apparent. A prototypical example here is the beginning breakdown of Moore's law in the semiconductor industry, where electronic components shrunk down to a few nanometres in size. This greatly enhanced the performance of, e.g., integrated circuits, but leads to a dead end since the further shrinking of structures is inhibited by their instability on a nanoscale [1], [2]. Such an issue cannot be solved by engineering efforts alone since it is the very physics that blocks the way. In the foreseeable future, disruptive technological advancement will rely on new physical concepts as a basis, and current efforts in solid-state physics research reflect this, as considerable resources are assigned to the study of phenomena that are yet described as "exotic".

One of such novel phenomena is the existence of non-trivial topological phases of matter. Theoretically proposed by Haldane in 1988 [3], [4], the concept of topology lied mostly dormant until 2007, when König et al. identified HgTe quantum wells as the first real world system with non-trivial topology [5], [6]. Besides the interesting implications for fundamental research, the emergence of the so-called bulk-boundary correspondence (BBC) from non-trivial topology initiated an ever-growing research field within the physics community. The BBC enforces a conductive channel at the interface between a topologically trivial and a non-trivial material, in which electron backscattering is prohibited [3]–[8], yielding robust metallic conductance independently of defects and local structural instabilities. This potentially opens a pathway for completely new concepts in (micro-) electronics.

To this day, all experimentally confirmed topologically non-trivial materials either have an exceedingly small bulk band gap [9], rendering them uninteresting for technological applications since a substantial share of the overall electric current would flow though the bulk, diminishing the advantages of the topologically protected interface conductance, or exhibit microscopic sample sizes like bismuthene on SiC substrates [10]. Additionally, all experimentally found topological insulators are band-insulators [9], [11].

The honeycomb transition metal oxide sodium iridate ( $\text{Na}_2\text{IrO}_3$ ) is a promising material in this context, as it exhibits a band gap (Mott gap) comparable to the band gaps of common semiconductors and a rich variety of proposed and experimentally reported electronic and magnetic properties [12]–[20]. Among the anticipated properties is the emergence of a non-trivial topological phase, which was first proposed in 2009 [21]. This prediction was reinforced

several times, with the latest according work being published in 2019 [22]–[25]. The Mott gap arises from concurrent crystal field splitting, spin-orbit coupling and Hubbard repulsion apparent on similar energy scales in the material, making  $\text{Na}_2\text{IrO}_3$  a strongly correlated Mott insulator. Non-trivial topology would render  $\text{Na}_2\text{IrO}_3$  to be the first topological insulator with a large energy gap as well as the first strongly correlated topological insulator. Combined with sample diameters of up to 1 cm, the material would be interesting for technological application. Yet, after more than a decade of research, the experimental findings on the  $\text{Na}_2\text{IrO}_3$  electronic structure are largely incoherent, where even the reported Mott gap size varies between 0.34 eV and 1.2 eV [18], [26]–[29] and the role of the surface with its different terminations is poorly understood.

This thesis provides a comprehensive study of the electronic properties of  $\text{Na}_2\text{IrO}_3$ , focusing on its surface. For this, scanning probe and transport measurements on freshly cleaved samples were performed in ultra-high vacuum (UHV). The new findings yield insights to a variety of disputed properties of  $\text{Na}_2\text{IrO}_3$ , including the spectral characteristics at the surface and their interpretation in the context of strong electron correlation as well as macroscopic transport properties and the physical picture behind them. Most important, the new results evidence the existence of a highly conductive surface channel as well as states within the Mott gap at the surface.

In this work, various physical phenomena apparent in  $\text{Na}_2\text{IrO}_3$  are covered, ranging from strong correlation over topology to transport phenomena. To provide a basis for this, a comprehensive introduction to the predicted and examined properties of  $\text{Na}_2\text{IrO}_3$  is given in the chapters 2 and 3. Here, chapter 2 focuses on the  $\text{Na}_2\text{IrO}_3$  bulk as well as the related Mott physics, while chapter 3 covers the surface characteristics as well as physical properties associated with topology. Additional physical properties found in experiments that do not arise from the Mott physics or the surface electronic structure are presented in chapter 4. This is followed in chapter 5 by the presentation of the experimental techniques and sample preparation procedures used in the scope of this thesis. All measurement setups are home-built and new techniques were developed specifically for the work on this thesis. For the two central methods, being scanning tunnelling microscopy and macroscopic transport measurements, an introduction to the relevant theoretical concepts and to applicable transport phenomena is given in chapter 5 as well. The scanning probe results are then presented and discussed in chapter 6. Chapter 7 covers the transport results and their discussion. Finally, a joint discussion on the  $\text{Na}_2\text{IrO}_3$  surface electronic structure, incorporating the findings from both methods, is given in chapter 8, before the thesis is concluded with a summary and an outlook.

## 2 Bulk Sodium Iridate: Structural and Electronic Properties

In 2010, single crystalline sodium iridate ( $\text{Na}_2\text{IrO}_3$ ) was synthesized for the first time [28]. This chapter provides an overview over the bulk properties. It will start with the description of the  $\text{Na}_2\text{IrO}_3$  crystal structure. Afterwards, the electronic structure and the concepts required to understand why the bulk of  $\text{Na}_2\text{IrO}_3$  is Mott insulating are presented. Finally, experimental data from the literature on the Mott gap will be shown.

### 2.1 Bulk Crystal Structure

The layered crystal structure of  $\text{Na}_2\text{IrO}_3$  is depicted in Figure 2.1, introducing the crystallographic directions  $a$ ,  $b$  (in-plane) and  $c$  (out of plane). The material consists of alternately stacked  $\text{Na}_6$  and  $\text{Na}_2\text{Ir}_4\text{O}_{12}$  layers, which are referred to as sodium layers ( $\text{Na}_6$ ) and iridate layers ( $\text{Na}_2\text{Ir}_4\text{O}_{12}$ ) in this thesis [18], [19], [22], [28], [30], [31]. The sodium layers consist of a quasi-hexagonal arrangement of Na [18], [19], [22], [28], [30], [31]. The iridate layers have a higher complexity, where the iridium atoms form a characteristic honeycomb structure and are surrounded by edge sharing oxygen octahedra. A single sodium atom sits in the centre of every honeycomb [18], [19], [22], [28], [30], [31], see Figure 2.1 a). The resulting unit cell is monoclinic and belongs to the  $C2/m$  space group [32]. X-ray diffraction experiments revealed the unit cell parameters to be  $a_{\text{uc}} = 5.427(1) \text{ \AA}$ ,  $b_{\text{uc}} = 9.395(1) \text{ \AA}$ ,  $c_{\text{uc}} = 5.615(1) \text{ \AA}$  and  $\beta_{\text{uc}} = 109.037(18)^\circ$  at 300 K [19], [32]. The oxygen octahedra were shown to be distorted with Ir-O-Ir bond angles of  $98^\circ - 99.4^\circ$  [33], influencing the overlap of the iridium and oxygen orbitals.

The iridium atoms donate their  $6s^2$  and two  $5d^7$  valence electrons to the oxygen atoms, resulting in an  $\text{Ir}^{4+}$  state [22], [34]. Similarly, the sodium atoms donate their  $3s^1$  valence electron leading to an overall  $\text{O}^{2-}$  state for the oxygen atoms [22], [34]. Consequently, the sodium layer is positively charged, where the iridate layer has a negative net charge, resulting in ionic interlayer bonding [17]. Within the iridate layer, iridium and oxygen atoms are covalently bonded to each other and ionically bonded to the sodium atoms at the honeycomb centre [17], [18], [30], [31].



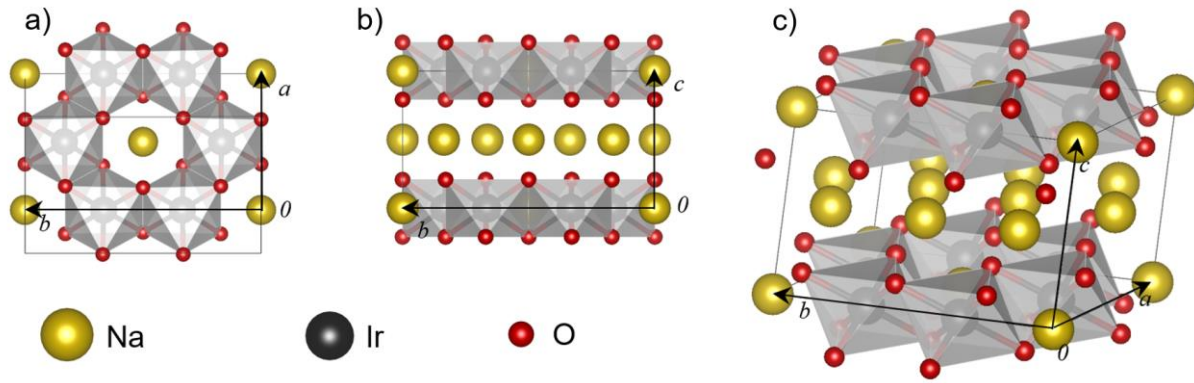


Figure 2.1 Crystal structure of  $\text{Na}_2\text{IrO}_3$ . a) Top view of the  $\text{NaIr}_2\text{O}_6$  layer, showing the edge-sharing  $\text{IrO}_6$  octahedra forming a honeycomb lattice. The centre of every honeycomb is occupied by a single Na atom. b) Side view of the  $\text{Na}_2\text{IrO}_3$  layer structure. c) Unit cell of  $\text{Na}_2\text{IrO}_3$ , consisting of alternately stacked honeycomb  $\text{NaIr}_2\text{O}_6$  and  $\text{Na}_3$  layers [28], [31].

These binding characteristics are relevant for three reasons: firstly, the anisotropy between intra- and interlayer bonding results in the preference for cleaving between the crystal layers. Secondly, such layered materials with comparably weak inter-layer bonding are prone to stacking faults, which complicates their synthesis and requires sophisticated accompanying characterization measurements to evidence good quality [17]. And thirdly, the spatial alignment of the Ir 5d orbitals with respect to the neighbouring oxygen p orbitals within the honeycomb structure determines the electronic properties.

## 2.2 Bulk Electronic Structure

The 5d orbitals of the iridium atoms dominate the electronic properties of sodium iridate close to the Fermi level [28], [34], [35]. It was discussed that  $\text{Na}_2\text{IrO}_3$  exhibits an energy gap, and that the existence of this gap can only be explained by considering crystal-field splitting, spin-orbit coupling and on-site electron-electron correlation simultaneously [19], [30]. As on-site correlation is required, the  $\text{Na}_2\text{IrO}_3$  is thought as a spin-orbit assisted Mott insulator and the band gap as Mott gap [25], [26], [36], [37]. The size of this Mott gap is comparable to the band gap sizes of common semiconductors (e.g. GaAs with a band gap of  $\sim 1.43$  eV at room temperature [38]). However, the quantitative results regarding the Mott gap size vary between 0.34 eV and 1.2 eV among different investigations [18], [19], [26].

The donation of the Ir  $6s^2$  electrons and two Ir  $5d^7$  electrons to the surrounding oxygen atoms changes the iridium electronic configuration from  $[\text{Xe}]6s^25d^74f^{14}$  to  $[\text{Xe}]5d^54f^{14}$ , with the Fermi

level lying within the Ir-5d states. Moreover, one has to consider that the primitive unit cell contains two iridium atoms [19], [24], [25]. Hence, five electrons per iridium atom, i.e. ten electrons for the primitive unit cell, occupy ten 5d-bands [25]. In the following, the picture behind the  $\text{Na}_2\text{IrO}_3$  band gap between iridium 5d states is presented.

### 2.2.1 Crystal Field Splitting and Trigonal Distortion in $\text{Na}_2\text{IrO}_3$

Crystal field splitting describes the impact of interactions of overlapping neighbouring orbitals on the energy level of the orbitals in a crystal in a single particle picture. An overview over the Ir 5d orbitals and their spatial coordination within the surrounding oxygen octahedron is illustrated in Figure 2.2.

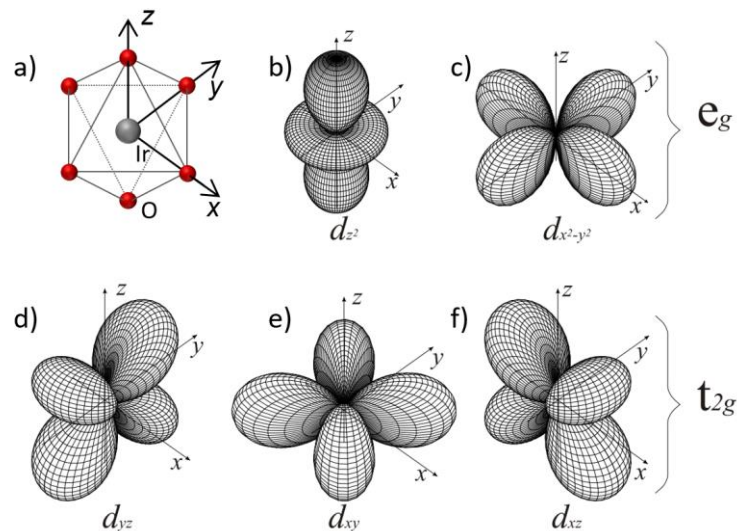


Figure 2.2 Spatial extension of the Ir-5d-orbitals in  $\text{Na}_2\text{IrO}_3$ . a) Depiction of a single  $\text{IrO}_6$  octahedron without distortion and oriented in accordance with the orientation in b)-f). b), c) The  $e_g$  orbitals  $d_{z^2}$  and  $d_{x^2-y^2}$  are oriented towards the surrounding oxygen atoms. d)-f) The  $t_{2g}$  orbitals  $d_{yz}$ ,  $d_{xy}$  and  $d_{xz}$  are oriented towards the edges of the surrounding oxygen octahedron, i.e. between the oxygen atoms. After [39].

As every oxygen atom in the system accepts two electrons, being donated by the iridium and sodium atoms, their charging is twofold negative ( $\text{O}^{2-}$ ), resulting in a repulsive interaction for electrons in spatially close orbitals [40]. As a consequence, the iridium 5d-orbitals that reach closer to the oxygen 2p orbitals, i.e. the two  $e_g$  orbitals as seen in Figure 2.2 a)-c), shift to a higher energy compared the three  $t_{2g}$  orbitals [39], [41]. The crystal field induced energy difference between the  $\text{Na}_2\text{IrO}_3$   $t_{2g}$  and  $e_g$  orbitals was reported to be  $\Delta E_{e_g t_{2g}} \approx 2 - 3$  eV from

resonant inelastic X-ray scattering (RIXS) measurements [42], [43]. It is worth noting, that the RIXS investigations measure the relative energetic position of the Ir 5d orbitals with crystal field splitting, spin-orbit coupling and Hubbard repulsion in effect, and that the assignment of spectral features from the RIXS measurements to the respective Ir 5d orbital is disputed [44]. The energetic situation in a single iridium atom picture is shown in Figure 2.3 a). Since the three  $t_{2g}$  states can be occupied by six electrons (two spin directions per orbital), the  $e_g$  states remain empty and all five 5d electrons occupy  $t_{2g}$  orbitals [34].

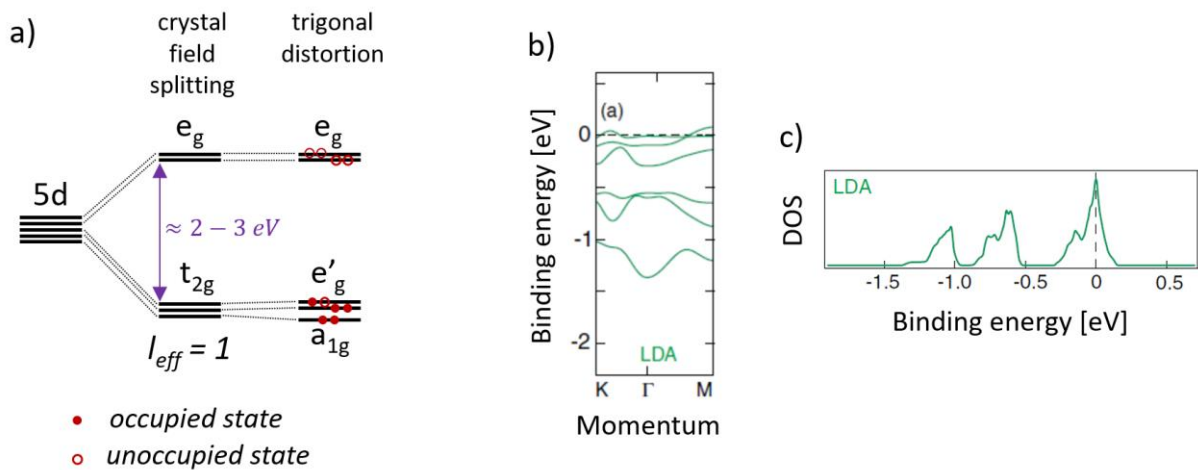


Figure 2.3 Energy levels, band structure and resulting density of states for the Ir 5d  $t_{2g}$  states in  $\text{Na}_2\text{IrO}_3$  simulated via DFT in the LDA. a) Scheme of the energy level splitting due to crystal field effects and trigonal distortion of the  $\text{IrO}_6$  octahedra considering a single Iridium atom. Filled red dots mark the occupation of a state with one electron. Red circles indicate unoccupied states. Adapted from [34] and [42]. b), c) Results from DFT and LDA calculations considering both Ir-atoms in the primitive unit cell, incorporating crystal field effects and showing a Fermi level crossing of  $t_{2g}$  bands and an apparent density of states at the Fermi level [19].

The anisotropy due to trigonal distortion further impacts the 5d energy levels by splitting the  $t_{2g}$  states into a lower  $a_{1g}$  and two upper  $e'_g$  states [42], [45]. However, the energetic impact of the distortion on the states is only  $\sim 2\%$  of the influence due to crystal field splitting [42]. Since, in a single Ir-atom picture, two of the five iridium 5d-electrons occupy the energetically lower  $a_{1g}$  orbitals, the remaining electrons occupy three out of four  $e'_g$  states.

Crystal field splitting and trigonal distortion alone do not open a band gap in  $\text{Na}_2\text{IrO}_3$ , which is reflected by density functional theory (DFT) calculations in the local-density approximation (LDA) considering both Ir-atoms in the primitive unit cell, as shown in Figure 2.3 b) and c). Here, the six  $t_{2g}$  bands (three  $t_{2g}$  orbitals and two Ir in the unit cell) are shown in b), while the corresponding density of states is depicted in c), showing no band gap at the Fermi level.

## 2.2.2 Spin-Orbit Coupling in Na<sub>2</sub>IrO<sub>3</sub>

Spin-orbit coupling (SOC) describes the interaction of an electron's spin with the orbital angular momentum in a single particle picture and is modelled either via LS-coupling or JJ-coupling, depending on the atomic number [46]. Typically, an atomic number of  $Z=30$  is used as the threshold above which the system needs to be described via JJ-coupling [46]. Iridium has an atomic number of  $Z=77$ , and JJ-coupling has to be considered. The effective angular momentum for the iridium 5d orbitals is then described via

$$j_{\text{eff}} = l_{\text{eff}} + s, \quad 2.1$$

with the orbital angular momentum  $l_{\text{eff}}$  and the electron spin  $s$  [21]. Since the orbital angular momentum for the  $t_{2g}$  orbitals is  $l_{\text{eff}} = 1$  [21], the SOC causes a splitting into two energetically lower  $j_{\text{eff}} = 3/2$  states and one energetically higher  $j_{\text{eff}} = 1/2$  state, as depicted in Figure 2.4 a), showing the energy scheme considering a single Ir atom.

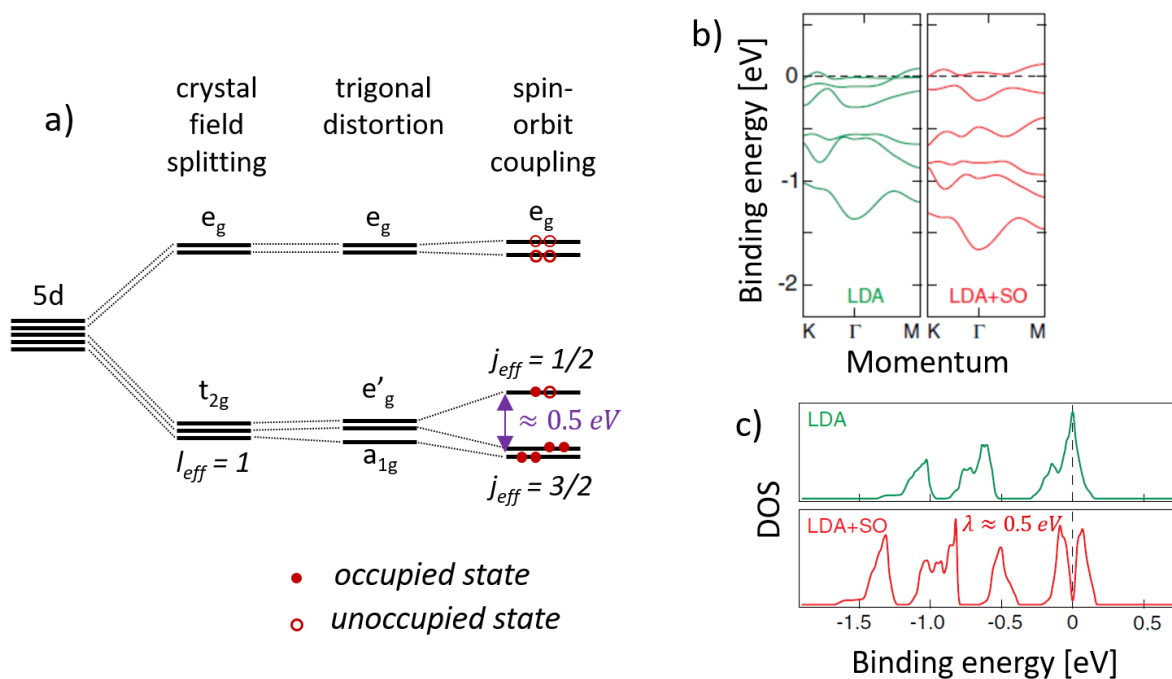


Figure 2.4 Energy levels, band structure and resulting density of states for the Ir 5d  $t_{2g}$  states in Na<sub>2</sub>IrO<sub>3</sub> simulated via DFT in the LDA with incorporation of SOC. a) Scheme of the energy level splitting due to crystal field effects and trigonal distortion of the IrO<sub>6</sub> octahedra and SOC in a single iridium picture. The SOC strength was modelled to be  $\approx 0.5$  eV, violet arrow. Filled red dots mark the occupation of a state with one electron. Red circles indicate unoccupied states. Adapted from [34] and [42]. b), c) Results from DFT and LDA calculations incorporating crystal field effects and SOC, showing  $t_{2g}$  bands in the direct vicinity of the Fermi level. Even though the DOS at the Fermi level is considerably reduced, no open band gap emerges level [19].

All  $j_{\text{eff}} = 3/2$  states are occupied by 5d electrons, leaving only one valence electron left, resulting in a half filled  $j_{\text{eff}} = 1/2$  orbital [34], [42]. DFT-LDA calculations where SOC is being incorporated and both Ir-atoms in the primitive unit cell are considered are shown in Figure 2.4 b) and c). Here, the SOC strength was modelled to be  $\lambda \approx 0.5$  eV. Even though the density of states corresponding to the  $j_{\text{eff}} = 1/2$  bands has a minimum at the Fermi level, no band gap is found.

### 2.2.3 Hubbard Repulsion in $\text{Na}_2\text{IrO}_3$

Hubbard repulsion incorporates the on-site electron-electron repulsion, that occurs when a given orbital is occupied by two electrons with opposing spin, into band theory, leaving the single particle picture [28], [47], [48]. Even though the Pauli-principle does not restrict the occupation of an orbital with two electrons with opposing spin, a Coulomb repulsion between the electrons is always apparent. However, only in strongly correlated electron materials, this repulsion is strong enough to have a considerable impact. This is the case for the iridium  $j_{\text{eff}} = 1/2$  orbitals in  $\text{Na}_2\text{IrO}_3$ .

The Hubbard-model was the first ansatz to describe the dynamics of correlated electrons, with the Hamiltonian [48]–[51]:

$$H = U \sum_i c_{i\uparrow}^\dagger c_{i\uparrow} c_{i\downarrow}^\dagger c_{i\downarrow} - t \sum_{\langle ij \rangle, \sigma} (c_{i\sigma}^\dagger c_{j\sigma} + c_{j\sigma}^\dagger c_{i\sigma}) , \quad 2.2$$

Here, summation is done over all lattice sites  $i$  and all neighbouring lattice sites  $\langle ij \rangle$  as well as over both spin directions  $\sigma$ .  $c_{i\sigma}^\dagger$  and  $c_{i\sigma}$  are the fermionic creation and annihilation operators of an electron at lattice site  $i$  with spin  $\sigma$ . The so-called Hubbard  $U$  is a measure of the Coulomb repulsion.  $t$  is the hopping amplitude for neighbouring hopping sites, i.e.  $t$  describes the wavefunction overlap for adjacent lattice sites. The Hamiltonian describes the competition between the repulsive on-site Coulomb interaction raising the energy level (equation 2.2, first term) with the electrons kinetic energy stemming from inter-site hopping (equation 2.2, second term). For half-filled bands, the ratio  $U/t$  gives qualitative information about the material. For  $U/t \ll 1$ , the Coulomb repulsion is small, and the electrons have high mobility, resulting in metallic behaviour [51], [52]. For  $U/t \gg 1$ , the Coulomb repulsion dominates, and the electrons are localized causing insulating behaviour. In this case, the initial band is split into the lower Hubbard band (LHB) and the upper Hubbard band (UHB). The energy gap between LHB and UHB is referred to as the Mott gap  $E_{\text{Mott}}$ . Considering a half-filled orbital, the splitting into a LHB and an UHB results in the LHB being filled and the UHB being empty, with the Fermi level

sitting at the centre of the Mott gap, as can be seen in Figure 2.5. Such insulators are referred to as Mott insulators. The size of  $E_{\text{Mott}}$  can be determined from the bandwidth  $W$  and the Hubbard repulsion  $U$  via [39], [48]:

$$E_{\text{Mott}} \approx U - W \quad . \quad 2.3$$

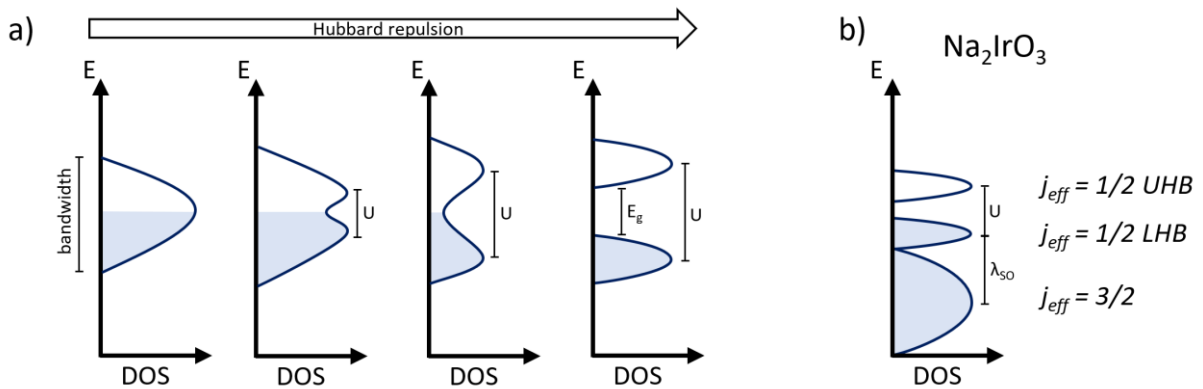


Figure 2.5 a) The effect of increasing Hubbard repulsion  $U$  on the density of states for a single orbital with a given band width at  $U=0$  (left) and half filling. For a small  $U$ , the DOS begins to split, as the occupation of an orbital with a second electron costs energy. With increasing  $U$ , the DOS gets further teared until it is fully split into two sub-bands (the upper and lower Hubbard band), when  $U$  is large enough to overcome the bandwidth. Both bands contain half the number of initial states. In a half-filled system, this leads to a filled lower and an empty upper Hubbard band, separated by a band gap – and the system becomes a Mott insulator. b) Situation for  $\text{Na}_2\text{IrO}_3$  in a single iridium picture. Here, Hubbard repulsion splits the half-filled  $j_{\text{eff}}=1/2$  band into upper and lower Hubbard bands, driving the system into the Mott insulating phase. This is possible, as crystal field splitting and spin-orbit coupling energetically separate the  $j_{\text{eff}} = 1/2$  band from the other Ir-5d-bands, reducing the bandwidth that  $U$  needs to overcome.

In summary, the existence of an energy gap in  $\text{Na}_2\text{IrO}_3$  can be understood. Three ingredients are required: high  $U$ , low  $W$ , and half-filled orbitals. The high Coulomb repulsion is achieved by the localization of the Ir 5d orbitals within the surrounding  $\text{O}^{2-}$  octahedron. The low  $W$  and the half-filling result from the crystal field splitting and spin-orbit coupling, that energetically isolate the  $j_{\text{eff}}=1/2$  bands from the other Ir 5d bands, significantly decreasing the bandwidth (and therefore  $t$ ) that needs to be overcome by the Coulomb repulsion [19].

The occurrence of all three effects – crystal field splitting, spin-orbit coupling and Hubbard repulsion – on similar energy scales renders  $\text{Na}_2\text{IrO}_3$  to be a spin-orbit assisted Mott insulator [19], [28], [42], [43], as schematically depicted in Figure 2.6 a) in a single iridium picture. In the scope of this work, the band gap between the  $\text{Na}_2\text{IrO}_3$   $j_{\text{eff}}=1/2$  LHB and UHB will be referred to as the Mott gap  $E_{\text{Mott}}$ . Other gaps, e.g. the gap between the  $j_{\text{eff}}=3/2$  and the  $j_{\text{eff}}=1/2$  bands, will be referred to as energy gap, where the notation will include the bands that are separated by the energy gap, e.g.  $E_{j_{3/2}, j_{1/2}}$  for the energy gap between the  $j_{\text{eff}}=3/2$  and the  $j_{\text{eff}}=1/2$  bands.



Importantly, the physical pictures underlying the Mott gap and the energy gaps are fundamentally different. The energy gaps can be described in a single-particle picture, while the Mott gap arises from many-body interactions in the form of on-site electron-electron correlation. This is reflected in the energy diagram for  $\text{Na}_2\text{IrO}_3$  in a single iridium picture in Figure 2.6 a).

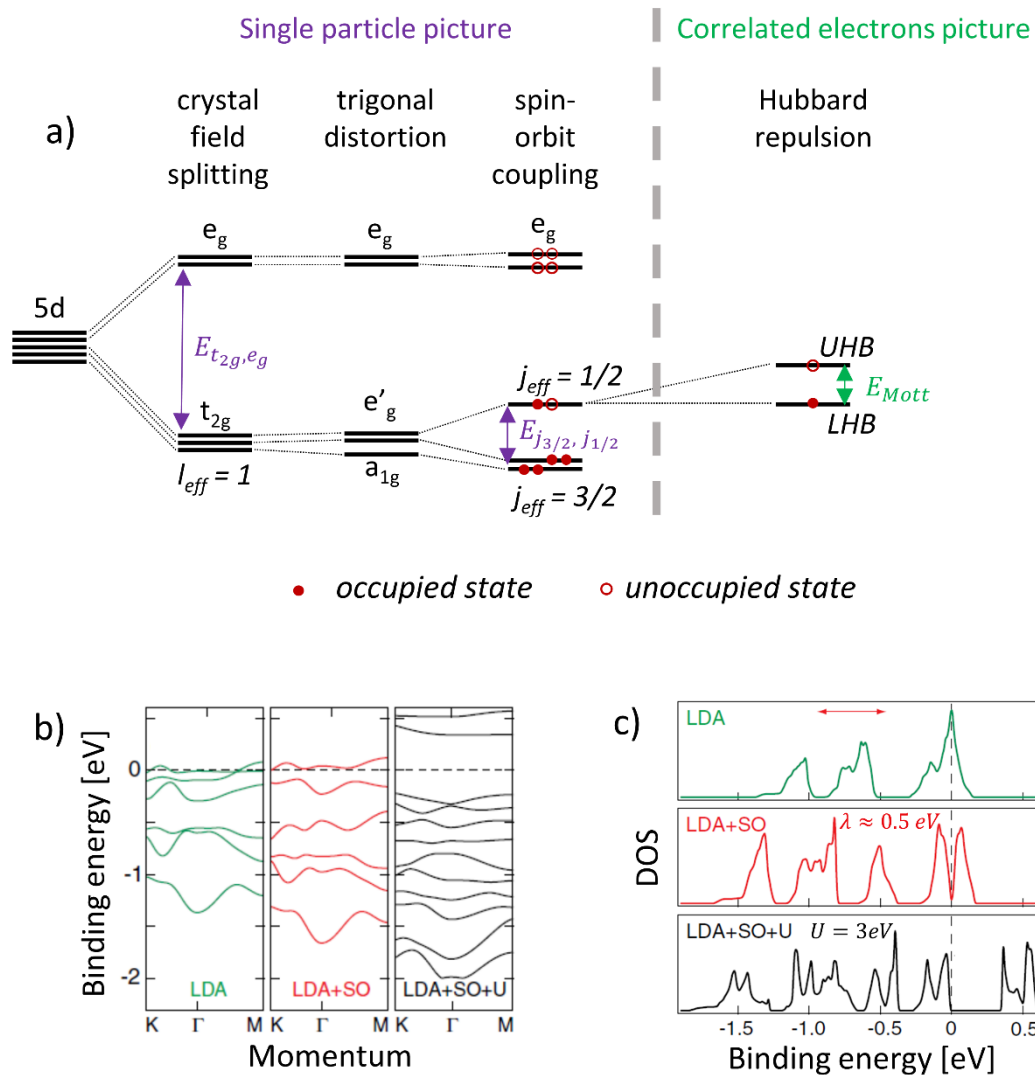


Figure 2.6 Energy levels, band structure and resulting density of states for the Ir 5d  $t_{2g}$  states in  $\text{Na}_2\text{IrO}_3$  simulated via DFT in the LDA with incorporation of SOC and the Hubbard repulsion  $U$ . a) Scheme of the energy level splitting due to crystal field effects and trigonal distortion of the  $\text{IrO}_6$  octahedra, SOC and Hubbard repulsion in a single iridium picture. Filled red dots mark the occupation of a state with one electron. Exemplary energy gaps are marked in violet, while the Mott gap is marked in green, with  $E_{\text{Mott}} \approx 0.34 \text{ eV}$ . Red circles indicate unoccupied states. Adapted from [34] and [42]. b), c) Results from DFT and LDA calculations incorporating crystal field effects, SOC and  $U$ , as well as both Ir-atoms in the primitive unit cell, showing the emergence of an energy gap when all three effects are considered simultaneously. [19].

It is worth noting that the exact parameters for the strength of the crystal field splitting, the spin-orbit coupling and the Hubbard repulsion are still the subject of ongoing investigations [53].

DFT results incorporating an energy shift between the  $j_{\text{eff}}=1/2$  bands and arguing that such a shift could only arise from Hubbard repulsion are shown in Figure 2.6 b), c), where ARPES and optical conductivity data were used to find suitable parameters. For the spin-orbit coupling,  $\lambda \approx 0.5$  eV was suggested and for the Hubbard repulsion a value of  $U \approx 3$  eV was proposed to fit the simulations to the experimental data [19]. The doubling of the number of bands in Figure 2.6 b) is due to the consideration of antiferromagnetism once an energy gap is apparent, effectively doubling the unit-cell size and hence the number of bands. Since the DFT simulations could not explain the existence of a band gap without the incorporation of Hubbard repulsion, it was argued that  $\text{Na}_2\text{IrO}_3$  is a Mott insulator [19].

### 2.3 Experimental Findings on the Bulk Mott Gap of $\text{Na}_2\text{IrO}_3$

The identification of the mechanisms that render  $\text{Na}_2\text{IrO}_3$  to be a Mott insulator is based on experimental results from angle resolved photoemission spectroscopy (ARPES) combined with optical conductivity measurements as depicted in Figure 2.7 [19].

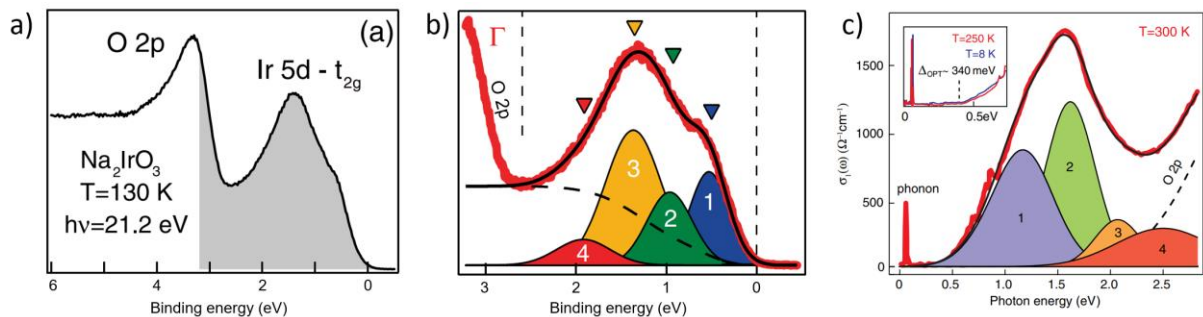


Figure 2.7 Experimental findings on the  $\text{Na}_2\text{IrO}_3$  band gap by means of photoemission spectroscopy and optical conductivity measurements. a) Angle integrated photoemission spectrum of O and Ir valence band b) Energy distribution curve for the valence band at the  $\Gamma$ -point measured with ARPES. The spectrum was fitted using four Gauss-peaks that were attributed to Ir 5d  $t_{2g}$  states. The steep inset at  $\sim 2.6$  eV is due to oxygen 2p states. At the chemical potential no spectral weight is apparent. c) Optical conductivity data as well as a fit to model the data using again four Gauss-peaks representing Ir 5d  $t_{2g}$  states. For the fit, both ARPES and optical data were used. The colours and the numerations correspond to b). The inset shows the measured band gap for  $T=250$  K and  $T=8$  K, showing no significant temperature dependence [19].

Integrated photoemission spectra show a broad spectral weight below the Fermi level (Figure 2.7 a), 0-3 eV) that was attributed to Ir 5d  $t_{2g}$  states. Further below the Fermi level at  $\sim 2.6$  eV, spectral weight emerges due to oxygen 2p states. At 0 eV, no considerable spectral weight is apparent in agreement with the existence of a Mott gap. In Figure 2.7 b), the energy distribution



curve for the valence band at the  $\Gamma$ -point measured with ARPES is depicted. The energy distribution was modelled using four Gauss-peaks, being the minimum number of peaks that was needed in the model. This highlights the difficulty to disentangle the contributions from different  $t_{2g}$  bands and the considerable energy shifts from the degenerated Ir 5d states due to crystal field splitting, spin-orbit coupling and Hubbard repulsion. Optical conductivity measurements paint a similar picture, Figure 2.7 c). Again, four peaks related to the optical transitions from  $t_{2g}$  states as well as the optical transmission from the oxygen 2p states to the valence band, i.e. the UHB, were used to model the experimental data. Between 0 eV and  $\sim 0.34$  eV photon energy, no signal is observed due to the existence of a Mott gap. The zoom-in in the inset in Figure 2.7 c) shows that no substantial temperature dependence of the optical gap, and hence the Mott gap, was found [19].

It is worth noting that the role of the  $\text{Na}_2\text{IrO}_3$  surface and its reconstruction was not yet investigated at the time the measurements presented above were reported. This role is illuminated in chapter 3.

### 3 Sodium Iridate Surface: Structural and Electronic Properties

After the presentation of structure, physical concepts and experimental data for the  $\text{Na}_2\text{IrO}_3$  bulk in the previous chapter, the properties of the surface are outlined in this chapter. This will begin with the structure of the surface. After this, a brief introduction to non-trivial topology and the implications for the boundary of a topological material will be given. Then, the theoretical predictions regarding non-trivial topology in  $\text{Na}_2\text{IrO}_3$  will be presented. The chapter is closed with a presentation of reported electronic properties of the  $\text{Na}_2\text{IrO}_3$  surface from ARPES and scanning tunnelling spectroscopy (STS).

#### 3.1 $\text{Na}_2\text{IrO}_3$ Surface Structure

For investigations of the  $\text{Na}_2\text{IrO}_3$  surface, samples are cleaved and probed in UHV to protect the surface from contaminations and degeneration. The layered nature of the crystal resulting in the weaker inter-layer bonding compared to the intra-layer bonding determines the feasible cleaving direction to be in the crystallographic  $ab$ -plane [29]. This results in two possible cleaves: either between a sodium layer and an adjacent iridate layer or within a sodium layer, effectively splitting it in half. Both scenarios are depicted in Figure 3.1.

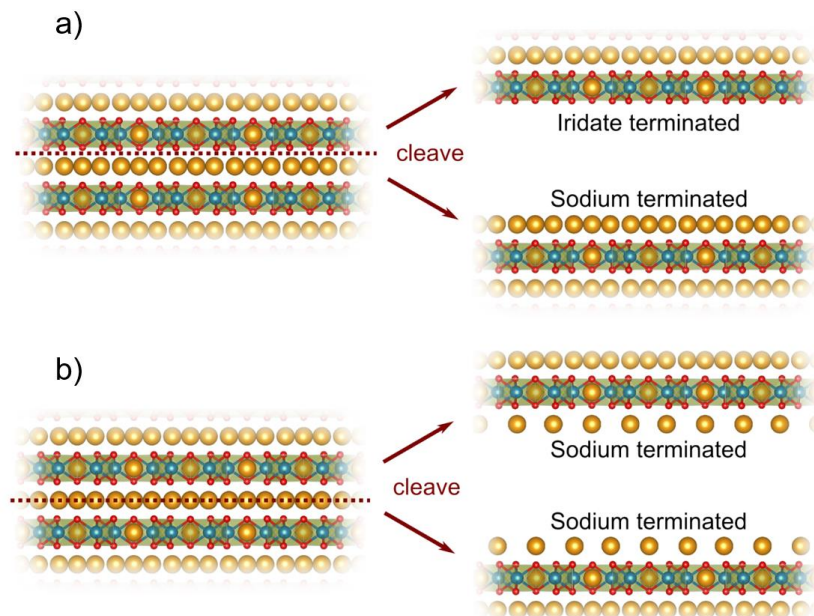


Figure 3.1 Possible cleaving planes in  $\text{Na}_2\text{IrO}_3$ . a) Cleaving plane between two different layers resulting in two distinct terminations with opposing charge b) Cleaving plane within the sodium layer where one half of the layer remains on either side of the crystal and the resulting surfaces are charge neutral. Adapted from [29].

STM work of Lüpke et al. [18], [29] showed the existence of two different surface terminations, which was later confirmed by spatially resolved ARPES measurements [26]. This makes a cleaving process that splits the sodium layer unlikely, as both resulting surfaces would be identical, resulting in only one apparent surface termination. The two terminations correspond to either the sodium or the iridate layer at the surface. The chemical compositions of the surface layer is not identical with the respective bulk layer. In both cases, 2/3 of the sodium content of the topmost layer vanishes [18], [29]. In case of an iridate-termination, the remaining topmost sodium atoms further relax by  $\sim 2 \text{ \AA}$  out of the surface. Sodium terminated surfaces are  $(1 \times 1)$ -reconstructed and iridate terminated surfaces are  $(\sqrt{3} \times \sqrt{3})R30^\circ$ -reconstructed, as is detailed in Figure 3.2. Both surface unit cells are marked in red.

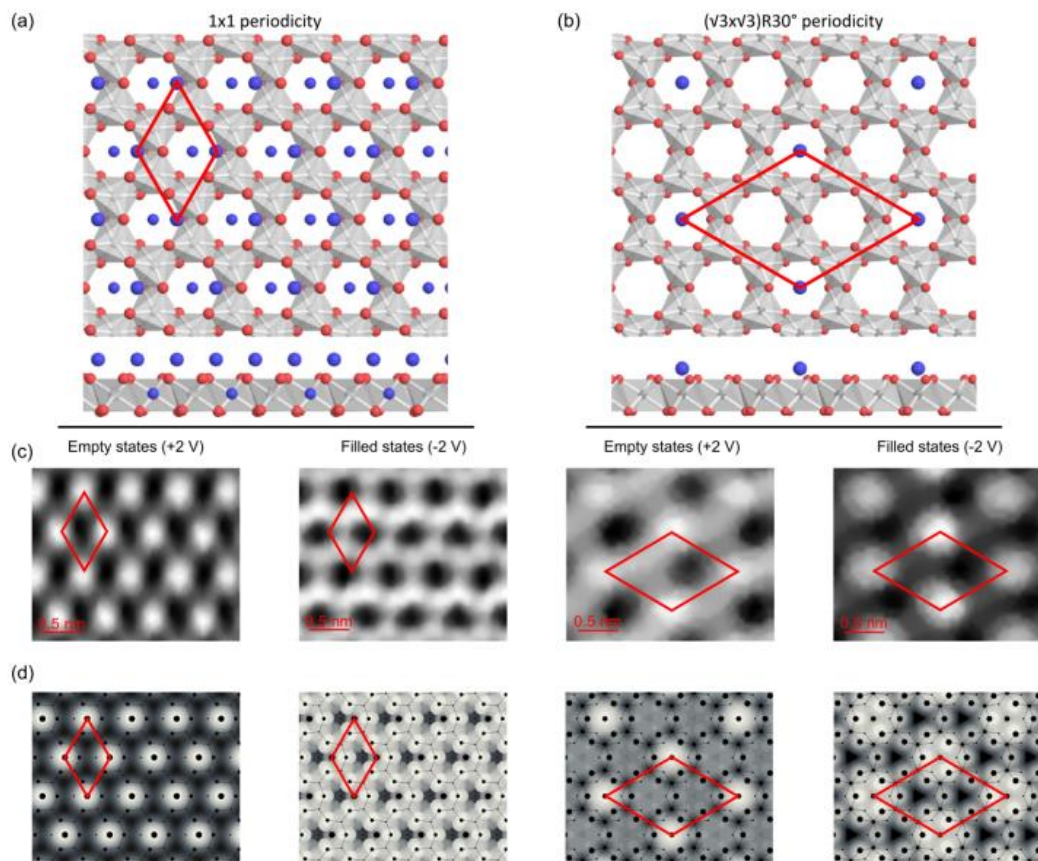


Figure 3.2 Structural models for the  $(1 \times 1)$ - and  $(\sqrt{3} \times \sqrt{3})R30^\circ$ -reconstructed surfaces in a top view (a, b), top pictures) and a side view (a, b) bottom pictures). Na: blue, Ir: grey, O: red. c) Experimental STM images at 2 V and -2 V bias voltage for both surface terminations. d) Simulated STM topographies for the data depicted in c), showing good agreement, and confirming the structural model. The surface unit cells are marked in red. From [18].

To identify the reconstruction in STM measurements, the surface Na-Na distance is used. From the lattice parameters of the bulk unit cell (chapter 2.1), the characteristic distances are  $d_{1, \text{Na-Na}} = 5.427(1) \text{ \AA}$  for the  $(1 \times 1)$ -reconstructed surface and  $d_{2, \text{Na-Na}} \approx 9.395(1) \text{ \AA}$  for the

$(\sqrt{3}\times\sqrt{3})R30^\circ$ -reconstructed surface, under the premise that relaxation does not change these spacings on the surface. The height of single step edges between two terraces with different termination would be estimated from the bulk unit cell to  $h = \sin(\beta_{uc}) \frac{c_{uc}}{2} = 2.653(19) \text{ \AA}$ . STM-investigations at step edges, where the upper terrace was  $(1\times 1)$ - and the lower terrace  $(\sqrt{3}\times\sqrt{3})R30^\circ$ -reconstructed, showed an apparent step height of  $\sim 3 \text{ \AA}$  for a bias voltage of 2 V, and  $\sim 1.5 \text{ \AA}$  for a bias voltage of -2 V [29], deviating from the 2.65  $\text{ \AA}$  suggested by the considerations using the height of the bulk unit cell. This deviation was explained by the fact that STM topographies map the local density of states and not the surface morphology as well as by surface relaxation [29]. Since all found  $(1\times 1)$ - $(\sqrt{3}\times\sqrt{3})R30^\circ$  step heights were greater than 0  $\text{ \AA}$  and smaller than  $2h$ , it is still possible to identify single steps between the two differently reconstructed terraces by means of STM.

### 3.2 Topology and Topologically Protected Conductive States in Solids

Since the first discovery of a real material exhibiting topological non-triviality, the previously solely theoretical concept of topology gained great attention, as it promises new approaches in microelectronics and spintronics [3]–[9], [54]. In the following, a brief introduction to the relevant concepts of topology in solid state physics, that are required to understand the idea of  $\text{Na}_2\text{IrO}_3$  being topologically non-trivial, will be given. The theory of topology in solid state physics classifies materials into topologically trivial and topologically non-trivial by assigning a so-called topological invariant [8], [9], [55]. Non-trivial materials are often simply referred to as topological materials, or as topological insulators (TI) if they exhibit an open band gap. The naming “topological invariant” roots from the analogy to the integer genus in the mathematical field of topology that categorizes geometric forms [8], [55]. Here, two forms have the same genus if they can be smoothly deformed into each other without doing something “radical” like cutting them or punching a hole. In physics, the topological invariant is derived from the Berry phase, which represents the geometric phase acquired when a Hamiltonian undergoes an cyclic adiabatic evolution [55]–[58]. Details on this can be found in [8], [57]. Importantly, it is the bulk Bloch-Hamiltonian that determines the topological invariant, and the band theory is the foundation of the theory of topology in solids.

For a system to be topologically non-trivial, band inversion as well as time reversal symmetry (TRS) are prerequisites [8], [55]. The implications from band inversion will be presented first, before coming to the role of time reversal symmetry. A schematic depiction of band inversion is seen in Figure 3.3.

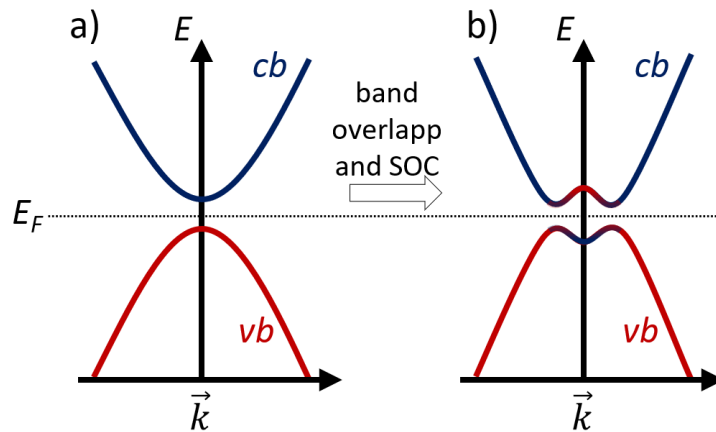


Figure 3.3 Schematic plot showing the transition of the band structure from a trivial insulator phase (a) to a topological insulator phase (b) due to band overlap and a spin-orbit induced gap opening. The valence band is plotted in red, the conduction band in blue.

Figure 3.3 a) shows the valence (red) and conduction band (blue) of a trivial insulator. In a topological material, the highest valence band states lie energetically above the lowest conduction band states, i.e. the bands overlap [8], [55]. If sufficiently strong spin-orbit coupling is apparent, perturbation theory starting from atomic orbitals yields additional terms representing the mixing of valence and conduction band that inhibit a crossing of the bands [11]. Consequently, a gap opens at the crossing points of the bands as depicted in Figure 3.3 b), while valence band states remain above, and conduction band states remain below the gap. This situation is referred to as band inversion, and materials showing such a band structure are potential topological insulators [5], [8], [55], [59].

As mentioned, to change the genus of a geometric object “something radical” needs to take place. The equivalent for “something radical” in topological materials is a closing of the band gap. This can be understood when considering what happens with the inverted bands when a trivial and a topological material are brought into contact. This situation is sketched in Figure 3.4 a).

At the interface region between a topological and a trivial material, the valence band bends down where the conduction band bends up upon transition from the non-trivial to the trivial phase, leading to a band crossing and therefore to a closing of the band gap in the case of topological insulators. This is the so-called bulk boundary correspondence, leading to robust metallic conductivity at the boundary of a topological material.

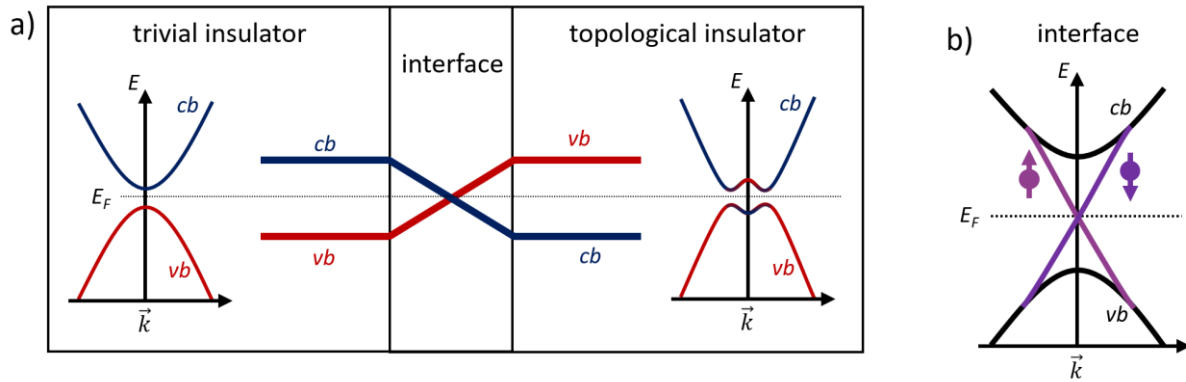


Figure 3.4 Interface between a topologically trivial and a non-trivial material. a) The inverted valence band (VB) bends down, and the inverted conduction band (CB) bends up at the interface to the trivial material, resulting in a band gap closing. b) Due to time-reversal symmetry, the band gap closing occurs via a Dirac-cone, where spin and momentum are locked, and direct electron backscattering is forbidden.

The second characteristic of topological materials is TRS, which enforces a linear dispersion for the boundary states at the band crossing and that the wavevector  $\vec{k}$  is coupled to the electron spin (upon time reversal  $t \rightarrow -t$ , the wavevector is also reversed,  $\vec{k} \rightarrow -\vec{k}$ . Symmetry now requires the spin to also change its sign). The consequence is depicted in Figure 3.4 b): the boundary states within the bulk band gap form a Dirac-cone at the crossing point where backscattering requires the electron spin to flip, i.e. the charge carriers are spin-momentum locked. Such spin-flip is prohibited in absence of magnetic impurities. Hence, boundary channels emerging from topology provide robust metallic conductivity that is not dependent on the structure of the boundary and where backscattering is forbidden.

The dimensionality of the conductive boundary is determined by the dimensionality of the topological system. For topological 2D materials, the conductive channel emerges at the edge, forming a 1D channel [8], [9], [55]. In 1D channels, electron scattering only occurs in forward and backward direction. Since backscattering is prohibited, the transport mediated by the edge channels of 2D topological materials is ballistic. Stacks of 2D topological insulators are referred to as weak 3D topological insulators [8], [55].

For topological 3D materials, the conductive channel emerges at the surface. Transport in such surface channels is not ballistic, as the prohibition of backscattering does not forbid scattering to other directions [8], [9], [55]. Such 3D-TI's are also referred to as strong 3D topological insulators when the bulk of the material is insulating.



### 3.3 Theoretical Predictions of Non-Trivial Topology for Na<sub>2</sub>IrO<sub>3</sub>

Multiple theoretical works from 2009 to 2019 predict the existence of a topological phase in sodium iridate [21]–[25]. In the following, a brief introduction to such predictions is provided.

Incorporating crystal field splitting and spin-orbit coupling  $\lambda$ , it was proposed that band inversion occurs for the spin-orbit coupled iridium 5d bands, leading to 2D-non-trivial topological behaviour [21]. Here, each iridate layer acts as an own topological system where a conducting edge would appear at the border of every layer. The situation within each respective layer is commonly known as a Quantum-Spin-Hall (QSH) system.

Further theoretical work that incorporated hopping beyond nearest neighbours, parameterized by  $t_n$ , where  $t_n = 0$  denotes the absence of hopping beyond nearest neighbours, found both possibilities: that Na<sub>2</sub>IrO<sub>3</sub> may consist of stacked 2D-TI's (i.e. is a weak 3D TI), or that it may be a strong 3D-TI. Starting with the 2D-case, the nearest neighbour hopping amplitudes were fixed, and the initial values for all other parameters were taken from first principles tight-binding calculations [24]. Figure 3.5 shows the considered hopping paths in a) and b) and the evolution of the  $j_{\text{eff}}=1/2$  bands with  $t_n$  close to the Fermi level in c).

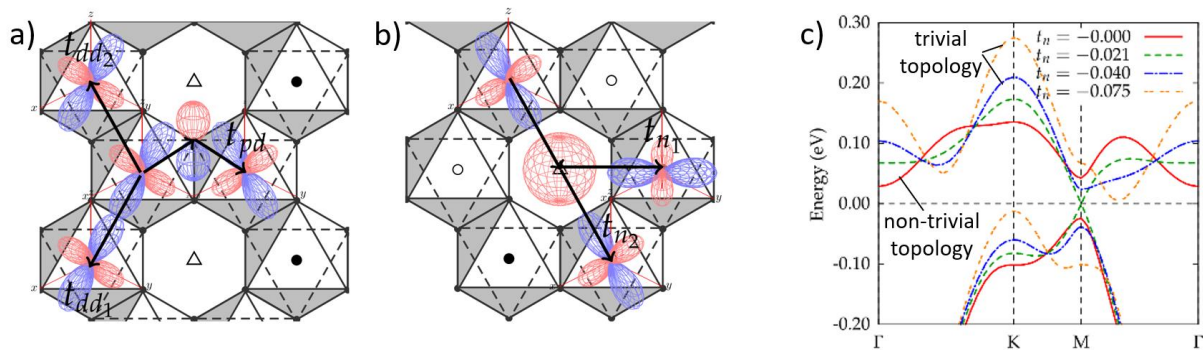


Figure 3.5 Theoretical work on the prospect of nontrivial topology in Na<sub>2</sub>IrO<sub>3</sub> adapted from [24]. Different hopping paths within the iridate layer of Na<sub>2</sub>IrO<sub>3</sub> depending on the consideration of either nearest-neighbour hopping (NNH, a) or second-nearest-neighbour hopping (SNNH, b)). As illustrated, for NNH only the iridium d-orbitals and the oxygen p-orbitals are considered, where for SNNH the hopping occurs via the sodium orbitals. c) Na<sub>2</sub>IrO<sub>3</sub>  $j_{\text{eff}}=1/2$  band structure calculated in a tight binding model for different values of the tight binding-parameter  $t_n$  reflecting hopping via sodium atoms, i.e. hopping beyond nearest neighbour hopping. In a pure NNH situation ( $t_n = 0$  eV), Na<sub>2</sub>IrO<sub>3</sub> was calculated to be topologically insulating. At  $t_n = -0.021$  eV, the system transitions from topologically non-trivial to trivial and the band gap closes with linear dispersion.

In absence of hopping beyond nearest neighbours ( $t_n = 0$ , red curve in Figure 3.5 c)), a band gap exists, and a band inversion is apparent in vicinity of the M-point of the Brillion zone. With rising  $|t_n|$ , the gap size decreases until the gap vanishes, and a Dirac-cone is apparent in the

vicinity of the Fermi level. With  $|t_n|$  further rising, a band gap opens again but without a band inversion. Hence, increasing  $|t_n|$  drives the system from a topological to a trivial phase. It is important to note that the here described band gaps (with and without band inversion) are not Mott gaps, as electron-electron correlation is not considered in Figure 3.5. Instead, the gap between the two  $j_{\text{eff}}=1/2$  bands, that arise since two iridium atoms are apparent in the primitive unit cell, is considered. Hence, the theoretical work underlying Figure 3.5 implies that crystal field splitting and spin-orbit coupling alone might introduce the band gap in  $\text{Na}_2\text{IrO}_3$ , alternatively to the picture of  $\text{Na}_2\text{IrO}_3$  being Mott insulating (chapter 2.2).

$t_n$  is not the only relevant parameter, and varying the trigonal crystal field splitting  $\Delta$  and the spin-orbit coupling  $\lambda$  results in the phase diagram depicted in Figure 3.6

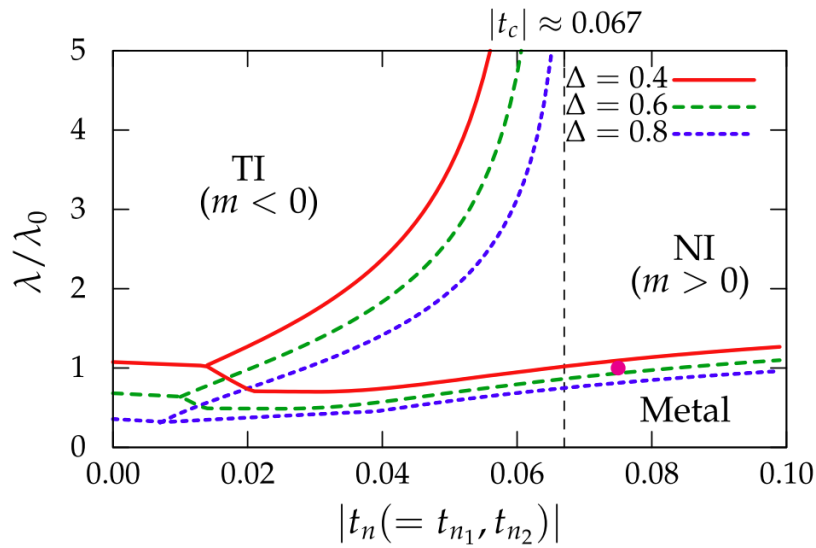


Figure 3.6  $\text{Na}_2\text{IrO}_3$  phase diagram calculated from a first principles tight binding model showing the dependency of the 2D topological phase (topological insulator = TI, normal insulator = NI) on the trigonal crystal field splitting  $\Delta$ , the spin-orbit coupling  $\lambda$  and the hopping via second ( $t_{n_1}$ ) and third ( $t_{n_2}$ ) nearest neighbors. As band inversion is apparent in the TI phase, the effective electron mass  $m$  is negative, while  $m$  is positive for the NI phase without inverted bands. The pink dot indicates the expected values in the real material. All values are in eV.  $|t_c|$  denotes the asymptotic line for  $\Delta = 0.6$  eV [24].

Due to the band inversion, the electron effective mass  $m$  is negative in the topological phase, while it is positive in the trivial phase without band inversion. It becomes clear that high  $\lambda$ , low  $t_n$  and low  $\Delta$  favour a topologically non-trivial phase. Above  $t_n \approx 0.067$  eV, no topological phase is possible independently of  $\lambda$  according to Figure 3.6. It was further reported that the incorporation of out-of-plane hopping amplitudes leads to a 3D topological phase if the interlayer distance is virtually enhanced by 30 % [24].

Even though the theory of topology is based on band theory, i.e. a single particle picture, it was proposed that some iridates might exhibit a topological Mott insulating phase [60]. Theoretical examinations incorporating strong on-site electron-electron correlation for the



investigation of possible topological phases in  $\text{Na}_2\text{IrO}_3$  used a similar ansatz as above as basis, i.e. the consideration of crystal field splitting and spin-orbit coupling, to identify topologically trivial and non-trivial band insulating phases [25]. From there, it was argued that increasing the Hubbard repulsion  $U$  would monotonically decrease the band gap size due to inhibiting its kinetic effect until the gap vanishes. Upon further increase of  $U$ , a Mott gap would form and grow monotonically in size with  $U$ . It was proposed that the topological invariant stays the same if the gap closing between band insulating and Mott insulating phase occurs at a point in the Brillouin zone that is not a time-reversal invariant momentum (TRIM) point [25]. In such a case, the Mott insulating phase “inherits” the topological invariant from the band insulating phase. Using cluster perturbation theory, it was shown that a Hubbard repulsion driven transition from the topologically non-trivial band insulating phase to the Mott insulating phase can occur, where the valence and conductance band meet at the non-TRIM K-point at the phase boundary. A phase diagram showing both, topologically non-trivial band and non-trivial Mott insulating phases in dependence of the Hubbard repulsion  $U/t$ , parametrized with the hopping amplitude for neighbouring hopping sites  $t$ , and the nearest neighbour hopping parameter  $\theta$ , is shown in Figure 3.7.  $\theta$  parametrizes the relative strength between hopping via oxygen p-states  $t_1$ , and direct hopping  $t'_1$  between  $t_{2g}$  orbitals, with  $t_1 = t \cdot \cos(\theta)$  and  $t'_1 = t \cdot \sin(\theta)$ . The spin-orbit coupling is fixed at  $\lambda = 1.6 \cdot t$ .

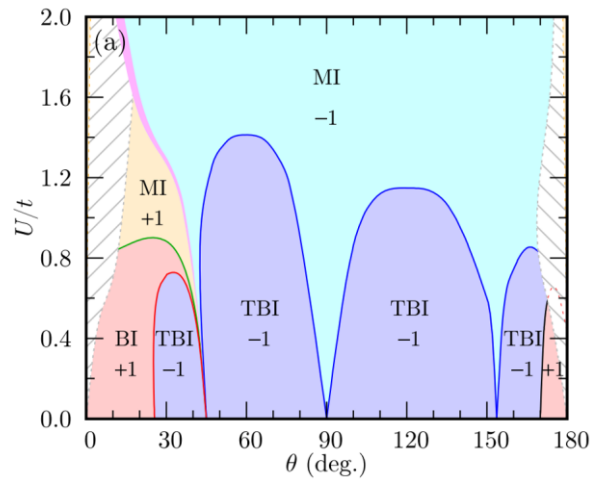


Figure 3.7 Phase diagram for fixed spin-orbit coupling  $\lambda = 1.6 \cdot t$  with respect to the Hubbard repulsion  $U/t$  and the nearest neighbour hopping parameter  $\theta$ . Here,  $\theta$  parametrizes the relative strength between hopping via oxygen p-states  $t_1$ , and direct hopping  $t'_1$  between  $t_{2g}$  orbitals, with  $t_1 = t \cdot \cos(\theta)$  and  $t'_1 = t \cdot \sin(\theta)$ .  $t$  denotes the hopping amplitude for neighbouring hopping sites. Violet (red) as well as cyan (orange) areas represent the band and the Mott insulator phase, respectively, with the topological invariant -1 (+1). BI = band insulator phase, TBI = topological band insulator phase, MI = Mott insulator phase. From [25].

In the phase diagram, the cyan coloured region represents a Mott insulating phase with the identical topological invariant (-1) as the topologically non-trivial band insulating phase marked in violet, giving the theoretical prospect of a topologically Mott insulating phase in  $\text{Na}_2\text{IrO}_3$ . Additionally, it was argued that a transition from a trivial to a non-trivial Mott insulating phase might be possible without a band gap closing at the phase boundary (light pink line in Figure 3.7) [25].

Up to now, it is not clear if sodium iridate exhibits topologically non-trivial characteristics, as experimental findings paint a very diffuse picture and the quantitative tight-binding parameters are disputed [30]. The next chapter provides an overview over reported  $\text{Na}_2\text{IrO}_3$  surface electronic properties.

### 3.4 $\text{Na}_2\text{IrO}_3$ Surface Electronic Properties

Different experimental investigations of the  $\text{Na}_2\text{IrO}_3$  surface electronic structure report vastly different results for the size and existence of a band gap at the  $\text{Na}_2\text{IrO}_3$  surface.

ARPES datasets showing states in the vicinity of the Fermi level are depicted in Figure 3.8 [37], [61]. The measurements did not distinguish between different surface terminations. Hence, the data in Figure 3.8 can be understood as an averaging over both terminations. The in-gap states seen in a)-c) were argued to have linear dispersion throughout the whole Mott gap, purple dotted line, and it was discussed that this results in surface metallicity [61]. However, the quality of the data is not high enough to prove a linear dispersion of the in-gap states. Furthermore, in the context of the Mott insulating nature of the  $\text{Na}_2\text{IrO}_3$  bulk, it is worth noting that the width of the valence band (i.e. the LHB) was found to be rather high with  $\sim 1$  eV. The ARPES data published in another work (Figure 3.8 d), e) also show an apparent in-gap density of states, i.e. between the valence band edge at  $\sim 0.3$  eV -  $\sim 0.4$  eV and the Fermi level [37], with no linear dispersion attributed to the in-gap states.

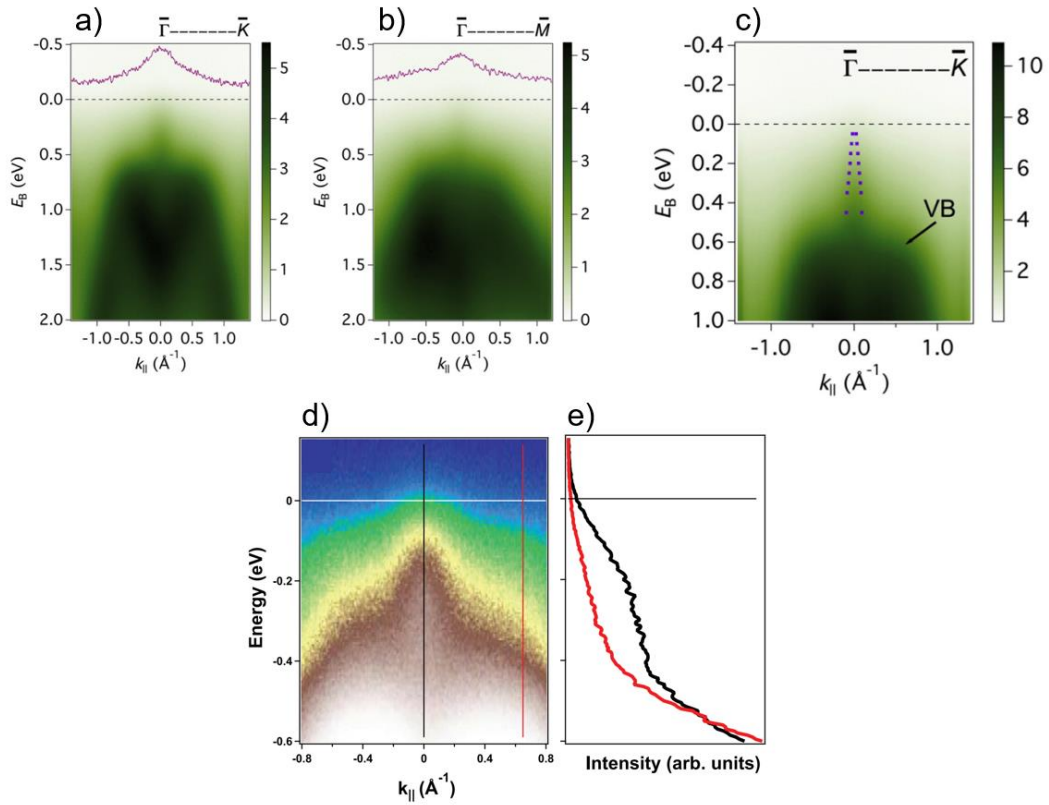


Figure 3.8 Band structure of  $\text{Na}_2\text{IrO}_3$  measured with ARPES. Data along the high symmetry directions  $\bar{\Gamma} - \bar{K}$  (a) and  $\bar{\Gamma} - \bar{M}$  (b) of the Brillouin zone measured with ARPES averaged over both surface terminations. On top of the graphics, the momentum distribution curves at the Fermi level are plotted in purple. c) Zoom-in on a) showing states in the vicinity of the Fermi level. The dashed purple lines mark linear dispersion. The width of the valence band is  $\sim 1$  eV [61]. d) Measured electronic band structure along the  $\bar{\Gamma} - \bar{M}$  symmetry direction from another ARPES work [37], showing density of states between  $-0.4$  eV and the Fermi level. e) Energy distribution curves integrated over  $0.04 \text{ \AA}^{-1}$  around  $\bar{\Gamma}$  (black curve) and at  $0.65 \text{ \AA}^{-1}$  (red curve) as is indicated by the black and red lines in d) [37].

Investigations using spatially resolved ARPES with a spot size of  $\sim 10\text{-}20 \mu\text{m}$  combined with photoemission electron microscopy (PEEM) and photoemission spectroscopy (XPS) were performed to distinguish between the two surface terminations. An according dataset is shown in Figure 3.9 [26].

The combination of XPS and PEEM measurements reveal surface patches with different termination having a size between  $10 \mu\text{m}$  and  $40 \mu\text{m}$ . It was reported that at all investigated surface positions, small cracks and spurious areas are present, Figure 3.9 c) [26]. ARPES measurements showed two different gap sizes for the two reconstructions. The sodium terminated,  $(1 \times 1)$ -reconstructed surface was shown to have a gap of  $\sim 0.4$  eV, while the iridate terminated,  $(\sqrt{3} \times \sqrt{3})R30^\circ$ -reconstructed surface, has a gap of  $\sim 1.0$  eV. The interpretation of this difference is based on doping in the context of the Mott physics in the system. Both, iridium and sodium atoms in  $\text{Na}_2\text{IrO}_3$  donate valence electrons to the oxygen atoms. If sodium atoms are locally missing (e.g. at the iridate terminated surface), fewer electrons will be donated. It

was argued that due to electron correlations, different electron donation leads to a qualitatively different DOS, indicated by the pre-edge peaks in Figure 3.9 f) B. This pre-edge DOS was attributed to the emergence of a quasiparticle density of states appearing close to the Fermi level (Figure 3.9 f), effectively reducing the size of the Mott gap, resulting in termination dependent Mott gap size [26].

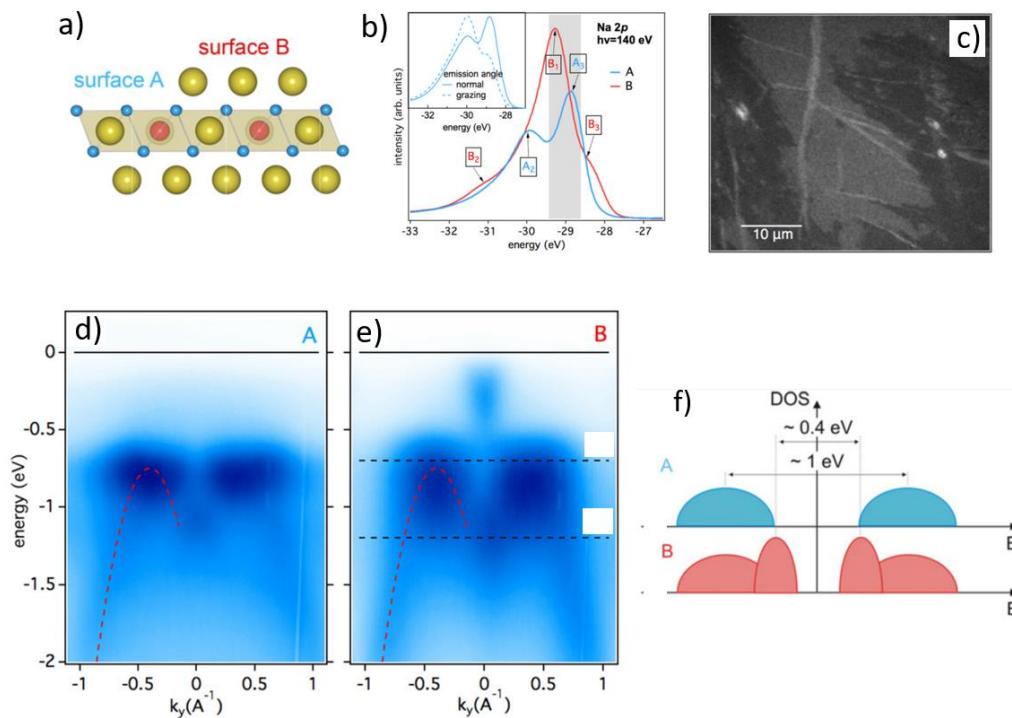


Figure 3.9 Spatially resolved ARPES results on the two different  $\text{Na}_2\text{IrO}_3$  surface reconstructions. Distinguishing between the two reconstructions was done using XPS and PEEM. a) Classification of the terminations. “A” = iridate terminated, “B” = sodium terminated. b) XPS Na-2p spectra used to distinguish between the terminations. c) PEEM image of the  $\text{Na}_2\text{IrO}_3$  surface. The energy window of the photoelectrons is indicated by the shaded grey area in b). d), e) Valence band dispersion measured with spatially resolved ARPES for the  $(\sqrt{3}\times\sqrt{3})R30^\circ$ -reconstructed surface (“A”) and the  $(1\times 1)$ -reconstructed surface (“B”) at the  $\Gamma$ -point. Even though the latter dataset seems to have a non-zero density of states up to the Fermi level, an open Mott gap was reported to be apparent. f) Estimated gap size for the two different terminations. From [26].

An alternative method to investigate the termination dependent surface electronic structure is scanning tunnelling microscopy (STM) and spectroscopy (STS). A dataset showing such an investigation on the freshly cleaved  $\text{Na}_2\text{IrO}_3$  surface in UHV is depicted in Figure 3.10.

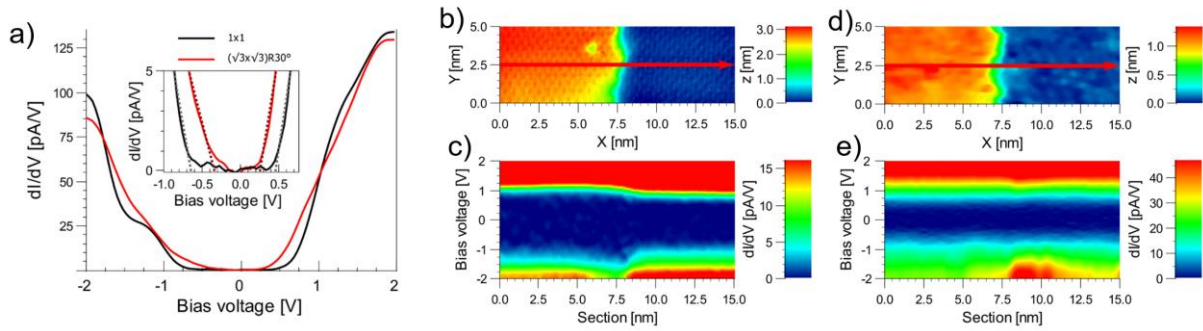


Figure 3.10 Investigation of the surface electronic properties of  $\text{Na}_2\text{IrO}_3$  by means of STM and STS. a) Differential conductivity spectra for both terminations as marked in the inset above. The inset itself depicts a zoom-in revealing gaps of  $\sim 1.2$  eV for the (1x1)- and  $\sim 0.6$  eV for the  $(\sqrt{3}\times\sqrt{3})\text{R}30^\circ$ -reconstructed surface, in contrast to the ARPES findings, where the larger gap was found for measurements on the (1x1)-reconstructed surface. b) STM constant current topography across a step edge separating two (1x1)-reconstructed surfaces. c) Differential conductivity spectra along the red line in a), showing the gap to remain apparent across the step edge. d) STM constant current topography across a step edge separating two  $(\sqrt{3}\times\sqrt{3})\text{R}30^\circ$ -reconstructed surfaces. e) Differential conductivity spectra along the red line in d), again showing a gap across the step edge. Adapted from [18].

The (1x1)-reconstructed surface was reported to have a Mott gap of  $E_{\text{Mott}} \approx 1.2$  eV, where for the  $(\sqrt{3}\times\sqrt{3})\text{R}30^\circ$ -reconstructed surface it is  $E_{\text{Mott}} \approx 0.6$  eV, Figure 3.10 a). These values are higher than the ones obtained by ARPES and photo conductivity [18], [19], [26]. Additionally, STS reveals that the sodium terminated surface has the larger Mott gap, where spatially resolved ARPES assigned the larger gap to the iridate terminated surface. An advantage of STM/STS investigations is the ability to probe the surface on an atomic scale, allowing for examinations of local structures like step edges. According data is depicted in Figure 3.10 b)-e), showing that the Mott gap remains apparent, independently of the termination of the terraces adjacent to the respective step edge. Hence, no in-gap states were found by means of STS, i.e. no hallmark of topologically insulating behaviour was observed.

In summary, the picture regarding the electronic properties of the  $\text{Na}_2\text{IrO}_3$  surface remains unclear as both, an apparent Mott gap and in-gap states were reported. Furthermore, the quantitative size of the reported Mott gaps varies considerably among the different investigations, making interpretations of the findings difficult. Transport measurements on freshly cleaved surfaces were not yet performed to the best knowledge of the author. In the context of topology, only the ARPES data presented in Figure 3.8 a)-c) point to metallic surface conductance accompanied by a linear dispersive band gap closing that might suggest a topologically non-trivial phase in  $\text{Na}_2\text{IrO}_3$ . Up to this point,  $\text{Na}_2\text{IrO}_3$  is predominantly viewed as a trivial Mott insulator [18], [26]–[28], [30], [37], [61], [62].

## 4 Supplementary Experimental Data of Na<sub>2</sub>IrO<sub>3</sub>

This chapter covers experimental results that are not directly related to the Na<sub>2</sub>IrO<sub>3</sub> bulk or surface electronic structure but are important in the context of the experimental work conducted for this thesis.

### 4.1 Electronic Transport Properties of the Na<sub>2</sub>IrO<sub>3</sub> Bulk

Transport measurements firstly evidenced that Na<sub>2</sub>IrO<sub>3</sub> does not show metallic conductance. Such macroscopic bulk electronic transport measurements were performed by multiple groups [28], [37], [62], [63] and a representative dataset is shown in Figure 4.1. Both, in-plane (Figure 4.1 a) and out-of-plane (Figure 4.1 d, e)) conduction was shown to be mediated by 3D variable range hopping (VRH) below 300 K, identified by the characteristic  $R \propto \exp(T^{-1/4})$  temperature dependence of the materials resistivity, as seen in Figure 4.1 c).

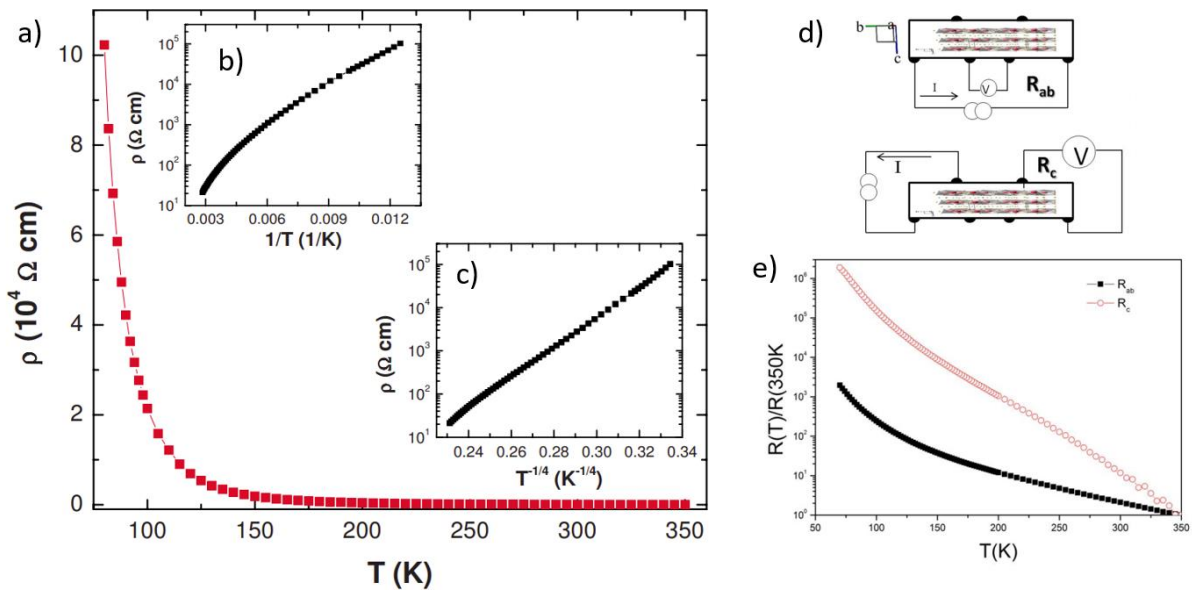


Figure 4.1 Macroscopic electronic transport characteristics of Na<sub>2</sub>IrO<sub>3</sub>. a) Resistivity versus temperature measured for a Na<sub>2</sub>IrO<sub>3</sub> single crystal in crystallographic ab-direction (in-plane). The insets show the same data in a  $\ln(\rho)$  vs  $1/T$  plot (b)) and a  $\ln(\rho)$  vs  $1/T^{1/4}$  plot (c)). The plot in c) shows a nearly linear behaviour with deviation from this linearity at high temperatures. This indicates a dominant 3D variable range hopping mechanism below room temperature. d) Schematic of the setup for comparative in-plane and out-of-plane resistance measurements. e) Data taken with the measurement geometry depicted in d), plotted in a semi-log plot. The out-of-plane resistance is higher by two to three orders of magnitude compared to the in-plane resistance [63].



VRH conductance arises from electron hopping between localized states in a narrow energy interval around the Fermi level (for details, see chapter 5.7.3). Since  $\text{Na}_2\text{IrO}_3$  exhibits a Mott gap, no Ir 5d states are expected to be available for VRH at the Fermi level. It is disputed which states mediate the VRH conduction, with impurity states being mostly proposed [63], [64].

At higher temperatures, the resistivity shows a  $R \propto \exp(T^{-1})$  dependence on the temperature (Figure 4.1 b)), that was assigned to a thermal excitation effect similar to the case for intrinsic semiconductors. The thermal excitation ansatz allows for the extraction of an excitation energy above 300 K, which was quantified to  $E_g \approx 350$  meV [44], [63], being in accordance with the size of the Mott gap reported from ARPES and optical conductivity measurements [19].

The out-of-plane transport characteristics are similar, but with the absolute resistivity being two to three orders of magnitude higher compared to the in-plane resistivity, as shown in Figure 4.1 e). The anisotropic crystal structure was reported as the reason for this enhanced out-of-plane resistivity [63].

## 4.2 Chemical Instability of $\text{Na}_2\text{IrO}_3$ in Air

The investigation of the  $\text{Na}_2\text{IrO}_3$  surface requires pristine surfaces that are neither contaminated nor chemically degenerated. In the process of synthesis, pre-characterization and preparation for further measurements, the exposure of the  $\text{Na}_2\text{IrO}_3$  samples to ambient air is not avoidable. This is particularly relevant as degeneration of sodium iridate under the simultaneous exposition to  $\text{H}_2\text{O}$  and  $\text{CO}_2$  was reported, where ambient air concentrations are sufficient to cause substantial damage to the material, as X-ray diffraction spectroscopy revealed (see Figure 4.2) [65].

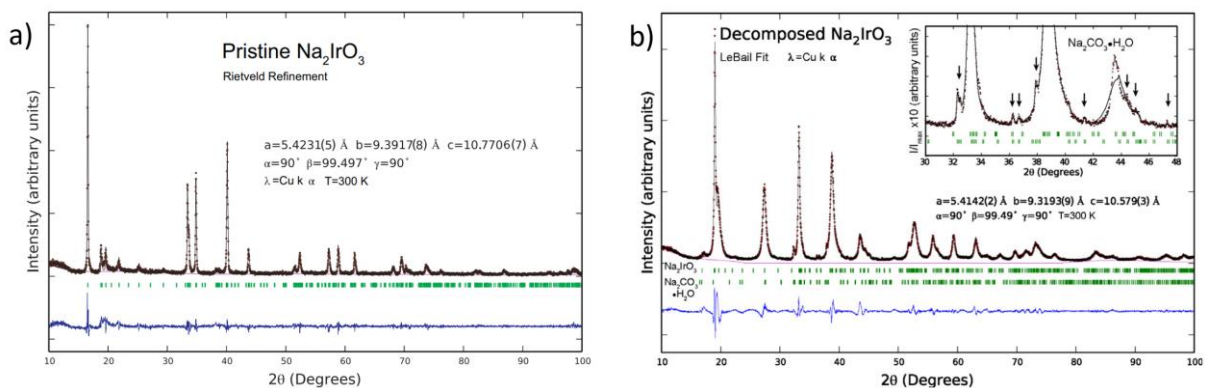


Figure 4.2 XRD-spectra taken on  $\text{Na}_2\text{IrO}_3$  at room temperature. a) Measurement on pristine  $\text{Na}_2\text{IrO}_3$  in Ar-atmosphere. b) Measurement on fully decomposed  $\text{Na}_2\text{IrO}_3$  that was left in air, showing a peak broadening as well as additional peaks. The peaks marked with a black arrow (zoom-in in the inset) were attributed to a  $\text{Na}_2\text{CO}_3 \cdot \text{H}_2\text{O}$  phase emerging upon decomposition of the sample.

It was proposed that degenerated  $\text{Na}_2\text{IrO}_3$  consists of a mixture of  $\text{Na}_2\text{CO}_3 \cdot \text{H}_2\text{O}$  and Na deficient sodium iridate. The degeneration of  $\text{Na}_2\text{IrO}_3$  powder begins immediately in air and full decomposition is observed within  $\sim 20$  h [65].

### 4.3 Surface Modification due to Effusion of Na from the $\text{Na}_2\text{IrO}_3$ Bulk to the Surface

From combined atomic force microscopy (AFM) and energy-dispersive X-ray spectroscopy (EDX) measurements, it was reported that clusters of material form on the freshly cleaved  $\text{Na}_2\text{IrO}_3$  surface in air [66]. These clusters grow over time, as is shown in Figure 4.3.

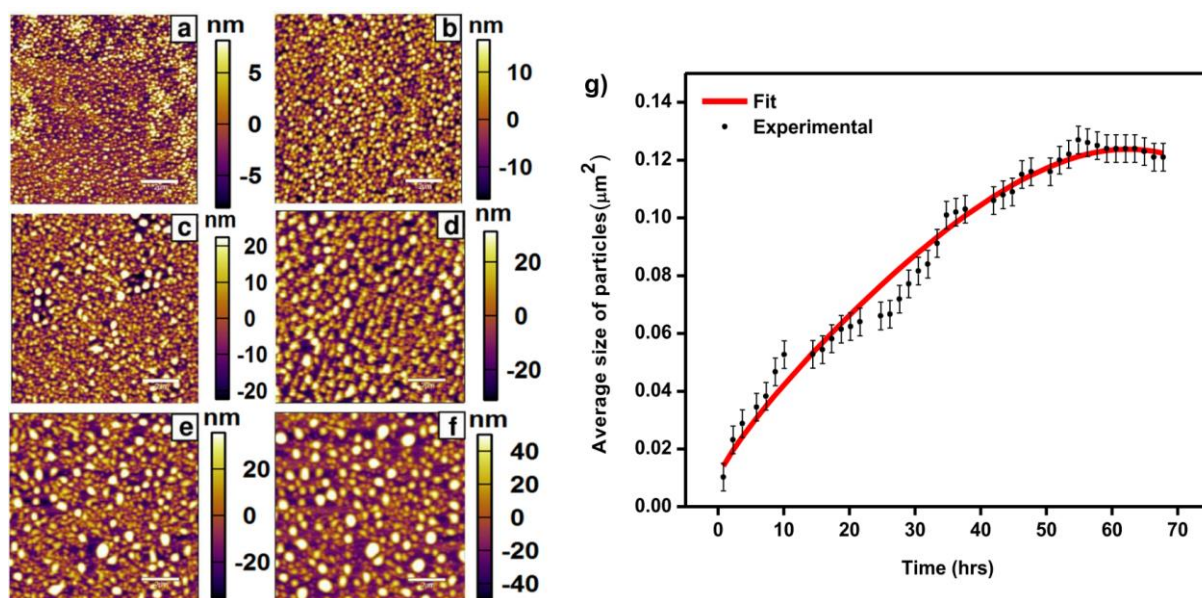


Figure 4.3 Formation of clusters on the freshly cleaved  $\text{Na}_2\text{IrO}_3$  surface in air. a)-f) AFM topographies on the  $\text{Na}_2\text{IrO}_3$  surface after cleaving (a), 10h after cleaving (b), 20h after cleaving (c), 30h after cleaving (d), 40h after cleaving (e) and 50h after cleaving (f). Over time, the clusters grow in size. This growth is displayed in g), showing the evolution of cluster cross section area parallel to the sample surface.

As depicted in the AFM-topographies in Figure 4.3 a)-f), small clusters emerge directly after cleaving in air. The size of these clusters grows over time, reaching a saturation at cluster cross sections of  $\sim 12 \mu\text{m}^2$  after  $\sim 50$  h. Subsequent conductivity measurements of the clusters using conductive AFM cantilevers showed metallic conductance of the clusters [66]. Combined with EDX-investigations, it was argued, that the clusters consist of sodium effusing from the  $\text{Na}_2\text{IrO}_3$  bulk to the surface [66].

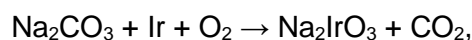


## 5 Introduction to the Experimental Methods

In the following the experimental methods used in the scope of this work are presented. This chapter is arranged according to the consecutive steps being performed practically, beginning with the crystal synthesis and characterization done by Ina-Marie Pietsch in the group of P. Gegenwart at the Augsburg University. Afterwards, the sample preparations for both, the macroscopic transport measurements and microscopic scanning tunnelling investigations are described. This is followed by an introduction to scanning tunnelling microscopy as well as the used STM methods. The chapter is closed with a description of the technical realization and methodology of the transport measurements as well as an overview over applicable transport phenomena.

### 5.1 Sample Synthesis of $\text{Na}_2\text{IrO}_3$

Investigations using STM methods as well as macroscopic conductivity measurements require single crystals of sufficient size ( $>0.5$  mm in diameter) and high quality. Suitably sized  $\text{Na}_2\text{IrO}_3$  single crystals cannot be directly grown from the educts. Instead, polycrystalline  $\text{Na}_2\text{IrO}_3$  powder is produced in a first step that serves as source material for the aspired large single crystals. The  $\text{Na}_2\text{IrO}_3$  powder is synthesised using the solid-state reaction method in an open furnace [28]. High purity  $\text{Na}_2\text{CO}_3$  is mixed with Ir powder in a 1.05:1.0 ratio and grinded for several minutes before being heated in an alumina ( $\text{Al}_2\text{O}_3$ ) furnace. Primary calcination reaction is done at  $800^\circ\text{C}$  and therefore below sodium iridates melting temperature of  $823^\circ\text{C}$ , being described by:



where the additional oxygen on the educts side is provided by the surrounding ambient air. The excess  $\text{CO}_2$  volatilises into the surrounding atmosphere. Subsequently, the material is grinded repetitively and heat treated at successively higher temperatures of up to  $900^\circ\text{C}$ . Details on this process can be found in [28], [31].

To grow large single crystals, 10 % (atomic %)  $\text{IrO}_2$  is mixed to the  $\text{Na}_2\text{IrO}_3$  powder. The material is then heated again in an alumina crucible to  $1050^\circ\text{C}$  and held at this temperature for up to two weeks, before cooling back to room temperature. The resulting plate-shaped, shiny, black crystals grow vertically out of the powder as seen in Figure 5.2. Since they are stacked on each other in random angles, the crystals need to be separated with sharp tools, occasionally resulting in breaking of crystals or marks on the facets. Diameters of up to a few

millimetres in the crystallographic a-b-direction (in-plane) and thicknesses of usually around 100  $\mu\text{m}$  in the c-direction (out of plane) are achieved [28], [31].



Figure 5.1: Plate shaped sodium iridate crystals grown out of  $\text{Na}_2\text{IrO}_3$  powder during the synthesis. Suitably large and stable crystals are harvested for investigation. Usual sizes are a few millimetres in diameter and thicknesses of around 0.1 mm.

## 5.2 Sample Pre-Characterization via XRD and SQUID

Sodium iridate is prone to defects like stacking faults that may have a considerable impact on the sample quality. To provide good quality, crystals are hand-picked considering their macroscopic shape. Small crystals and crystals with deformations or cracks are discarded after synthesis.

Detailed structural pre-characterization is done using X-ray diffractometry (XRD), where the diffraction of incident radiation at the samples crystallographic planes yields information about the lattice structure as well as defects like stacking faults according to Bragg's law [67]. The occurrence of defects that impact the lattice periodicity only in a minor way are difficult to identify using XRD-methods alone. For further examination of the sample quality, the structural analysis is complemented by measurements of the magnetic susceptibility with a superconducting quantum interference device (SQUID) over a large temperature range, covering the regimes below and above the Néel temperature  $T_N$ , below which  $\text{Na}_2\text{IrO}_3$  enters the antiferromagnetic phase. Generally, the magnetic exchange interaction is described via competing Heisenberg and Kitaev type interaction, where the distortion of the  $\text{IrO}_6$  octahedra results in a deviation from the Kitaev-ideal [16], [68], [69]. Such distortions are influenced by nearby defects, and a high  $T_N$  indicates low distortions of the  $\text{IrO}_6$  octahedra and good crystal quality. The Néel-Temperature varies between 13 K and 18 K [28], [33], [70] depending on crystal quality [30]. In the scope of this work, values for  $T_N$  above 15 K are considered sufficiently good. Datasets showing XRD and magnetic susceptibility data for a  $\text{Na}_2\text{IrO}_3$  sample are depicted in Figure 5.2.

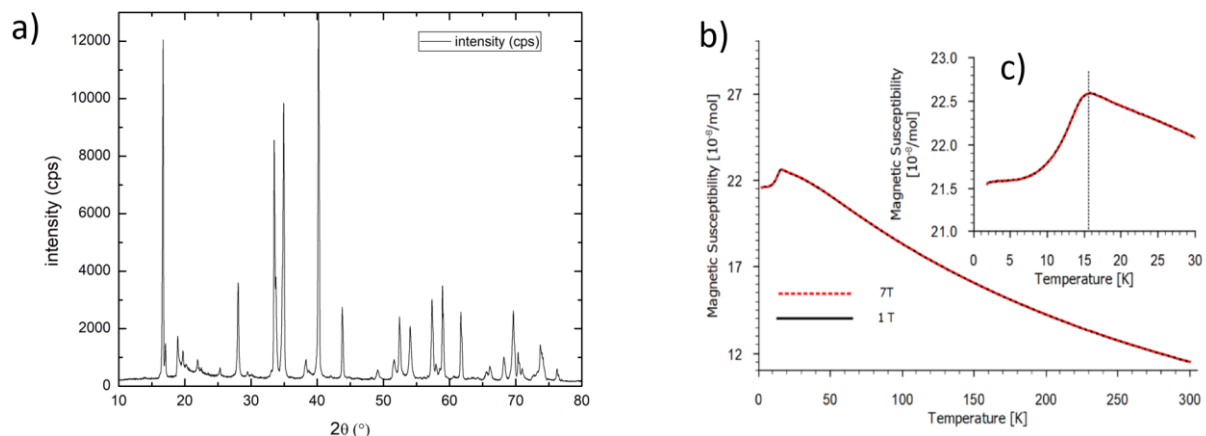


Figure 5.2 Examinations of the  $\text{Na}_2\text{IrO}_3$  sample quality using XRD and SQUID. a) XRD-spectrum of a  $\text{Na}_2\text{IrO}_3$  sample considered to have good quality. The reflection peaks are sharp and distinct. b) Temperature dependent in-plane magnetic susceptibility of  $\text{Na}_2\text{IrO}_3$ , between 1.8 K and 300 K for 1 T (black line) and 7 T (dashed red line). c) Zoom-in on the sharp feature around  $T_N = 15\text{-}16$  K from (a), confirming good crystal quality.

XRD and SQUID measurements were performed in the group of P. Gegenwart at the Augsburg University. For XRD investigations, a FDI NTX from Photonic Science using a Philips PW 1830 X-ray generator was used with acceleration voltages between 10 kV and 30 kV and a current of 30 mA. The magnetic susceptibility measurements were done using a MPMS3 (Magnetic Property Measurement System) from Quantum Design.

### 5.3 Sample Preparation

The sample preparation varies depending on the intended measurement. Surface sensitive examinations require crystal cleaving in UHV, as the chemical instability of sodium iridate degenerates any surfaces that were simultaneously in contact with  $\text{CO}_2$  and  $\text{H}_2\text{O}$  [65]. Both, STM and transport measurements require electrical contacting, where a single contact is sufficient for STM. Even though transport measurements need at least two contacts, four contacts (two on top and two at the bottom of the respective plate-shaped sample) were applied. This geometry allows for reference measurements after the crystal is cleaved, as only the top pair of contacts is influenced by such a cleave. In the following, the sample preparation for both measurement methods is described.

### 5.3.1 Sample Preparation for STM Measurements

Single-tip STM requires the ability to apply a bias voltage to the sample and a sufficiently high conductivity of the probed material to establish a tunnelling current. For temperatures  $\geq 77$  K, the conductivity of  $\text{Na}_2\text{IrO}_3$  is high enough. It is therefore sufficient to contact the crystal on its backside by gluing it to a substrate using conductive epoxy and ensure electric contact of the epoxy layer to the measurement electronics. As substrates, copper blocks and Macor plates were used. The epoxy was applied in liquid form and dried for one hour at  $150^\circ\text{C}$  in air. The same procedure was used to apply a cleaver on the top side of the crystal. Steel rods of 1 cm length and a diameter of 1 mm were used as cleaver. A picture of the geometry is shown in Figure 5.3. To minimize the time under ambient air, all samples were stored in a desiccator at a pressure of  $\sim 10^{-3}$ - $10^{-2}$  mbar before transferring them to the designated UHV-chamber for STM measurements.

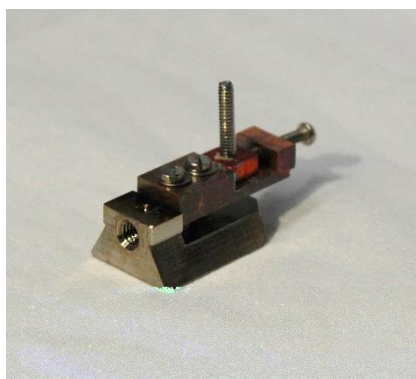


Figure 5.3 Sample holder with sample prepared for cleaving.

To mount and transport the samples within the UHV-chambers, a home-build, standardized dovetail geometry was used, see Figure 5.3. This system allows for sample transfer across interconnected UHV-chambers as well as placement into a probing stage without the application of any forces to the sample.

### 5.3.2 Sample Preparation for Transport Measurements

For transport measurements a refined method to attach contacts is used. Instead of conductive epoxy, four high-purity gold contacts are grown using gold evaporation from a tungsten

crucible. The first two contacts are directly grown onto the Macor substrate using shadow masks. Afterwards, epoxy is applied on the substrate between the contacts, and the sample is pressed on the glue using a clamp. Here, non-conductive epoxy is used to avoid a shorting of the contacts. Before letting the epoxy dry out, the electrical contact between the gold patches - bridged by the sample - is measured. This measurement is re-done after the epoxy hardened.

In the next step, a second set of shadow masks is used, protecting the sample and the already existing contacts. With this, the two top contacts are evaporated on top of the package, leaving enough space on the top side of the sample for the application of a cleaver. In this work, a contact-contact spacing of 1 mm was used.

Electrical contact of all four gold patches with the sample is checked using a multimeter at room temperature, where a resistance below  $10\text{ k}\Omega$  between two contacts is accepted. Afterwards, the cleaver is glued on top of the sample in the centre between the top gold contacts using again non-conductive epoxy. Conductive glue needs to be avoided to enable reference transport measurements before cleaving the crystal.

An overview of the geometry is depicted in Figure 5.4.

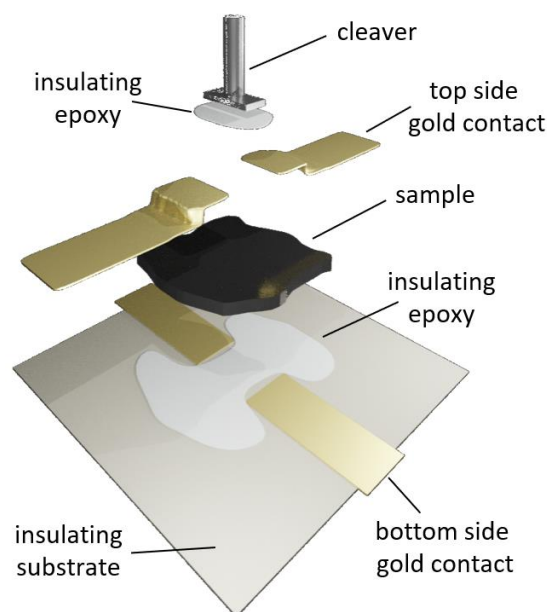


Figure 5.4 Overview over the contact and cleaver geometry for transport measurements on  $\text{Na}_2\text{IrO}_3$ .

After preparation, the samples are stored in a desiccator to minimize air exposure. Including all steps, the average time of any sample in ambient air is  $\sim 5$  hours.

Before finally transferring a sample to a UHV-chamber, the substrate is attached to a sample holder with the standard dove-tail design. Here the dovetail is segmented, and each gold contact is electrically connected to its own single segment via a screw. This design allows for easy contacting in the UHV chamber to employ transport measurements. The whole sample holder setup is depicted in Figure 5.5.

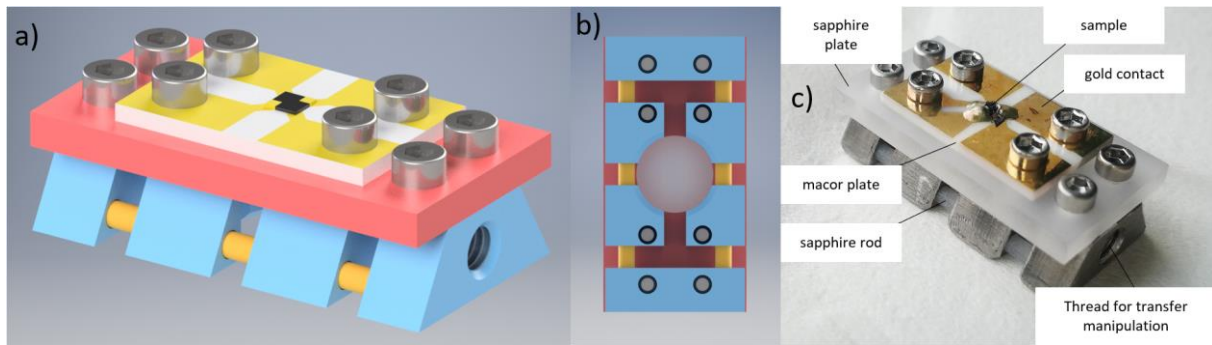


Figure 5.5 Overview over the sample holder and contact setup used for transport measurements. a) Angled view of a sample holder with contacted sample. Blue: dovetail segments, red: sapphire plate to enhance thermal coupling, dark yellow: sapphire rod to enhance mechanical stability, white: insulating substrate, gold: gold contacts attached to the sample and connected to the dovetail segments via screws, black: sample. b) Bottom view of the setup in a). The central round cut-out in the middle dovetail segments is only for technical inter-compatibility purposes. c) Photograph of a sample prepared in accordance to a).

## 5.4 Crystal Cleaving

Crystal cleaving was done under vacuum conditions at a base pressure of  $10^{-9}$  mbar by applying a lateral force to the cleaver. The required force is slightly different for every sample. This is intuitive, as the sample size and geometry should influence the needed force. Consequently, at any cleaving attempt the applied force to the cleaver is raised gradually until the crystal cleaves. A cleaved sample is depicted in Figure 5.6.



Figure 5.6 Cleaved  $\text{Na}_2\text{IrO}_3$  sample for transport measurements. On the left, the contacted sample mounted on the holder for transport measurements is seen. On the right, the hole-base with cleaver and second half of the sample is visible.

To check for a good cleave in UHV, both halves of the sample are preserved. To ensure that the resulting sample halves do not touch each other after cleaving (avoidance of contact induced damages of the fresh surface), a special holder (“hole base”) is used, where the cleaver can be threaded in (see Figure 5.6) and fixed after cleaving. With this, both halves of the sample can be checked visually in-situ and in detail after transferring out of the UHV chamber. The geometry of the hole base and the used cleaver rods was chosen in a way that makes it usable for STM investigations, i.e. both crystal halves can be used for STM if desired. To avoid long delays of the overall measurement process, multiple samples were prepared for each measurement. As it turns out, around 1 in 3 samples cleave appropriately.

## 5.5 Scanning Tunnelling Microscopy

The invention of the scanning tunnelling microscope (STM) by Gerd Binnig and Heinrich Rohrer in 1982 enabled real space measurements on the nanoscale for the first time, opening up new research fields in surface science and solid-state physics [71]. This breakthrough was awarded the Nobel Prize in physics just four years later and laid the foundation for various other scanning probe methods, e.g. the atomic force microscopy [72]. The fundamental working principle behind STM measurements is the quantum mechanical tunnelling effect, where a particle may pass through a potential barrier if the barrier is sufficiently narrow. Conventional tunnelling experiments use a thin insulating layer serving as such a potential barrier between two conductive materials [73]. Similarly, in STM the positioning of a conductive tip in close proximity to a conductive sample and the application of a bias voltage between both results in a tunnelling current  $I_T$ . Since the decay of  $I_T$  with increasing tip-sample-distance  $d$  is exponential, the width of the tunnelling barrier is usually smaller than  $d = 1$  nm in the



experiment. This exponential relation not only allows for precise height adjustments of the probe, but also results in atomic lateral resolution for atomically sharp probes.

The experimental requirements for the motion of the probe relative to the sample are met using piezoelectric crystals accompanied by sophisticated damping setups. If required, this is paired with cooling to low temperatures, further enhancing the stability of the measurement.

### 5.5.1 STM Theory

The basic phenomenon underlying STM efforts is the quantum mechanical tunnel effect. Even though the most important requirement for the tunnelling process is the availability of an unoccupied electron state behind the potential barrier, experimentally usable electric currents require the barrier to be sufficiently small and narrow. In a rather simple one-dimensional approach, the corresponding transmission coefficient  $T$  is given by:

$$T \propto e^{-2d\sqrt{\frac{2m}{\hbar^2}(\phi-E)}} , \quad 5.1$$

with the barrier width  $d$ , the barrier height  $\phi$ , the electron mass  $m$  and the electron energy  $E$  [74]. Equation 5.1 provides an estimation of the involved dimensions. Assuming for example  $\phi = 4$  eV (i.e. a typical ionization energy) and  $E = 1$  eV (corresponds to 1 V applied to the tunnelling junction), increasing the tip-sample distance - and therefore the barrier width - by 0.1 nm results in a decrease of  $T$  by ~87 %. This sensitive  $T$ - $d$ -dependence is the reason for the atomic resolution obtained with STM techniques and immediately displays the need to position the probe extremely close to the sample (usually  $d \leq 1$  nm).

Originally starting with the transfer-Hamiltonian ansatz on macroscopic tunnel junctions between two metal electrodes, Bardeen formulated the transfer matrix element:

$$M_{\mu\nu} = -\frac{\hbar^2}{2m} \int_S [\psi_\mu^* \nabla \psi_\nu - \psi_\nu \nabla \psi_\mu^*] dS , \quad 5.2$$

with the sample wavefunctions  $\psi_\mu^*$  and the tip wavefunction  $\psi_\nu$ , providing the transition probability [75], [76]. The integration is done over a surface  $S$  within the tunnelling junction separating tip and sample, as depicted in Figure 5.7 (further information is found in [77]).



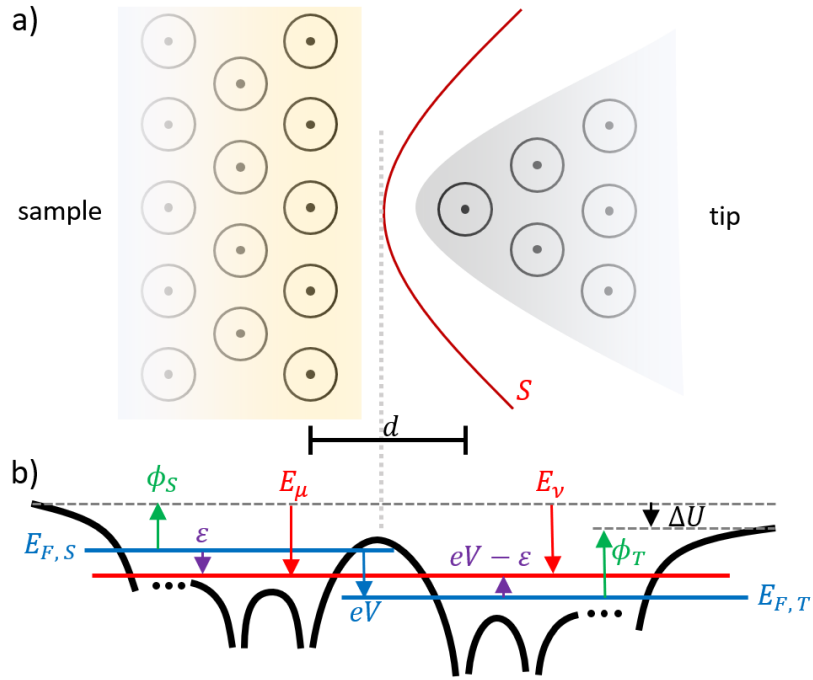


Figure 5.7 a) Scheme of the perturbation ansatz formulated by Bardeen, where the system is described by the tip- and sample as subsystems separated by the surface  $S$ . b) Scheme of the potential landscape of the whole system, visualizing all involved parameters. Adapted from [77].

With the transfer matrix element, the tunnelling current is given by [76], [78]:

$$\begin{aligned}
 I_T(V) &= \frac{2\pi e}{\hbar} \sum_{\mu,\nu} [f(E_\mu) - f(E_\nu)] |M_{\mu\nu}|^2 \delta(E_\nu + V - E_\mu) \\
 &\approx \frac{2\pi}{\hbar} e^2 V \sum_{\mu,\nu} |M_{\mu\nu}|^2 \delta(E_\mu - E_F) \delta(E_\nu - E_F),
 \end{aligned}
 \tag{5.3}$$

with the Fermi-Dirac distribution  $f(E)$  and the applied voltage  $V$ . The approximation in equation 5.3 is only valid for small voltages, where the summands equal the transfer rates provided by Fermi's golden rule [78]. The sum can be replaced by an integral over the tip and sample densities of states  $\rho_T$  and  $\rho_S$ , respectively [77]:

$$I_T(V) \propto \int [f_s(\epsilon - eV) - f_t(\epsilon)] \rho_S(\epsilon - eV) \rho_T(\epsilon) |M(\epsilon, eV)|^2 d\epsilon.
 \tag{5.4}$$

However, this needs to be taken with a grain of salt as it simplifies the transition matrix element (equation 5.2) to a function of energy only. Further conceptual development was provided by Tersoff and Hamann by taking the actual tip-sample geometry of the STM tunnel junction into account. To represent the sharp tip, a spherical s-orbital was modelled to the position  $\mathbf{r}_0$  of the

tip apex. For small voltages and low temperatures, the tunnelling current can then be related to [76]

$$I_T(V) \propto V \rho_S(E_F, \mathbf{r}_0) , \quad 5.5$$

i.e. the tunnelling current is linearly proportional to the applied voltage  $V$  times the local density of states (LDOS) of the sample  $\rho_S$ . Here, the matrix elements  $M$  are constant and therefore energy independent. This does not hold for significant voltages and is handled in the Hamers model by replacing the matrix element with an energy and distance dependent transmission term, i.e.  $|M(\epsilon, eV)|^2 \rightarrow T(\epsilon, eV, d)$  [79]. Using the Wentzel-Kramers-Brillouin (WKB) approximation, this transmission term was found to be [79]:

$$T(\epsilon) = \exp\left(-\frac{2d\sqrt{2m}}{\hbar} \sqrt{\frac{\phi_S + \phi_T}{2} + \frac{eV}{2} - \epsilon}\right) . \quad 5.6$$

With the work function of tip and sample,  $\phi_T$  and  $\phi_S$ , the tunnel current is then:

$$\begin{aligned} I_T(V) &\propto \int_0^{eV} [f_S(\epsilon - eV) - f_T(\epsilon)] \rho_S(\epsilon - eV, r) \rho_T(\epsilon, r) T(\epsilon, eV, d) d\epsilon \\ &\approx \int_0^{eV} \rho_S(\epsilon - eV, r) \rho_T(\epsilon, r) T(\epsilon, eV, d) d\epsilon , \end{aligned} \quad 5.7$$

where the integral goes over the energy corresponding to the applied bias voltage. With this expression, the STM-methods described in the subsequent chapters can be understood. A complete discussion on the tunnelling theory and its applications is found in the books of Bonnell, Chen and Voigtländer instructive [77], [78], [80], giving an deeper insight into the matter.

### 5.5.2 Role of the STM Tip Orbital

To model the STM tip with an s-orbital at the apex as introduced by Tersoff and Hamann, resulting in equation 5.7, is an approximation that does not reflect any situation for real STM tips. If knowledge on the tip wavefunctions is available, the transition matrix element  $M_{\mu\nu}$  (equation 5.2) can be determined quantitatively. Then, it is possible to simplify  $M_{\mu\nu}$  by using the so-called derivative rule [77], where the wavefunction of the tip apex atom is described as Green's function to transition the integral in equation 5.2 into an expression that is only

dependent on the wavefunctions decay constant in vacuum  $\kappa = \sqrt{2m\phi}/\hbar$  with the work function  $\phi$ , and the sample wavefunction  $\psi_{\mu}^*$  (i.e.  $\psi$  in Table 5.1) at the centre of the tip-apex atom  $\mathbf{r}_0$ . The resulting expressions for the transfer matrix elements for s-, p- and d-tip-orbitals are summarized in Table 5.1.

Table 5.1 Real transfer matrix elements for different tip wavefunctions of the apex atom at position  $\mathbf{r}_0$ .  $\kappa$  denotes the decay constant in vacuum,  $\psi$  is the sample wavefunction and  $C$  a constant. From [77].

Tip state	Matrix element
$s$	$\frac{2\pi C\hbar^2}{\kappa m} \psi(\mathbf{r}_0)$
$p_z$	$\frac{2\pi C\hbar^2}{\kappa m} \frac{\partial \psi}{\partial z}(\mathbf{r}_0)$
$p_x$	$\frac{2\pi C\hbar^2}{\kappa m} \frac{\partial \psi}{\partial x}(\mathbf{r}_0)$
$p_y$	$\frac{2\pi C\hbar^2}{\kappa m} \frac{\partial \psi}{\partial y}(\mathbf{r}_0)$
$d_{zx}$	$\frac{2\pi C\hbar^2}{\kappa m} \frac{\partial^2 \psi}{\partial z \partial x}(\mathbf{r}_0)$
$d_{zy}$	$\frac{2\pi C\hbar^2}{\kappa m} \frac{\partial^2 \psi}{\partial z \partial y}(\mathbf{r}_0)$
$d_{xy}$	$\frac{2\pi C\hbar^2}{\kappa m} \frac{\partial^2 \psi}{\partial x \partial y}(\mathbf{r}_0)$
$d_{z^2 - \frac{1}{3}r^2}$	$\frac{2\pi C\hbar^2}{\kappa m} \left( \frac{\partial^2 \psi}{\partial z^2} - \frac{1}{3} \kappa^2 \psi \right) (\mathbf{r}_0)$
$d_{x^2 - y^2}$	$\frac{2\pi C\hbar^2}{\kappa m} \left( \frac{\partial^2 \psi}{\partial x^2} - \frac{\partial^2 \psi}{\partial y^2} \right) (\mathbf{r}_0)$

As can be seen from Table 5.1, the tip state determines which derivative of the sample wavefunction at the tip-apex must be considered. Hence, depending on the combination of sample wavefunction and tip state, the transfer matrix element can take vastly different values for different tip states and even vanish for one tip state while it is non-zero for another tip-state.

### 5.5.3 Constant Current Topography

In constant current topography (CCT) measurements, while scanning, the tunnelling current for a given bias voltage is kept constant by adjusting the tip-sample distance. Consequently, by laterally scanning the probe over the sample one gets a map of constant current. Considering equation 5.7, this constant current contour equals a constant LDOS in the interval

[0, eV]. This is important, since CCT-examinations do not directly yield the surface morphology but can be used to identify this morphology in combination with theoretical work (e.g. density functional simulations). Another implication from equation 5.7 is, that the LDOS of the tip needs to be constant within the probed energy range to make the connection between the constant current contour and the surface morphology.

#### 5.5.4 Scanning Tunnelling Spectroscopy

Further insight to the energy dependent electronic structure can be gained by scanning tunnelling spectroscopy (STS). Here, at every probed lateral tip position above the sample surface, the scanning process is interrupted, and the tip height is adjusted according to the chosen current setpoint. Then, the bias voltage is swept through a given interval so that an energy sensitive  $I(V)$  curve is recorded. The local differential conductance is then given by the derivative of this  $I(V)$  curve. This in turn can be related to the energy resolved sample and tip LDOS's and the transmission probability  $T$  via the Hamers approximation:

$$\frac{dI_T}{dV}(V) \propto \rho_S(eV, r)\rho_T(0, r)T(eV, V, d) + \int_0^{eV} \rho_S(\varepsilon, r)\rho_T(\varepsilon - eV, r) \frac{dT(\varepsilon, eV, d)}{dV} d\varepsilon . \quad 5.8$$

For an energy independent tip LDOS and energy independent transmission probability, this simplifies to a proportionality of the obtained  $dI/dV$ -curves with the sample local density of states  $\rho_S$ :

$$\frac{dI_T}{dV}(V) \propto \rho_S(eV) . \quad 5.9$$

This expression must be handled with care for large voltages applied to the tunnelling junction, as then the voltage dependence of  $T$  cannot be neglected. This issue can be addressed by renormalizing the data via  $dI/dV \rightarrow (dI/dV)/(I/V)$  as proposed by Feenstra [81]. However, in the scope of this work this renormalization provides two pitfalls: firstly, for a vanishing conductivity, e.g. the bulk band gap of sodium iridate,  $(dI/dV)/(I/V)$  is not well defined. And secondly, for measurements containing tunnelling channels that are not "easily" explainable by the standard model,  $(dI/dV)/(I/V)$  may not be physically justified and could even introduce artifacts. The spectroscopic data presented in this work is therefore not renormalized and shown as  $dI/dV$  curves.

As mentioned above, the tip sample distance is set before each spectroscopy measurement according to the current and voltage setpoints. The current setpoint equals the integral over  $dI/dV$  from the voltage setpoint to 0 V. Hence, the LDOS (i.e.  $dI/dV$ ) within the interval between the voltage setpoint and 0 V impacts the initially adjusted tip-sample distance. This makes a comparison of different  $dI/dV$  data difficult, as potentially different tip-sample distances would have to be considered. To account for this, STS data can be normalized via [82]:

$$\frac{dI}{dV}(V, x, y)|_{d=d'} = \frac{dI}{dV}(V, x, y) \cdot e^{2\kappa(d(x,y)-d')}, \quad 5.10$$

with the decay constant in vacuum  $\kappa$  and the tip-sample distance  $d$ . The normalization projects the  $dI/dV$  data to a constant height contour  $d'$ . Such a projection is reasonable only for structurally flat surfaces, where the corrugation in constant current measurements arises from electronic contrast. Hence, at step edges or defects, a normalization according to 5.10 is not meaningful.

### 5.5.5 Barrier Height Spectroscopy

As stated in equation 5.7, the dependence of  $I_T$  on the tip-sample distance  $d$  stems from the transmission factor  $T$ . Consequently, in a tunnelling experiment where both, the lateral tip position and the voltage across the tunnelling junction is fixed, but the tip-sample distance  $d$  is varied, the tunnelling current will be proportional to  $T$  according to equation 5.6 to [80]:

$$\begin{aligned} I_T &\propto \int_0^{eV} \rho_S(\varepsilon - eV, r) \rho_T(\varepsilon, r) T(\varepsilon, eV, d) d\varepsilon \\ &= T(\varepsilon, eV, d) \int_0^{eV} \rho_S(\varepsilon - eV, r) \rho_T(\varepsilon, r) d\varepsilon \\ &\propto T(\bar{\Phi}, d) \propto \exp\left(-2d \sqrt{\frac{2m}{\hbar^2} \bar{\Phi}}\right), \end{aligned} \quad 5.11$$

with the average tunnelling barrier  $\bar{\Phi} = (\phi_S + \phi_T)/2$ . Consequently, measurements at the same lateral position while varying  $d$  yields an estimate for the apparent tunnelling barrier height, i.e. for the involved work functions.

### 5.5.6 Experimental STM Setup

The scanning tunnelling experiments in this work have been conducted with two different home-built STMs: one room temperature STM and one cooled STM (“Kryo-STM”) that is equipped with a LN2 and LHe cooling setup. Since the Kryo-STM is capable of everything the room-temperature setup allows, there will be no separate description for the room temperature STM.

The STM’s scanning unit is of the beetle type invented by Besocke [83]. A photograph of the unit is shown in Figure 5.8.

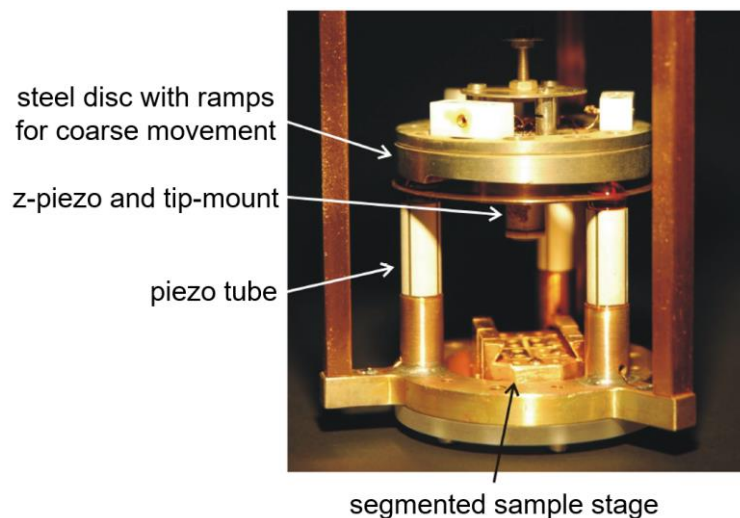


Figure 5.8 Beetle type scanning tunnelling measurement unit. Sample holders with a dovetail base are positioned in the segmented sample stage, allowing for multiple electrical contacts to the sample. Each of the three piezo tubes consists of four piezoelectric crystals, allowing for scanning and coarse movement of the steel disc resting on the piezo tubes. Coarse movement is achieved via ramps at the steel disc edge that translate tangential piezo-tube movement into coarse movement. STM tips are mounted to the z-piezo in the centre, providing fine movement of the tip perpendicular to the sample surface.

It has a segmented dovetail-negative at the bottom where sample holders are inserted via a manipulator. The segmentation allows for the usage of multiple contacts at the respective sample without losing mechanical or thermal stability. The segmented stage is surrounded by three piezo tubes that serve as rest for a steel disc. At the edges, the disc has ramps cut into the material. Depending on the type of piezo movement, two different disc-motion types are possible: lateral displacement in the horizontal plane (all piezo tubes simultaneously move in the same direction) and rotation of the disc (each piezo tube performs a slip-stick motion in tangential direction to the disc). The lateral displacement motion provides the scanning ability needed for STM. The rotation movement causes a vertical displacement of the disc due to the ramps and is used to approach the sample. The STM tip is mounted to another piezoelectric

crystal (“z-piezo”) at the centre of the bottom side of the disk. This additional piezo provides fine adjustment of the tip height, i.e. the tip-sample distance.

The beetle scanner setup is mounted to a reservoir of liquid helium or liquid nitrogen. By leaving the reservoir empty, measurements at room temperature are possible. The whole unit is situated within a gold-plated copper cup to shield it from outside thermal radiation. All cables are aligned along the coolant reservoir to avoid heating of the sample via those cables. Temperature measurements are done with a DT670 diode placed next to the sample stage. At equilibrium, a temperature of 8 K is reached when cooled with LHe.

The STM measurement unit is mounted within a UHV chamber that is evacuated by an ion-getter pump and a titanium sublimation pump. In combination with frequent baking-out of the chamber between measurement sessions, a pressure of  $<10^{-10}$  mbar is achieved. The chamber itself is supported by an air suspension to reduce low frequency vibrations. The inner coolant reservoir is additionally suspended with springs reducing high frequency vibrations.

To produce suitable conductive tips for the tunnelling experiments, polycrystalline tungsten rods with a diameter of 0.25 mm are etched in a KOH-solution, transferred into UHV and further prepared. The tips are heated to remove dirt and oxide from the tip apex. Afterwards, the tips are sputtered using an Argon beam to enhance their sharpness and to remove instable structures. This enhances both, the measurement resolution and its stability. Finally, the tip sharpness is checked using field emission to discard bad tips immediately. Suitable tips are transferred to the STM without leaving UHV conditions. A detailed description of the tip preparation can be found in [84]–[86].

### 5.5.7 STM Measurement Electronics

Like the general experimental STM setup, the according measurement electronics and the accompanying software are home-build. An overview over the electronics is depicted in Figure 5.9. The software runs on a conventional PC and a digital signal processor (DSP) card. PC, DSP and I/O board are galvanically isolated from the rest of the STM setup to inhibit electronic cross talk. All signals coming from the PC side are converted via digital analogue converters (DAC's) and all signals coming from the experiment side are converted via analogue digital converters (ADC's).

Piezoelectric crystals require high voltages for the desired movements, which is provided by using a high voltage amplifier having a range of -300 V to 300 V. At tip sample distances of a few angstroms, the resistance of the tunnelling junction is usually in the  $10^9\Omega$  range, resulting



in tunnelling currents that do not exceed a few nanoampere. An I/V-converter that converts  $1 \text{ nA} \rightarrow 1 \text{ V}$  is mounted as close as possible to the tunnelling junction but outside the UHV chamber. The voltage signal is transmitted to the DSP card that controls the z-piezo movement via a feedback loop. This setup allows to keep the tunnelling current at a given setpoint by adjusting the tip height. Combined with the scanning ability in the beetle design, all requirements for STM/STS measurements are met. A further in-depth description of the utilized STM setup can be found in [87].

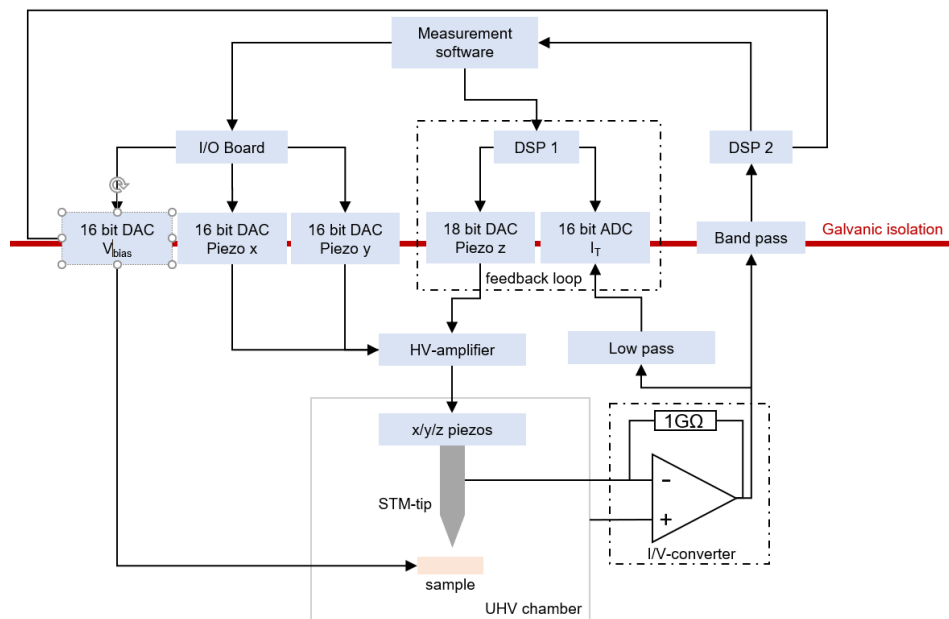


Figure 5.9 Scheme of the utilized STM-electronics. The upper part, including a PC running the measurement software, the I/O-board and the DSP's are situated in a separated control room and galvanically isolated from the rest of the experiment. The output voltage of the DSP's is amplified before addressing the piezoelectric crystals. The exception is the 16-bit DAC addressing the sample directly. Current passing the tunnelling junction is converted to a voltage. The resulting signal is used as input for the feedback-loop to adjust the tip-sample distance via the z-piezo. After [29], [88].

## 5.6 Transport Measurements

After preparation according to chapter 5.3.2, the samples were transferred to an UHV-chamber with a segmented stage, allowing to electrically contact the dovetail segments of the sample holder separately. The used chamber is the "Proben-Präparations-Shuttle I" (PPS I). The actual contacting is achieved via pins mounted to beryllium-copper springs to account for imperfect geometries of the sample holder as well as thermal contraction/expansion depending on the stage temperature. Photographs of the stage are depicted in Figure 5.10.

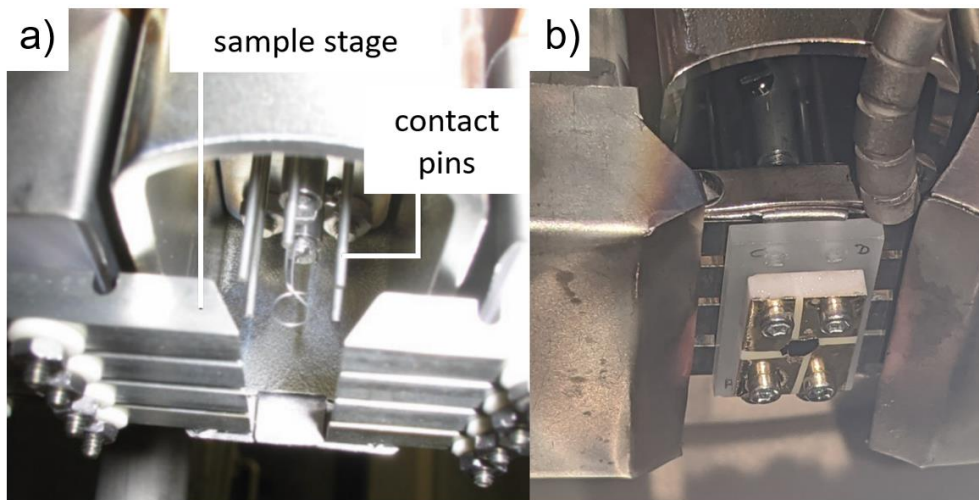


Figure 5.10 Photographs of the sample stage used for transport experiments. a) Sample stage without sample holder, showing the contact pin geometry. Every pin is mounted via a spring to account for thermal extension of the stage and to avoid contact losses upon temperature changes. The segments of the dovetail-negative are electrically isolated from the rest of the chamber. b) Sample stage with mounted sample holder.

Cooling is done via a liquid nitrogen reservoir thermally connected to (but electrically isolated from) the sample stage. Since active heating was not used, temperatures between the minimum temperature (equilibrium with filled LN<sub>2</sub>-reservoir) and room temperature were achieved by letting the LN<sub>2</sub> evaporate so that the stage – and therefore the sample holder and sample – slowly warms up to room temperature. Two k-type thermocouples at the stage were used to measure the temperature. Temperature values measured in such a way are not identical with the actual temperature at the very sample. This mismatch was accounted for by employing a calibration measurement, where a third thermocouple was directly mounted on a Na<sub>2</sub>IrO<sub>3</sub> sample, yielding the sample temperatures relative to the stage temperatures.

Measuring the resistance in dependence of the temperature for uncleaved crystals and calibrating them showed good agreement of the qualitative behaviour for the top-side of the sample when compared to measurements done with a PPMS in the group of Philipp Gegenwart, Augsburg University. For the bottom side of the sample, the calibration overestimated the temperature by 25 K at the low temperature equilibrium and the calibration was adjusted accordingly. The 25 K difference is plausible, since the samples top facet is directly exposed to thermal radiation, while the bottom crystal side is directly attached to the cooled sample holder.

For transport measurements, the first step is the recording of reference data by probing the uncleaved sample. For this, one voltage-sweep per minute was done from -1 V to 1 V. Every sweep took 20 seconds, followed by 40 seconds of rest to allow potentially induced heat from Joule heating to dissipate. Simultaneous temperature measurements allowed to correlate

temperature, applied voltage and measured current. After cleaving, the transport measurements were performed again using the same procedure. Finally, to quantify the impact of degeneration of the freshly cleaved surface in air, the chamber was vented to 1 bar of ambient air and re-evacuated after a chosen time-interval. This is followed again by transport measurements using the same procedure as before. An overview over the procedure is found in Figure 5.11.

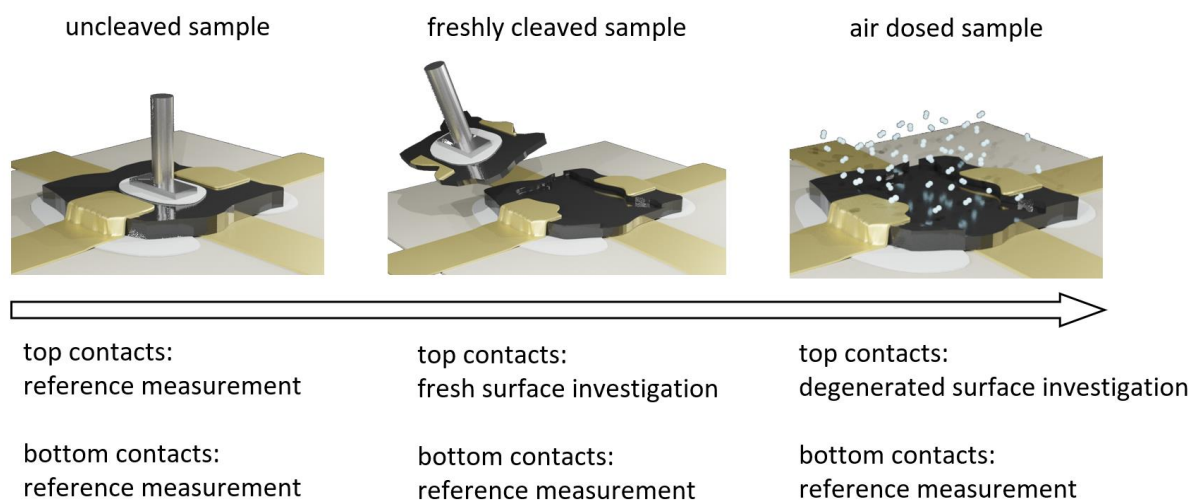


Figure 5.11 Overview over the general procedure for the transport measurements on  $\text{Na}_2\text{IrO}_3$ . Before cleaving, both, the top channel (top contacts) as well as the bottom channel (bottom contacts) are used to get reference data. After cleaving in UHV, both channels are investigated again, where the bottom channel provides a reference to check for the occurrence of cleaving-related effects. The top channel addresses the freshly cleaved surface. Finally, the sample is exposed to air for several hours to degenerate the fresh surface and investigate the impact of this degeneration on the surface conductance.

Voltage application and simultaneous measurement of the resulting current was done using a Keithley source-meter 2606B. The signal to noise ratio was minimized by integrating over 5 power grid cycles (0.1 s per data point). The precision of the current measurements was  $< 10$  nA for the source-meter.

## 5.7 Applicable Transport Phenomena

In the following, an introduction to the transport phenomena that are considerable for the discussion of the experimental transport results on  $\text{Na}_2\text{IrO}_3$  is given. This introduction exceeds the reported  $\text{Na}_2\text{IrO}_3$  transport characteristics to account for new results gained in the scope of the work on this thesis.

### 5.7.1 Metallic Conduction

Metals have no bandgap at the Fermi energy and their valence electrons are delocalized. The valence electrons with energy close to the Fermi level contribute to electrical conductivity, as unoccupied states are available at close energies. These electrons can be treated as a Fermi-gas and their occupation of available states is described via the Fermi-Dirac distribution, that is influenced by temperature, local variations of the charge density, external electric fields and scattering processes. Using the Boltzmann-equation, one can derive an expression for metallic conductivity:

$$\sigma = \frac{ne^2}{m^*} \tau(E_F) \quad , \quad 5.12$$

with the effective electron mass  $m^*$ , the charge carrier density  $n$  in the vicinity of the Fermi level and the scattering relaxation time  $\tau$ . Since only  $\tau$  has a significant temperature dependence, scattering determines the  $\sigma(T)$  behavior in metals. The relevant scattering mechanisms are defect and phonon scattering. Defects introduce a local alteration of the potential that is not temperature dependent. Hence, defect scattering is temperature independent, i.e.  $\tau_D = \text{const.}$  Electrons scatter at such defects elastically, i.e.  $\vec{k} \rightarrow \vec{k}'$  with  $E(\vec{k}) = E(\vec{k}')$ . In contrast, phonon scattering is an inelastic process, and its temperature dependence is given by the Bloch-Grüneisen law, yielding  $\tau_{ph}^{-1} \propto T^5$  for low temperatures and  $\tau_{ph}^{-1} \propto T$  for high temperatures. The Matthiesen rule states that phonon and defect scattering are independent from each other. Hence, the resistivities emerging from the two scattering types can be summed:

$$\rho = \frac{m}{ne^2\tau} = \rho_D + \rho_{ph} = \frac{m}{ne^2\tau_D} + \frac{m}{ne^2\tau_{ph}(T)} \quad . \quad 5.13$$

In metals close above 0 K, the resistivity increases with  $\sim T^5$  until it reaches the linear phonon scattering regime, as depicted in Figure 5.12 a).

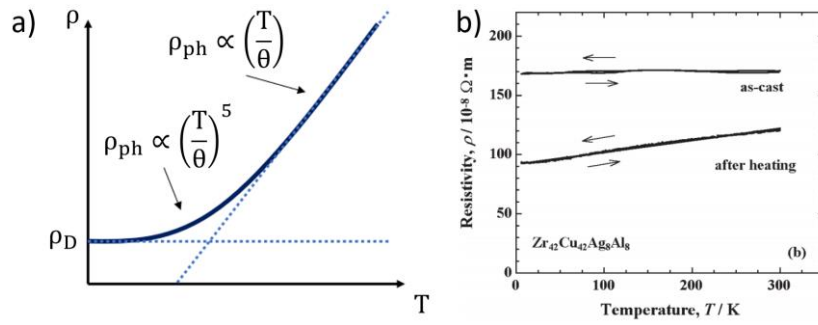


Figure 5.12 Temperature dependence of metallic conductivity. a) Schematic course of the temperature dependence according to the occurring scattering effects and the Matthiessen rule. At low temperatures, phonons are frozen out and the constant resistance due to defect scattering determines the  $\rho(T)$ -curve. With rising temperature, normal-electron-phonon scattering occurs yielding a  $\rho \propto T^5$  behavior. Above the Debye temperature  $\theta$ , Umklapp-electron-phonon scattering becomes increasingly dominant, yielding a linear  $\rho(T)$  curve. b) Resistivity versus temperature for  $\text{Zr}_{42}\text{Cu}_{42}\text{Ag}_8\text{Al}_8$ . The upper curve was taken at a freshly prepared amorphous sample, showing a nearly constant temperature dependence, as the scattering is dominated by defect scattering. The lower curve was taken after heating the sample to 873K and cooling it down again. The amorphous material crystallizes in the process, reducing the defect density significantly. Consequently, the linear electron-phonon-scattering  $\rho(T)$ -characteristic becomes apparent. From [89].

Typical ratios between high and low temperature resistivities are  $\rho(300 \text{ K})/\rho(4.2 \text{ K}) \approx 10^3$  [90]. However, metals with particularly high defect densities – and therefore strong defect scattering – like highly alloyed materials show smaller ratios. The extreme on this defect spectrum are amorphous metals, where the potential landscape shows no periodicity at all, which could effectively be treated as a saturation with defects. An exemplarily dataset is shown in Figure 5.12 b). Here, defect scattering is the dominant source of resistivity which can lead to ratios of  $\rho(300 \text{ K})/\rho(4.2 \text{ K}) \approx 1$  [89], [90]. The corresponding  $\rho(T)$ -curves appear to be temperature independent, as phonon scattering is negligible.

### 5.7.2 Electrical Transport in Semiconductors and Mott Insulators

Semiconducting (SC) solids and Mott insulators (MI) exhibit an energy gap  $E_g > 0 \text{ eV}$ . In the case of Mott insulators, this gap is referred to as the Mott gap. In SC's, the band gap separates the valence band (VB) and the conduction band (CB), while in MI's the Mott gap separates the lower (LHB) and the upper Hubbard band (UHB). Even though the VB/CB and LHB/UHB are not fundamentally the same (e.g. the VB and CB correspond to different orbitals, while LHB and UHB correspond to the same orbital), the conduction mechanism emerging in SC's and MI's is similar if the Mott gap size is comparable to semiconductor band gap sizes [91]. The thermal excitation ansatz used for SC's is also applicable for MI's like  $\text{Na}_2\text{IrO}_3$ . In the following,

when MI's are mentioned it is presumed that the Mott gap is comparable to common semiconductor band gaps.

### 5.7.2.1 Intrinsic and Lightly Doped Semiconductors and Mott Insulators

In the intrinsic case, i.e. the absence of doping, the density of thermally excited electrons determines the overall conductivity. These excited electrons can be modelled as a free electron gas. Hence, the conductivity of the excited electrons can be described by using equation 5.12 and adapting the parameters for the semiconducting or Mott insulating case.

The number of charge carriers that are thermally excited into the CB/UHB (electrons) and VB/LHB (holes) is characterized by the Fermi-Dirac distribution. From the number of excited charge carriers, the temperature dependent conductance for an intrinsic SC as well as an MI can be approximated by [90]–[92]

$$\sigma \approx \sigma_0 e^{\frac{-E_g}{2k_B T}}, \quad 5.14$$

where  $\sigma_0$  depends on the effective masses of the involved electrons and holes as well as on the temperature with  $\sigma_0 \propto T^{3/2}$  [90]–[92]. Since the exponential term in  $\sigma$  dominates the temperature dependence,  $\sigma_0$  is often approximated as temperature independent. In contrast to metallic systems, the overall carrier density is lower by several orders of magnitude and screening of charged defects is less efficient.

Light doping introduces defects to the system that act as acceptors and/or donators. Electron scattering at charged defects can be modelled by Rutherford scattering, yielding a temperature dependence of the relaxation time of  $\tau_D \propto T^{3/2}$  [90], [92]. In metals, the carrier velocity approximately equals the Fermi velocity and is temperature independent. For excited carriers, the carrier velocity is determined by the equations of states of the kinetic and the ideal gas, yielding  $v \propto \sqrt{T}$ . Incorporating this results in  $\tau_{ph} \propto T^{-3/2}$  for  $T \gg \theta_D$  [90], [92], where  $\theta_D$  denotes the Debye temperature. According to the Matthiessen rule (equation 5.13), defect and phonon scattering are independent from each other. Scattering has only a minor effect on the  $\sigma$  vs  $T$  dependence, that is dominated by the thermal excitation of charge carries between different band and/or defect states, and is often neglected [90], [92].

### 5.7.2.2 Band Tailing, Transport Heavily Doped Semiconductors and Anderson Localization

When the spatial distance between defects in a semiconductor is sufficiently small, the overlap of the defect wave functions becomes considerable, and energy splitting of the defect states occurs to lift the degeneracy, as depicted in Figure 5.13 a) [93].

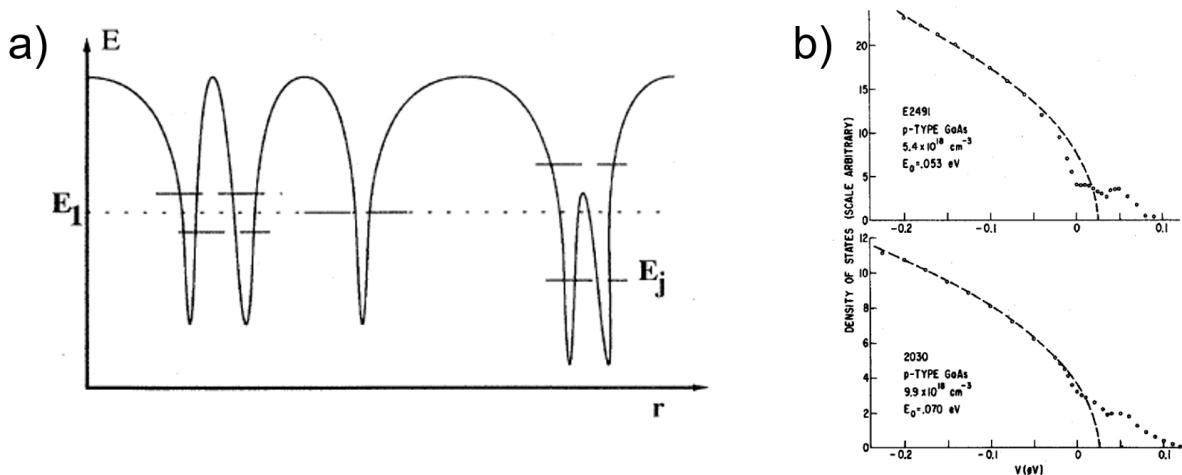


Figure 5.13 Energy shifting due to heavy doping and band-tailing. a) Schematic depiction of the potential (solid curve) and energy levels (dashed lines) for a system of attractive impurities [93], [94]. b) Band-tailing in p-doped GaAs with doping concentrations  $5.4 \cdot 10^{18} \text{ cm}^{-3}$  (top) and  $9.9 \cdot 10^{18} \text{ cm}^{-3}$  (bottom) showing a broad acceptor DOS (dots) merging into the valence band (dashed line) [93], [94].

If the defects are randomly distributed, the defect density varies locally, resulting in a broad energy spectrum of the defect states. The in-gap defect density of states peak is energetically broadened accordingly. Since shallow dopant states are located energetically close to either the valence or the conduction band of the host material, sufficiently low inter-defect distances cause a broadening of the defect DOS large enough to close the gap between the defect states and the valence/conduction band. The system is then described as heavily doped (also: degenerated) [93]. It was found that the energetic broadening of such a defect DOS does not occur symmetrically. Instead, the DOS forms a “tail” at the according band, and the situation is referred to as “band-tailing”, Figure 5.13 b), [93], [94]. When the Fermi level  $E_F$  lies within the defect DOS, band tailing can push  $E_F$  into the respective semiconductor band, resulting in metallicity of the system [93]–[96].

States “deep” in the band tail correspond to spatial regions with particularly high defect density, resulting in a large energy shift of the defect states. Charge carriers within such deep states are localized [93], [97], [98]. The energetically closer the state in the band tail to the semiconductor band, the weaker the localization of the charge carriers, as the probability to find spatially close states with similar or lower energy rises. This connection is valid for randomly distributed states [93], [96], [99], [100], i.e. if defect states were spatially ordered, the



related wavefunction overlap would be similar for each defect state and no deep potential wells occur.

The connection between disorder and localization was first theoretically described by P. W. Anderson, and disorder induced localization is commonly referred to as Anderson localization [93], [96], [99], [100]. In 1D and 2D systems, any disorder immediately results in Anderson localization, where in 3D systems small randomness can be treated as perturbation without immediately causing localization [93], [97], [98]. The transport mechanism mediated by such localized states is (variable range) hopping.

### 5.7.3 Hopping Conduction and Variable Range Hopping

The microscopic picture behind the transport of localized charge carriers is a hopping between localized states. The general picture is as follows: electrons occupy energy levels within randomly distributed deep potentials, so that any hopping site is separated from other hopping sites by potential barriers, preventing electrons to move freely like in metals, even though the energetic and spatial differences of the sites may be small. The situation is schematically depicted in Figure 5.14.

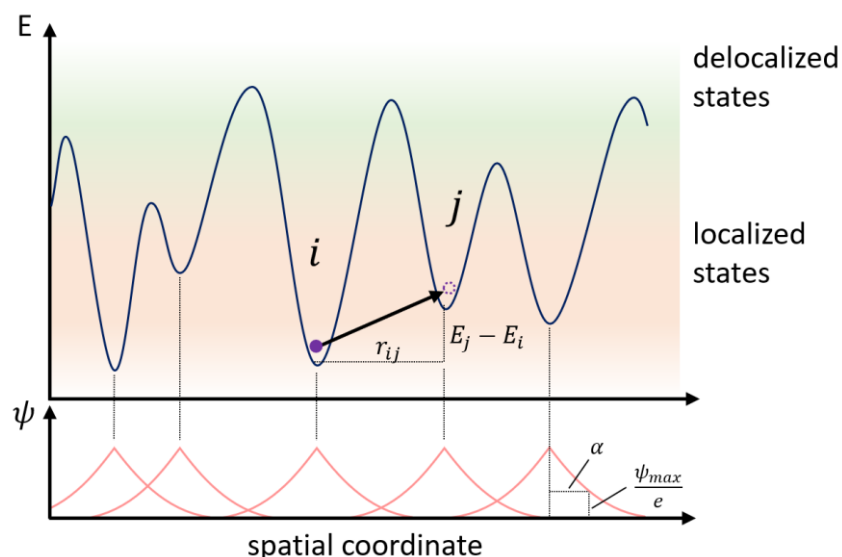


Figure 5.14 Schematic situation for electron hopping conductivity. Top: when the Fermi level lies in the localized state region, electrons need to overcome a potential barrier to get to a different unoccupied state and therefore move in real space. For sufficiently deep potential wells, the dominant mechanism for such changes of occupied site is the electron tunnelling through the respective potential barrier. Bottom: sketch of s-electron wavefunctions corresponding to the localized states to illustrate their overlap and the localization length  $\alpha$ . Adapted from [93], [98], [101]

For temperatures too low to excite the respective electron over the potential barrier (i.e. to lift the electron into a delocalized state), the quantum mechanical electron tunnelling is required for a site change (hopping) of electrons. Electron hopping from state  $i$  to state  $j$  (see Figure 5.14) depends on the spatial separation  $r_{ij}$  and the energetic separation  $\Delta E_{ij} = E_j - E_i$  of the states, leading to the inter-site resistance  $R_{ij}$  proportionality [98], [102]:

$$R_{ij} \propto e^{\left(\frac{r_{ij}}{\alpha} + \frac{\Delta E}{k_B T}\right)} . \quad 5.15$$

For high temperatures, i.e.  $\Delta E/k_B T \ll r_{ij}/\alpha$ , the inter-site resistance governed by the spatial separation and therefore hopping occurs between nearest neighbours. To relate the local inter-site resistance to a macroscopic resistance throughout a sample, a percolation ansatz is used. For this a percolation threshold is defined using the exponent from equation 5.15 to  $x_c = r_c/\alpha + \Delta E_c/k_B T$  [51],[105]–[107]. Hopping site pairs that fulfil  $R_{ij} \propto \exp(r_{ij}/\alpha + \Delta E/k_B T) < \exp(x_c)$  are categorized as “bonded”, all other site pairs as “unbonded”. In the percolation picture, only chains of bonded sites contribute to the macroscopic electric conductance. This is schematically depicted in Figure 5.15, where two paths are available for conduction but only the top path fulfils the percolation requirements.

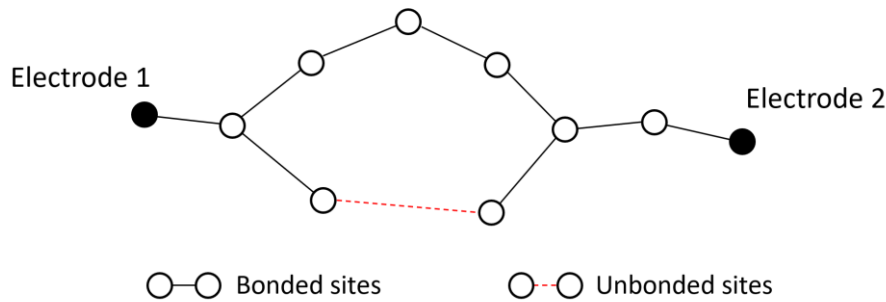


Figure 5.15 Scheme for the percolation model underlying nearest neighbour hopping conductance. Electric current between electrodes 1 and 2 is realized by electron hopping to the nearest neighbours if the two involved hopping sites are bonded in the percolation sense. Here, for the top path, all site-pairs are bonded, allowing for hopping conductance. For the bottom path, an unbonded site pair inhibits conductance. Upon raising the percolation limit, this unbonded pair can transform into a bonded pair, allowing for conductance through the bottom path. Adapted from [106].

For the macroscopic resistance of a material to change, closed (bonded) paths need to emerge or to get disconnected. In a solid, the spatial position of the hopping sites is fixed. Considering a site pair for which  $R(T) > \exp(x_c)$  but  $R(T + \Delta T) < \exp(x_c)$  holds, a finite raise in temperature transitions the site pair from unbonded to bonded. For site pairs that are infinitesimally close to the percolation threshold, an infinitesimal temperature raise is sufficient. Considering the bottom path in Figure 5.15, this can lead to the closing of a path and therefore to a reduction

of the overall macroscopic resistance. With this, the macroscopic nearest neighbour hopping resistance is described by

$$R(T) = R_0 e^{\left(\frac{r_c}{\alpha} + \frac{\mu}{k_B T}\right)}, \quad 5.16$$

with the activation energy  $\mu$ , representing the average energy difference between hopping site pairs close to the percolation threshold [107], [108].

The lower the temperature, the higher the chance to find hopping site pairs where the energetic difference  $\Delta E$  is too large to consistently get thermally overcome. In such a situation, hopping beyond nearest neighbors can be favorable, depending on the ratio between  $r_{ij}/\alpha$  and  $\Delta E/k_B T$  [102]. This type of conduction is referred to as variable range hopping (VRH). The VRH model is based on the physical picture shown in Figure 5.16. The ansatz is to translate the inter-site resistances  $R_{ij}$  into a macroscopic VRH resistance  $R$  is to reduce the  $R_{ij}$  network into a network of identical resistors, so that the network-character itself can be modelled by a single pre-factor.

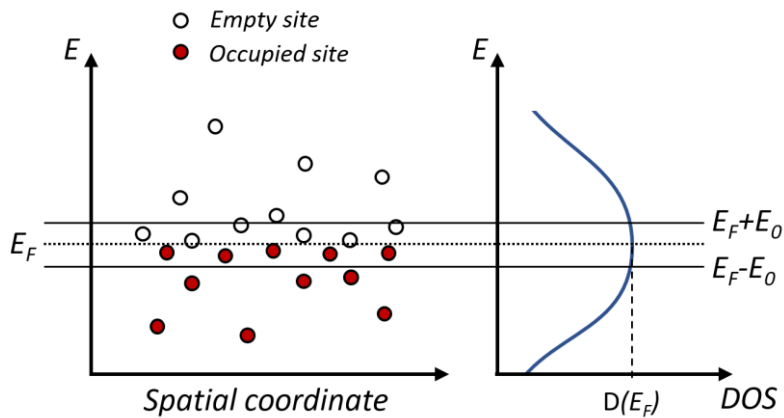


Figure 5.16 Physical Picture underlying variable range hopping conductance. Defect states are randomly distributed in space, where the energy of the defect states lies in the vicinity of the Fermi level (left). The defect states form a defect-band (right). Electron transport is mediated by states within a narrow interval  $[E_F - E_0, E_F + E_0]$  around the Fermi level. With this interval, the defect band is approximated to be constant vs the energy, i.e.  $D(E) = D(E_F)$ . Adapted from [106].

Since the thermal activation of charge carriers at low temperatures is not sufficient to address empty states far away from the Fermi level  $E_F$ , hopping takes place in a narrow energy interval  $[E_F - E_0, E_F + E_0]$  around the Fermi level. In such a narrow interval, the density of states can be approximated to be constant, i.e.  $D(E) \approx D(E_F)$ . The number of states  $n_V$  is then constant within a given volume  $V \propto r^d$  with the dimensionality  $d$ . Hence, the spatial distance  $r$  is proportional to  $E_0$  and the density of states via  $r \propto 1/(2 \cdot E_0 \cdot D(E_F))^{1/d}$ . With this, the local

resistance  $R_{ij}$  is translated into an average resistance  $R$  by identifying  $E_0$  as the average required activation energy, i.e.  $\langle \Delta E \rangle = E_0$  [107], [108] and the average hopping distance as  $\langle r_{ij} \rangle = (2 \cdot E_0 \cdot D(E_F))^{-\frac{1}{d}}$ . From equation 5.15, one gets [102]:

$$R \propto e^{\left( \frac{1}{\alpha(2 \cdot E_0 \cdot D(E_F))^{-\frac{1}{d}} + \frac{E_0}{k_B T}} \right)} \quad 5.17$$

The physical picture behind the exponent in equation 5.17 is that the spatial overlap of the electron wavefunctions and the average energy separation compete, leading to a resistance minimum when both terms in the exponent are equal. From this, one obtains:

$$E_0 = \frac{(k_B T)^{d/d+1}}{[2 \cdot D(E_F) \alpha^d]^{1/d+1}} \propto T^{\frac{d}{d+1}} \quad 5.18$$

Plugging equation 5.18 into equation 5.17 yields

$$R = R_0 e^{\left( \left( \frac{T_0}{T} \right)^{1/d+1} \right)} \quad 5.19$$

This is the temperature and dimensionality dependent low field variable range hopping resistance.  $T_0$  is a system dependent constant:  $T_0 = \beta/k_B D(E_F) \alpha^d$  with the numerical constant  $\beta = 21.2 \pm 1.2$  [109] for 3D-VRH and  $\beta = 13.8$  [110] for 2D-VRH.

From equation 5.19 it becomes clear that the resistance of VRH mediated transport in 2D and 3D shows the proportionalities:

$$\begin{aligned} \ln(R) &\propto \frac{1}{T^{1/3}}, & 2D \\ \ln(R) &\propto \frac{1}{T^{1/4}}, & 3D \end{aligned} \quad 5.20$$

#### 5.7.4 Effect of Electron-Electron Correlation on Variable Range Hopping

To account for inter-site electron correlation in the framework of VRH, the energy difference between two given hopping sites  $i$  and  $j$  is modified by a Coulomb term [111], [112], i.e.

$$\Delta E = E_j - E_i - \frac{e^2}{\kappa \Gamma_{ij}}, \quad 5.21$$

with the absolute dielectric constant  $\kappa$  of the material. In the ground state, all sites below  $E_F$  are occupied, all sites above  $E_F$  are unoccupied. Using the derived  $\langle r_{ij} \rangle$  from uncorrelated VRH, one obtains  $\Delta E = E_j - E_i - e^2/\kappa r_{ij} = E_j - E_i - e^2\kappa(2 \cdot E_0 \cdot D(E_F))^{1/d} > 0$ . Considering now a site pair  $ij$  infinitesimally close to  $E_F$ , the condition  $\Delta E > 0$  enforces  $e^2\kappa(2 \cdot E_0 \cdot D(E_F))^{1/d} = 0$  and therefore  $D(E_F) = 0$ . Hence, a pseudo gap emerges that is referred to as the Coulomb gap. Hopping that includes inter-site correlation, resulting in the emergence of a Coulomb gap, is named after their pioneers to Efros-Shklovskii Hopping (ESH). Since the macroscopic transport characteristics are mostly influenced by the density of states close to  $E_F$ , the characteristics of the Coulomb gap are important. From the expression for  $\Delta E$ , the condition  $r_{ij} \geq e^2/\kappa\Delta E_{ji}$  is derived, with  $\Delta E_{ji} = E_j - E_i$ , leading to the expression for the spatial hopping site concentration  $n(\Delta E_{ji}) \leq \kappa^d \Delta E_{ji}^d / e^{2d}$ , that in turn leads to the density of states via  $D(\Delta E_{ji}) = dn/d\Delta E_{ji} \leq c \cdot \kappa^d \Delta E_{ji}^{d-1} / e^{2d}$ , with the numerical coefficient  $c$  in the order of unity [111]. The density of states vanishes with  $E_0 \rightarrow 0$  at least as fast as  $E_0^2$  and a quicker decrease of  $D$  would mean an average hopping site separation greater than  $e^2/\kappa E_0$ , leading to a weaker Coulomb interaction. It is argued that such a weak interaction is not sufficient for the emergence of a Coulomb gap [111], resulting in

$$D(\Delta E_{ji}) = c \cdot \frac{\kappa^d \Delta E_{ji}^{d-1}}{e^{2d}} . \quad 5.22$$

Hence, the Coulomb gap is parabolic for 3D-systems and linear for 2D-systems. Using this expression for the density of states in the derivations for low and high electric field VRH resistance yields

$$R = R_0 e^{\left(\frac{T_{ES}}{T}\right)^{1/2}} \rightarrow \ln(R) \propto \frac{1}{T^{1/2}} , \quad 5.23$$

with  $T_{ES} = \beta e^2/\kappa\alpha$  and a factor  $\beta$  [113].

### 5.7.5 Transport Properties of Topologically Protected Boundary States

This chapter is based on the reviews [6], [8], [55], [114]. The specification of the in-gap states at the intersection between two materials with different topological invariants is not arbitrary, as time reversal symmetry enforces a linear dispersion at the crossing points of the valence and conduction bands (Figure 3.4) as well as spin-momentum locking (see chapter 3.2) [8]. For two

dimensional insulators, the conductivity of each edge channel is similar to the conductivity in one-dimensional wires where the mean free path of the electrons is larger than the wire length. The conductance is quantized, ballistic and independent from temperature and the physical length of the edge [8]. Backscattering is forbidden, since a change of the momentum  $\vec{k} \rightarrow -\vec{k}$  would force the electron spin to flip in the scattering process, which is prohibited if spin-conservation is enforced. Magnetic impurities make such a scattering mechanism available and therefore result in possible backscattering. Localization effects due to disorder do not occur, rendering the edge channel to be robust against any perturbation except for mentioned magnetic impurities.

For 3D-materials, the situation is more complicated and until 2007 it was not clear if 3D-topological insulators could exist [115]–[117]. Again, both time-reversal symmetry and strong spin-orbit coupling are required. However, in 3D the spin-orbit coupling must mix all components of the spin and it is not possible to obtain a 3D-TI from separate spin up and spin down electrons as in the 2D case [55]. Even though this complicates the understanding of the physical background, especially for the determination of topological invariants, the consequences in terms of the bulk boundary correspondence are rather straight forward. Again, conductive states are forced at the boundary between a topologically trivial and a non-trivial material. The in-gap states still have a linear dispersion at the band crossing, manifesting as a Dirac cone that is protected from disorder. A spin-momentum dependence and forbidden backscattering are also apparent due to time reversal symmetry, resulting in metallic surfaces with unconventional scattering properties. In Figure 5.17, all these properties are shown on exemplary experimental data [118], [119].

To experimentally show the absence of backscattering, STM/STS measurements can be used, since the local density of states shows spatial fluctuations depending on the scattering of the electrons within the surface states. Such examinations are referred to as quasiparticle interference (QPI) investigations. To correlate found QPI patterns with the spin-texture of the material, spin-resolved ARPES investigations are performed. With the ARPES results, the Fourier transform of the corresponding QPI pattern is simulated by using the spin and momentum dependent scattering probabilities as parameters [8], [119]. If direct backscattering is found to have a probability of zero, a strong indicator for a topologically protected state is found. In summary, topologically protected surface states of 3D-TI's are robust and metallic, where the quantitative conductance is prone to scattering effects. This scattering is spin-dependent with forbidden backscattering, resulting in characteristic quasiparticle interference patterns that have the same symmetry as the Brillouin-zone.

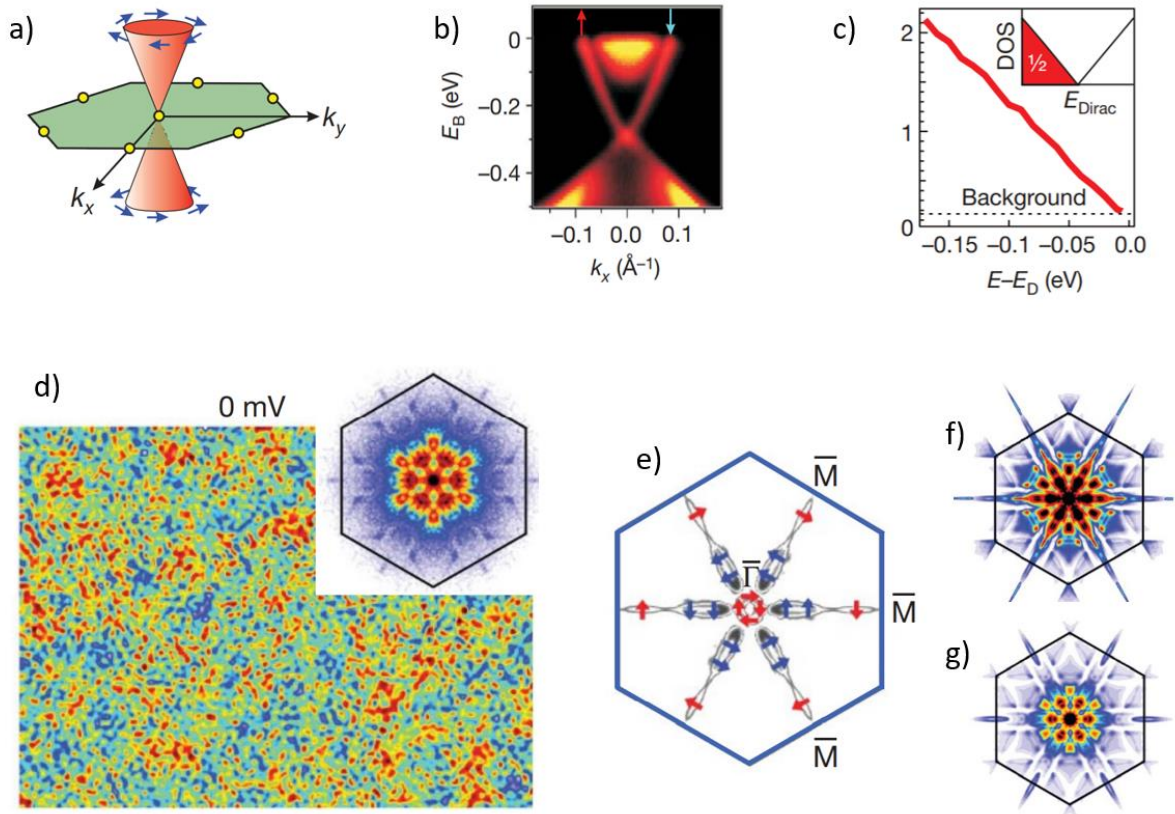


Figure 5.17 Exemplary experimental ARPES and STM data on 3D topological insulators. a)-c): Spin resolved ARPES investigation on  $\text{Bi}_2\text{Se}_3$  adapted from [118] d)-g) STM and spin resolved ARPES on  $\text{Bi}_{0.92}\text{Sb}_{0.08}$  adapted from [119] a) Scheme of the band gap closing Dirac cone with spin texture as suggested by spin-ARPES measurements. Dirac cone attributed to the topologically protected surface states as measured by means of ARPES. c) Linear density of states extracted from crystal momentum integrated ARPES data. d) Quasiparticle interference (QPI) at the Fermi level observed by STS at 4 K. The pattern is not commensurate with the surface reconstruction and single defects are not easily distinguishable. The inset showing the Fourier transform of the QPI pattern exhibits a clear structure even though the QPI being incommensurate with respect to the surface, highlighting that disorder does not impact the surface state. e) Spin texture as measured by spin resolved ARPES. f) Calculated QPI-Fourier transform with allowed backscattering based on spin resolved ARPES data. g) Calculated QPI-Fourier transform with prohibited backscattering based on spin resolved ARPES data. It is evident, that the backscattering-free calculation fits better to the measured data, suggesting the absence of direct backscattering. Spin-momentum dependent scattering is still apparent.



## 6 Scanning Tunnelling Microscopy and Spectroscopy on the Freshly Cleaved Na<sub>2</sub>IrO<sub>3</sub> Surface

In the following, the results from STM/STS investigations on the freshly cleaved Na<sub>2</sub>IrO<sub>3</sub> surface are presented, starting with structural characterizations and an examination of the long-time stability. Afterwards, electronic properties of the Na<sub>2</sub>IrO<sub>3</sub> surface measured with STM/STS are investigated (chapters 6.2-6.4). This is followed by a presentation of successful STM measurements on Na<sub>2</sub>IrO<sub>3</sub> at 8 K using optically excited charge carriers (chapter 6.5).

### 6.1 The Chemical Stability on the Na<sub>2</sub>IrO<sub>3</sub> Surface in UHV and In-Situ Modifications of the STM Tip

In a previous work, it was shown that Na<sub>2</sub>IrO<sub>3</sub> degenerates when being simultaneously exposed to H<sub>2</sub>O and CO<sub>2</sub> (see chapter 3.1), where the concentration in ambient air is sufficient to cause significant changes in measured x-ray spectra within hours [65]. The approach to avoid such degeneration in the experimental work for this thesis is to cleave and investigate all samples in UHV. It was further reported that sodium effuses from the bulk to freshly cleaved surfaces when the sample is in air, forming Na-clusters that grow continuously over time, reaching sizes of ~12 μm<sup>2</sup> within 50 hours (chapter 3.1, [65]). The effusion mechanism is not clear and might as well occur under UHV conditions. To check if changes of the freshly cleaved Na<sub>2</sub>IrO<sub>3</sub> surface due to degeneration or Na effusion occur in the used UHV setup, a long-time STM measurement was done at 300 K for 56 hours, where the same area was scanned every 8 hours. The results are shown in Figure 6.1.

The surface depicted in the topographies in Figure 6.1 is (1x1)-reconstructed. Once cleaved, all Na<sub>2</sub>IrO<sub>3</sub> surfaces examined by means of STM at 8 K, 80 K and 300 K stayed clean and stable under UHV conditions (< 10<sup>-9</sup> mbar). No degeneration of the surface and no growth of clusters due to effusion of sodium from the bulk to the surface is observed over time. Hence, the approach to use freshly cleaved Na<sub>2</sub>IrO<sub>3</sub> surfaces in UHV ensures that all data collected in this work emerge from properties of Na<sub>2</sub>IrO<sub>3</sub> surface and are not artifacts due to degeneration or sodium effusion.

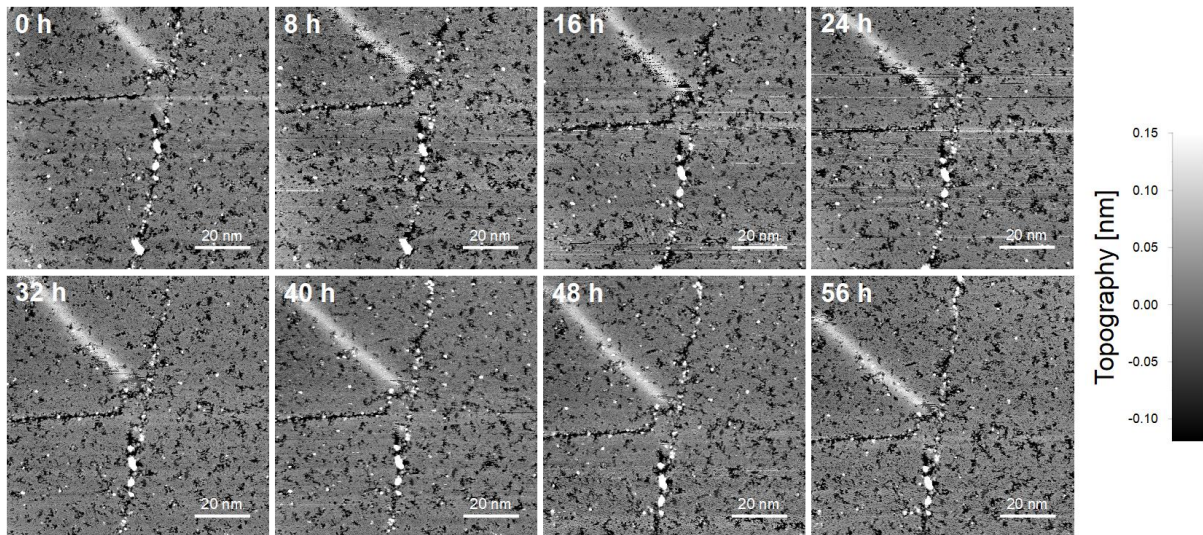


Figure 6.1 Long-time STM constant current topography measurement at 300 K using a setpoint of -1.5 V and 100 pA. For 56 hours, a constant current topography was taken every 8 hours at the same position on the freshly cleaved  $\text{Na}_2\text{IrO}_3$  surface. Here, the surface shows the (1x1)-reconstruction. No degeneration and no growth of sodium clusters is observed over time.

Regarding the known two surface reconstructions, the findings from previous works were confirmed in the scope of this thesis and will therefore not be discussed here in detail. In agreement with these former STM investigations [18], [29], only sodium terminated, (1x1)-reconstructed surfaces appear to be well ordered for large areas, while the  $(\sqrt{3}\times\sqrt{3})R30^\circ$ -reconstruction shows particularly high defect densities and merely small well-ordered patches. The presentation of data in chapter 6 will focus on the (1x1)-reconstructed surface and it will be discussed if the gained insights can be also applied to the  $(\sqrt{3}\times\sqrt{3})R30^\circ$ -reconstruction.

The defects found on the surface depicted in Figure 6.1 are detailed in Figure 6.2, showing zoomed-in STM topographies.

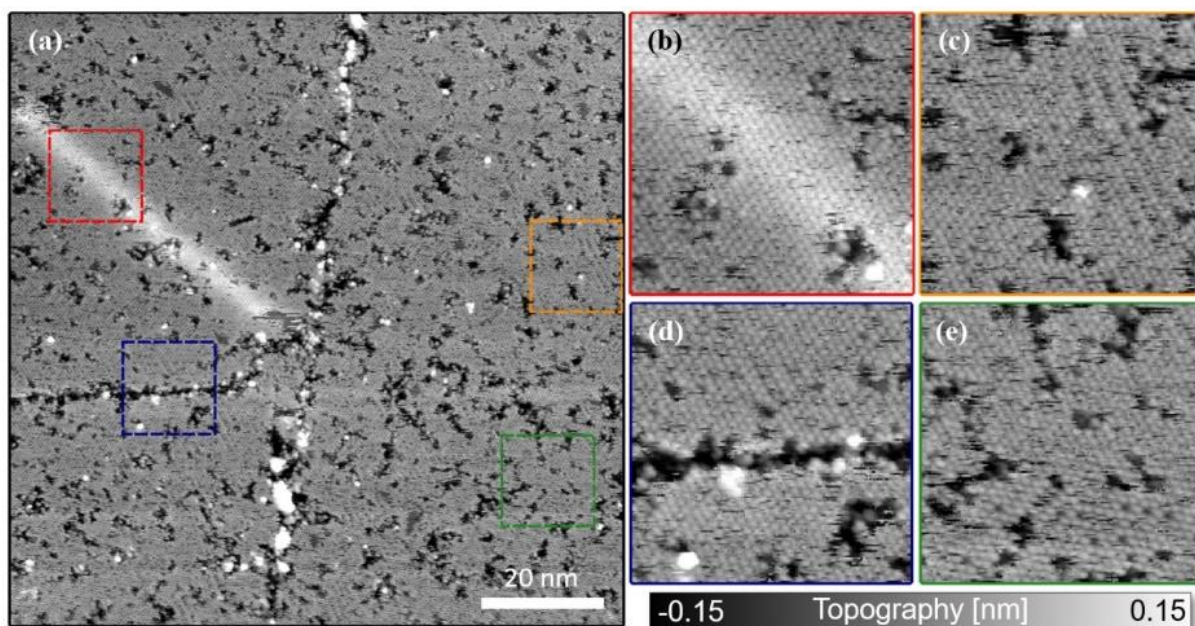


Figure 6.2 High defect density observed on  $\text{Na}_2\text{IrO}_3$  surfaces. (a) 100 nm x 100 nm constant current topographic map showing various defect structures on the (1x1)-reconstructed  $\text{Na}_2\text{IrO}_3$  surface, recorded using a setpoint of -1.5 V and 100 pA at room temperature. The dashed boxes mark the positions of the zoom-ins depicted in (b)-(e). (b) Ridge-like defect with a topographic height of approximately 100 pm. (c) "Stripy" pattern superimposed to the regular (1x1)-reconstructed surface, bordered by various defects. The pattern does not extend over any defects. (d) Crack in the topmost crystal layer (here:  $\text{Na}_3$  layer). Such cracks extend over several hundred nanometre and locally exhibit small sodium aggregations (white contrast). (e) Different surface defects, ranging from vacancies due to missing single sodium atoms to large defect aggregations.

Figure 6.2 shows a high defect density on the cleaved  $\text{Na}_2\text{IrO}_3$  surface from defects of various types. These defect types cover ridge-like defects with a topographic height of  $\sim 100$  pm (Figure 6.2 b)), stripy patterns superimposed on the regular (1x1)-reconstruction (Figure 6.2 c)), extended cracks on the surface (Figure 6.2 d)), and single vacancies as well as their aggregation into larger vacancy structures (Figure 6.2 e)). The distance between defects range from a few to some tens of nanometres. Among all performed STM investigations on multiple  $\text{Na}_2\text{IrO}_3$  samples done in this thesis, a high defect density was always present and free areas were the exception. Occasionally defects are arranged in unexpected structures on the surface. Examples are given in Figure 6.3.

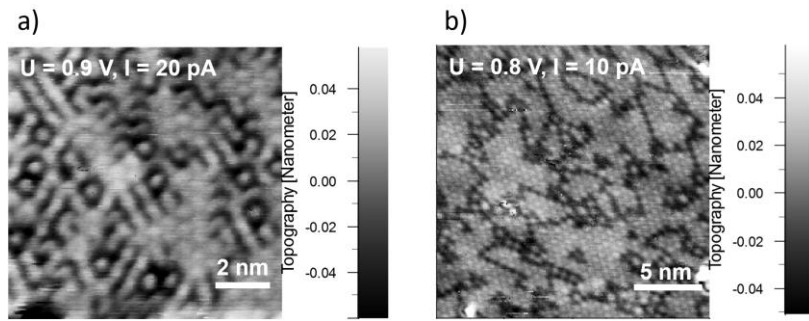


Figure 6.3 Two examples of unusual defect structures on the (1x1)-reconstructed surface measured with constant current STM at 300 K. a) Surface Na atoms form linear structures connecting Na islands. Within larger vacancy aggregations, single Na atoms arrange in a way that maximizes the minimum distance to another surface Na atom. b) Vacancies aggregate in extended linear structures, separating Na islands.

Here, on the one hand, surface sodium atoms form linear structures connecting small Na-islands. Single sodium atoms arrange in the centre of larger vacancy aggregations, presumably to minimize the energy due to coulomb repulsion since Na is positively charged in  $\text{Na}_2\text{IrO}_3$  (Figure 6.3 a)). On the other hand, there are examples where it is the vacancies that form line-shaped structures, bordering islands of (1x1)-reconstructed sodium atoms (Figure 6.3 b)). Neither of the two defect structures seen in Figure 6.3 was reported in former STM works on  $\text{Na}_2\text{IrO}_3$  [18], [29].

Stable tunnelling in STM investigations on  $\text{Na}_2\text{IrO}_3$  is possible within a small measurement parameter window. Usually, bias voltages between -1.5 V and -1 V as well as voltages close to 1 V with a tunnelling current setpoint below 100 pA work well. These values vary between measurements, i.e. are dependent on the respective tip and the local sample surface. Lowering the systems temperature from 300 K to 80 K does not provide a noticeable increase of the window of stable STM parameters. STM measurements at 8 K using LHe cooling were also performed and show similar issues regarding the stability of the STM tunnel contact. However, the 8 K STM investigations require an additional supply of charge carriers for tunnelling using optical excitation, as the resistivity of  $\text{Na}_2\text{IrO}_3$  rises exponentially with decreasing temperature. Consequently, a comparison of the stability of the tunnelling contact at 8 K with the stability at 80 K or 300 K might be misleading.

Occasionally, a loss of stability of the tunnelling contact or a loss of atomic resolution occurs by chance while scanning over the sample surface. Furthermore, in some instances the stability/atomic resolution is restored upon continued scanning shortly after without intervention. Subsequently repeating the measurement on the same area then shows that the loss/regain of stability/resolution does not correlate with structures on the sample surface and that the surface itself remains unaffected. Such a behaviour can be explained by modifications



of the STM tip during the measurement. STM tip modifications cannot be observed directly, as the precise condition of the tip is not accessible in STM examinations. Re-establishing stable conditions and/or atomic resolution is the usual approach. This is done by restoring the initial state of the tip. There are three general methods to work on the STM tip in-situ: firstly, applying short voltage pulses to the sample while the tip is in tunnelling contact (1 V – 5 V for up to 0.5 ms). Secondly, movements of the STM tip in z-direction (0.2 - 0.5 nm in 50 - 100  $\mu$ s). And thirdly, bringing the tip in physical contact with a surface, either the sample itself or preferably a known metallic material, e.g. gold. The first two methods are not viable for  $\text{Na}_2\text{IrO}_3$ . Voltage pulses in close proximity to the sample surface often led to damages of the very surface, presumably due to the high electric field and the locally charged nature of the material. Such damages occur uncontrolled and usually lead to a worsening of the situation. Therefore, to employ cleaning via pulsing, the position at the surface must be changed afterwards. Controlled tip-movements rarely yield improvements. This leaves the option to bring the tip into physical contact with the sample as only method without leaving a potentially interesting area on the surface. In the employed experimental work, either voltage pulsing and changing the position or dipping the tip into a nearby gold patch (and therefore change the position macroscopically) were the practicable options. This also applies if the tip allows for stable tunnelling but yields poor resolution, as attempts to alter the tip-apex are performed with the same methods used for cleaning the tip. Using the presented tip cleaning procedures, the same results as gained by the work of Lüpke et al. [18], [29] were obtained (chapter 3.1) in the experimental work for this thesis.

Considering that for both surface reconstructions sodium atoms lie on top, i.e. closest to the STM tip during measurements, as well as the high electric field in the tunnelling junction, the most likely reason for the occurring tip modifications is the attachment and detachment of sodium to or from the STM tip. The here proposed tip-attached sodium model is depicted in Figure 6.4 on the left.

In this thesis, a major advancement for the investigation of  $\text{Na}_2\text{IrO}_3$  surfaces was achieved by investigating if modified STM tips always lead to unstable tunnelling conditions or a loss of atomic resolution on  $\text{Na}_2\text{IrO}_3$ . This was done with a “rather unusual” approach: instead of aborting a running measurement upon occurring modifications of the tip for cleaning, measurements were kept running despite tip modifications. An according dataset is depicted in Figure 6.4.

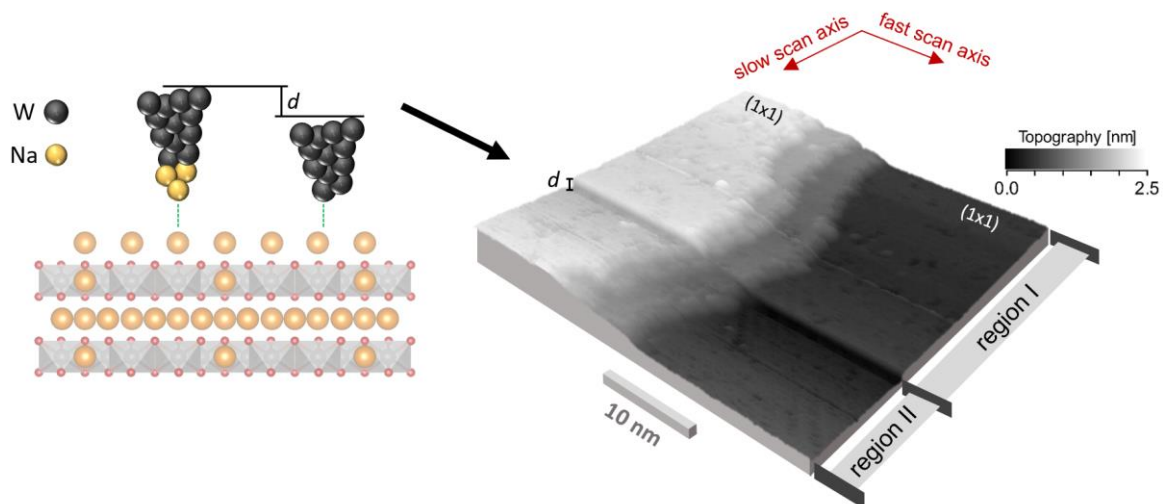


Figure 6.4 Tip modifications leading to instantaneous jumps of the recorded topographic height on the sodium iridate surface. The topography shown on the right covers three step edges separating (1x1)-reconstructed surfaces. The fast scan axis was aligned perpendicular to the step edges, the slow scan axis was aligned parallel to the step edges. Between the areas denoted as region I and region II, the topographic height instantaneously drops by  $\sim 0.43$  nm, indicating a change of the STM tip length as sketched on the left. Such a reduction in tip-length causes the STM feedback loop to approach the tip towards the surface to maintain the desired tunnelling current (here 100 pA at -1 V bias voltage). Despite the tip modification, atomic resolution is maintained.

The topography covers three surface steps, separating (1x1)-reconstructed surfaces. The areas marked as “region I” and “region II” are separated by an instantaneous change of the topographic height of  $d = 0.43 \text{ nm} \pm 0.035 \text{ nm}$ . The scanning movement of the tip is indicated in Figure 6.4. After a trace and a retrace movement along the fast scan axis is done, the tip moved one pixel in the direction of the slow scan axis. Repeating this yields the depicted topography. The instantaneous change of topographic height is proposed to be achieved by a change of the tip length. In this case, the tip height was adjusted by  $\sim 0.43$  nm towards the surface by the STM feedback loop to maintain the set tunnelling current, meaning that the tip has shortened by an according length. Such immediate changes of the topographic height are common in STM investigations on  $\text{Na}_2\text{IrO}_3$ . The tip modification in Figure 6.4 has no obvious impact on the topographic surface features, giving no hint concerning the tip shapes as well as their imaging quality for both regions.

In Figure 6.5 a) it can be better seen that both, the modified and the unmodified tip yield consistent imaging quality, depicting a zoom-in on the instantaneous jump in the topography in Figure 6.4.

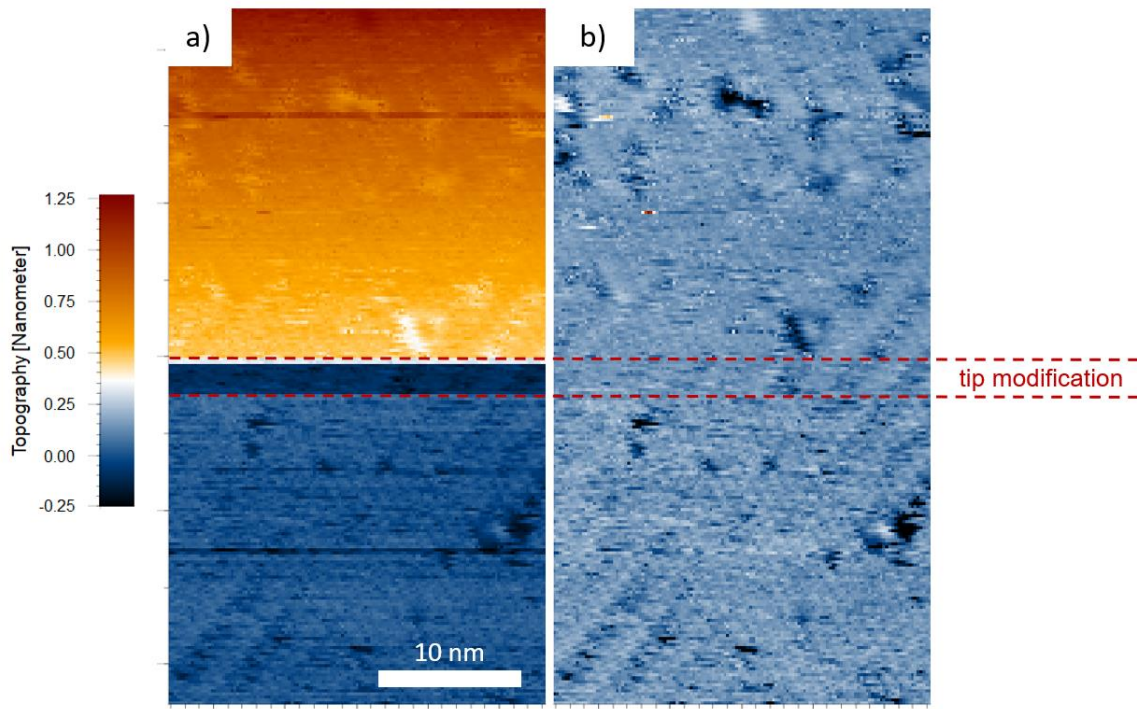


Figure 6.5 Impact of a modification of the STM tip on the observable topographic characteristics. a) STM topography measured at room temperature with a bias voltage setpoint of -1 V and a tunnelling current setpoint of 100 pA. The surface is (1x1)-reconstructed, i.e. sodium terminated. The upper part of the topography corresponds to region I, the lower part to region II. The instantaneous jump in topographic height denotes a change of tip length and therefore a change of the (sodium) structure at the tip apex. b) Same topographic data as in a), adjusted via a horizontal line offset. The atomic resolution before and after the tip modification is unchanged.

In Figure 6.5 b), the same topography is shown but adjusted via a horizontal line offset to compensate the jump in topographic height, revealing that the atomic resolution did not change upon tip modification. Hence, (Na-)modified STM tips can be used to perform scanning tunnelling measurements on the cleaved  $\text{Na}_2\text{IrO}_3$  surface.

Summary on the tunnelling conditions in UHV:

- Cleaved  $\text{Na}_2\text{IrO}_3$  surfaces stay clean and stable in UHV.
- Stable tunnelling contact possible at 300 K and 80 K.
- Despite high defect density on the surface, stable tunnelling is possible.
- Atomic resolution and measurement stability can be maintained even with in-situ modifications of the STM tip.



## 6.2 Impact of Tip Modifications on the $dI/dV$ -Spectra Taken on the $\text{Na}_2\text{IrO}_3$ Surface

While tip modifications as shown in Figure 6.4 have no obvious impact on the topographic results, we have also investigated if tip modifications leave tunnelling spectroscopy data unchanged too. In Figure 6.6, various tunnelling spectra as well as the respective position on the (1x1)-reconstructed surface the spectra were recorded on is shown. The temperature was 300K for the measurements.

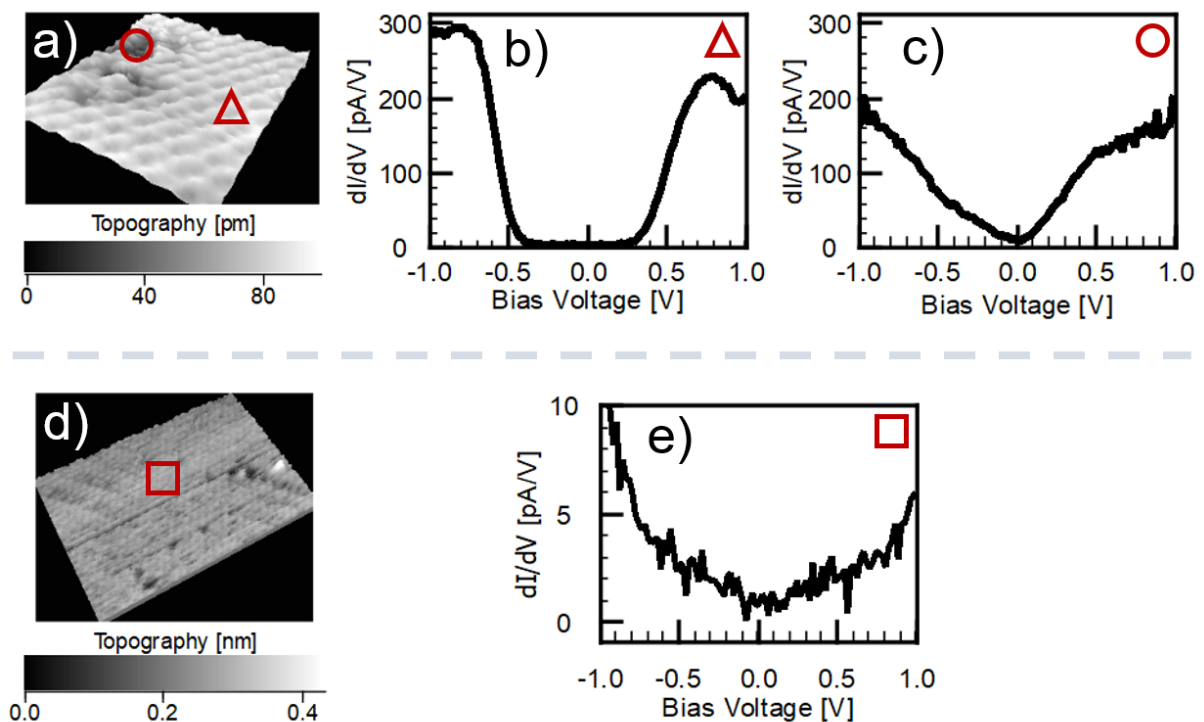


Figure 6.6 Observation of two different spectral characteristics on the  $\text{Na}_2\text{IrO}_3$  surface measured at 300 K with tunnelling spectroscopy. The bias voltage setpoint is -1 V, the tunnelling current setpoint is 100 pA. a) (1x1)-reconstructed surface with clean areas and defects. b)  $dI/dV$ -spectrum taken on the free surface (position marked in a)). On the free surface, an open spectral gap of  $\sim 0.8$  eV is observed. At -0.45 V and 0.35 V, the  $dI/dV$  signal shows a steep increase. c) At the defect, a V-shaped closing of the spectral gap is found. The minimum is located at the Fermi level. d) Clean, (1x1)-reconstructed surface measured with a different STM tip than a) but with identical setpoint. e) Spectrum taken on the clean surface as marked in d). The spectral gap is closed in a linear, V-shaped fashion.

The  $dI/dV$  spectrum in Figure 6.6 b) was taken on the clean surface, i.e. on the (1x1)-reconstructed  $\text{Na}_2\text{IrO}_3$  surface without adjacent defect. It shows no spectral weight in an extended voltage interval around the Fermi level. Bias voltage intervals with no apparent spectral weight will be referred to as spectral weight gap or spectral gap in the following. It is worth noting that the finding of a large spectral gap is in accordance with previously reported

STM/STS works from Lüpke et al. [18], [29] that interpret the spectral gap as the Mott gap separating the Ir 5d  $j_{\text{eff}}=1/2$  Hubbard bands in  $\text{Na}_2\text{IrO}_3$ .

A  $dI/dV$  curve taken at a defect on the same surface, here a sodium vacancy, with the same STM tip as in Figure 6.6 b) is depicted in Figure 6.6 c). At the defect, no spectral gap is found and the  $dI/dV$  signal shows a linear bias voltage dependence within the spectral gap region from Figure 6.6 b). This linear  $dI/dV$  dependency on the bias voltage will be referred to as “V-shaped” in this thesis. The V-shaped  $dI/dV$  has its minimum at the Fermi level, where the spectral weight is close to the resolution limit. Most importantly, such a gap closing was not found in STM/STS works before, where only a decrease of the Mott gap size by  $\sim 0.25$  eV was reported at defects [18], [29].

To investigate whether the V-shaped spectral signature is tied to defects only, Figure 6.6 d), e) show a tunnelling spectroscopy measurement on the clean (1x1)-reconstructed surface with a different STM tip at a different position on the sample. Temperature and tunnelling setpoints were identical to the measurements in Figure 6.6 a)-c). The spectrum in Figure 6.6 e) shows a V-shaped  $dI/dV$ , similar to that in Figure 6.6 c), i.e. tunnelling spectroscopy occasionally reveals a V-shaped spectral signature also on the clean (1x1)-reconstructed  $\text{Na}_2\text{IrO}_3$  surface. Hence, even though having an influence, it is not the local  $\text{Na}_2\text{IrO}_3$  surface structures alone that determine what type of  $dI/dV$  spectrum is measured.

To study what determines the different  $dI/dV$  characteristics observed on the  $\text{Na}_2\text{IrO}_3$  surface, the finding that differently modified STM tips can lead to similar topographic results for the  $\text{Na}_2\text{IrO}_3$  surface (chapter 6.1) is considered. Simultaneously to the topographic measurement in Figure 6.4, a  $dI/dV$ -spectrum was taken at every pixel, allowing to correlate the change of the tip modification to changes of spectroscopic data. Spatially resolved  $dI/dV$  maps at -1 V, -0.5 V, 0 V, 0.5 V and 1 V are depicted in Figure 6.7 a), exhibiting multiple tip modification dependent characteristics. To simplify the following descriptions, all terraces in the topography in Figure 6.7 a) are labelled. The STS-maps show a pronounced impact of the tip modification on the absolute conductivity as is seen by comparing the data for the terraces R.1.1/2/3 with the data for R.2.1/2/3, where the absolute  $dI/dV$  values change drastically. This change seems to manifest itself in a reduction of differential conductance (i.e.  $dI/dV$ ) due to the tip modification (compare R.1.1 to R.2.1 and R.1.3 to R.2.3). However, at positive bias voltages, the situation is the other way around for the terraces R.1.2 and R.2.2, where the conductance rises after the tip modification.

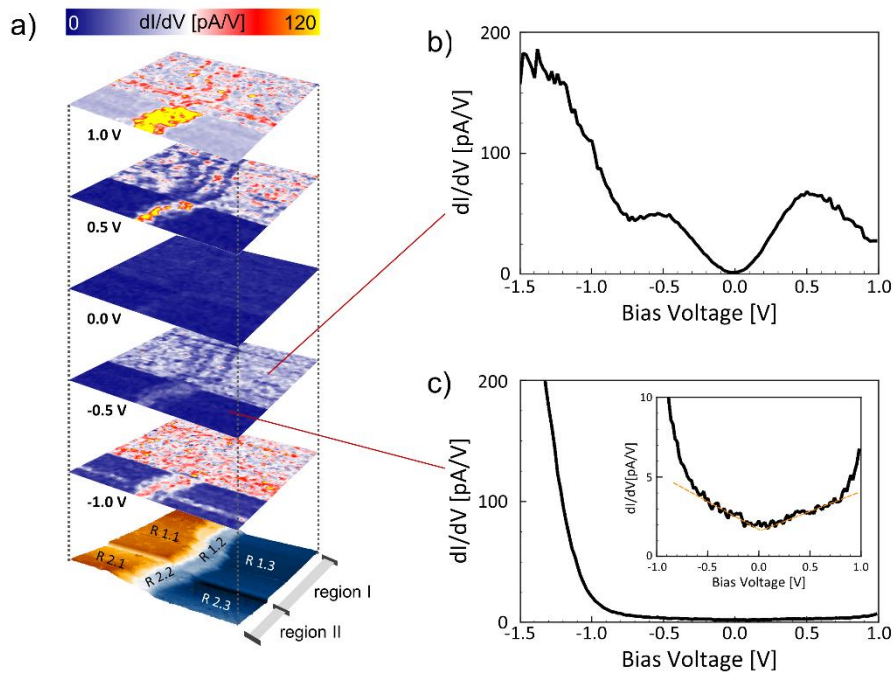


Figure 6.7 Impact of the STM tip modification on spectroscopic data on the  $\text{Na}_2\text{IrO}_3$  surface. a) Scanning tunnelling spectroscopy data at different bias voltages covering multiple  $(1 \times 1)$ -reconstructed terraces, separated by step edges. The instantaneous jump in the topographic height (bottom) splits the dataset in region I and region II and marks the position where the modification of the STM tip changed. The terraces are additionally labelled for reference in the text. The impact of the tip modification is visible in the STS maps. b)  $dI/dV$  spectrum taken on the free surface before the tip modification occurred (region I), exhibiting broad peaks at  $\pm 0.5$  V. The  $dI/dV$  minimum is at the Fermi level. c)  $dI/dV$  spectrum on the free surface taken after the tip modification occurred (region II). The inset shows a zoom-in of the  $dI/dV$  curve around the Fermi level. Compared to b), the peaks vanished, and the overall conductance is reduced. The overall  $dI/dV$ -signal does not vanish at any bias voltage but reaches the resolution limit. The gap closing resembles a V-shaped  $dI/dV$ .

Next to a change of the absolute  $dI/dV$  value, it is evident that the influence of local surface structures is different in region I compared to region II, which can be seen best in the 1 V STS map. Local defect structures on the free surface as well as step edges are more pronounced in the  $dI/dV$  map in region I. In region II, the  $dI/dV$  characteristic at the step edges is identical to the adjacent terraces. Furthermore, it is observed that even when comparing terraces within one region, the tip modification has an influence. In region I, all terraces R.1.1, R.1.2 and R.1.3, share similar characteristics. This changes drastically in region II, where R.2.2 exhibits higher  $dI/dV$  values than R.2.1 and R.2.3 in every STS-map.

The  $dI/dV$  spectra shown in Figure 6.7 b) and c) were measured on clean surfaces at the marked positions with identical measurement settings. The  $dI/dV$ -spectrum in b) - i.e. before the tip modification - shows two broad peaks at  $-0.5$  V and  $0.5$  V, respectively. The minimum of the  $dI/dV$  signal is at the Fermi level. Hence, this  $dI/dV$  curve is different compared to both spectral types found in Figure 6.6. After the tip modification, the spectral characteristic changes drastically (Figure 6.7 c)). The peaks at  $\pm 0.5$  V vanish, and the overall conductance is reduced.

As seen in the inset, the  $dI/dV$  curve then exhibits a V-shaped  $dI/dV$  characteristic around the Fermi level, similar to the observations in Figure 6.6 c) and e).

Briefly summarized, the findings are:

- The measured spectral characteristics depend on the modification of the tip.
- Different types of  $dI/dV$  spectra can be observed on the clean, (1x1)-reconstructed  $\text{Na}_2\text{IrO}_3$  surface. The measured spectral characteristics can depend on local surface structures like defects and step edges.

In the following, the impact of the tip modification on the observed  $dI/dV$  spectra is discussed in two possible scenarios.

#### Scenario 1: STM tip modifications change the tip density of states.

The basic assumption for this scenario is that the tip density of states  $\rho_T$  changes upon modification while the sample density of states  $\rho_S$  and the transmission probability  $T$  either remain unaffected or that changes are negligible. Equation 5.8 relates the  $dI/dV$  signal to the products of the local densities of states of tip and sample as well as the transmission term. Hence, a change of  $\rho_T$  upon tip modification would directly result in a change of the measured  $dI/dV$ .

Freshly prepared STM tips consist of tungsten that is assumed to have an energy independent density of states within the energy interval used in the employed STM measurements (here  $\pm 1.5$  eV around the Fermi level). Assuming, that modifications of the STM tip occur by sodium attachment to, or detachment from, the tip apex as proposed in chapter 6.1, the composition of elements at the tip-apex changes upon its modification. Here, the different  $dI/dV$  spectra at similar local sample surface structures, as in the case presented in Figure 6.6 b) and e), would not arise from characteristics of the sample electronic structure but are the result of a change of the tip LDOS. However, the spectral difference between Figure 6.6 b) (0.8 eV spectral gap) and e) (no gap) seems rather extreme for this explanation. Furthermore, it is surprising in this context that Figure 6.6 c) and e) show similar spectroscopic characteristics, even though the comparison between Figure 6.6 b) and e) suggest different states of the tip. It would be a rather surprising coincidence if different combinations with different tip and sample LDOS would by chance result in the same  $dI/dV$  characteristics.

### Scenario 2: The transfer matrix element changes upon tip modification.

In this scenario measured  $dI/dV$  characteristics result from electronic properties inherent to the cleaved  $\text{Na}_2\text{IrO}_3$  surface, but the state of the tip determines if and to which extend spectral characteristics are detected. In the STM theory presented in chapter 5.5, it is stated in equation 5.3 that the tunnelling current, and hence also the  $dI/dV$  signal, is proportional to the sum over all transitions from initial states to final states. For each transition, the respective transition matrix element  $M_{\mu\nu}$  weights the contribution of the transition between states  $\mu$  and  $\nu$ . The transition matrix elements depend on the state of the tip, the decay constant in vacuum and the sample wavefunction at the position of the tip apex according to Table 5.1. Hence, if a modification of the tip changes the tip-state, e.g. from d-like to s-like, the contributions of transitions corresponding to different sample states to the overall tunnelling current may change as well, resulting in different measured  $dI/dV$  spectra. Considering further that sodium valence states have s-character while tungsten valence states have d-character, tip modifications by sodium may fit well into this picture even though being an oversimplification, as hybridized states would need to be considered.

The line of argumentation from scenario 2 is supported by  $I_T(U, d)$ -data taken on the freshly cleaved  $\text{Na}_2\text{IrO}_3$  surface at 80 K depicted in Figure 6.8. Figure 6.8 b) shows  $\ln(I_T(d))$ -curves for multiple bias voltages. After approaching the tip  $\sim 0.25$  nm towards the surface, a hump is observable in each curve (black arrow) except for  $|V| = 1.5$  V, where the experimentally chosen current limitation of 1 nA is reached before the tip approaches 0.25 nm. In Figure 6.8 c)-e),  $dI/dV$  curves calculated from the  $I_T(U, d)$  data after approaching the tip by c) 0.1 Å, d) 1.4 Å and e) 3 Å are depicted. For the STM tip far away from the sample surface, the  $dI/dV$  spectrum shows in-gap states and no spectral gap. The minimum of the  $dI/dV$  signal is in the vicinity of the Fermi level. Upon approaching the STM tip towards the sample a spectral weight shoulder emerges at  $\sim -0.5$  V (Figure 6.8 d), e), red arrows).

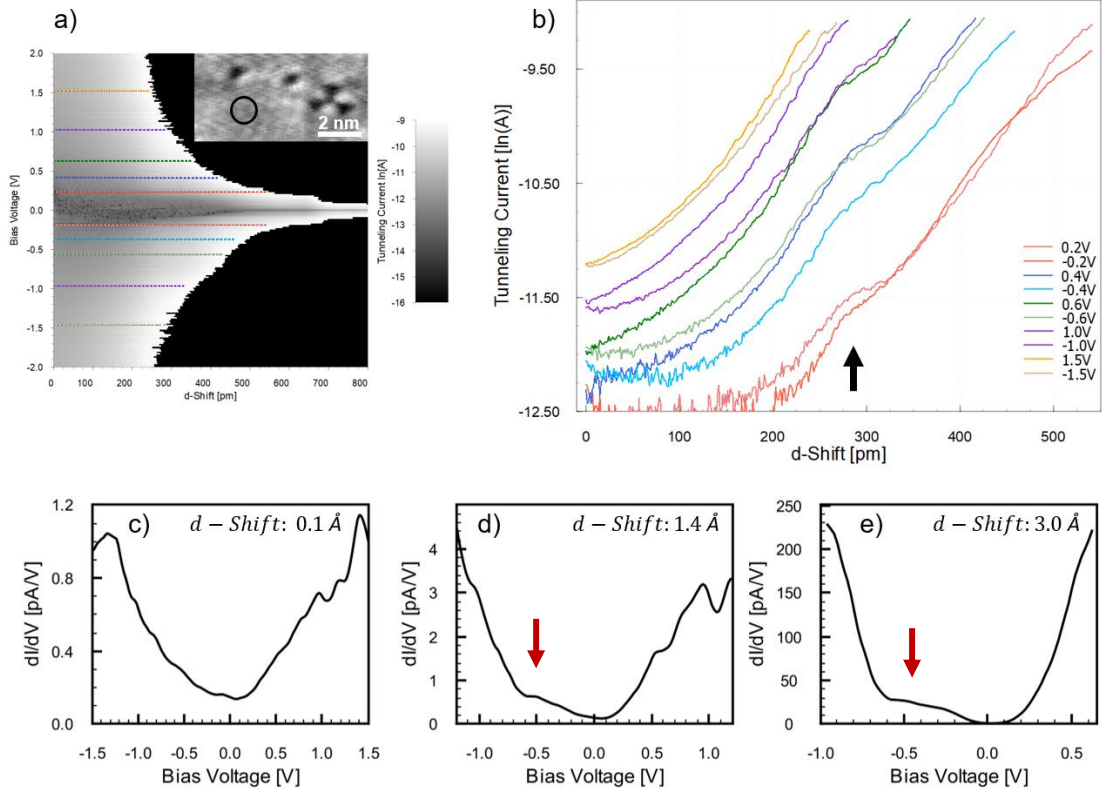


Figure 6.8 Tip-sample distance and bias voltage dependent measurement of the tunnelling current on the freshly cleaved, (1x1)-reconstructed  $\text{Na}_2\text{IrO}_3$  surface at 80 K. a)  $I_T(U, d)$ -dataset covering the voltage range from -2 V to 2 V and a tip-approach of 0.8 nm towards the sample surface. The initial setpoint determining the initial tip-sample distance is 2 V at 10 pA. The topography in the inset shows the measurement position (black circle). b) Tip-approach dependent tunnelling current for different bias voltages, extracted from a) at the dotted coloured lines. After a tip-approach of  $\sim 0.25$  nm, the curves show a feature deviating from the linear  $\ln(I)$  vs.  $d$  behaviour (black arrow). c)–e)  $dI/dV$  curves calculated from the  $I_T(U, d)$ -data. c)  $dI/dV$  after approaching the tip by  $0.1 \text{ \AA}$ , showing in-gap states and no spectral gap. d)  $dI/dV$  after approaching the tip by  $1.4 \text{ \AA}$ . A spectral weight shoulder emerges at  $\sim -0.5$  V. e)  $dI/dV$  after approaching the tip by  $3 \text{ \AA}$ . The spectral weight shoulder from d) is more pronounced.

The hump in Figure 6.8 b) and the emergence of spectral features in dependence of the tip sample distance in Figure 6.8 c)–e) indicate the existence of multiple transmission channels. For the  $I_T(U, d)$  curves, this can be seen from the dependence of the tunnelling current on the tip-sample distance  $d$  that is given by the transmission factor  $T$  introduced in chapter 5.5.5:

$$I_T \propto T(\bar{\phi}, d) \propto \exp\left(-2d \sqrt{\frac{2m}{\hbar^2} \bar{\phi}}\right) = \exp(-2d\kappa) . \quad 6.1$$

Here,  $\kappa = \sqrt{2m\bar{\phi}}/\hbar$ , denotes the decay constant in vacuum with  $\bar{\phi} = (\phi_S + \phi_T)/2$ , where  $\phi_S$  and  $\phi_T$  are the work function of sample and tip, respectively. Usually, this approach is used to estimate the size of the tunnelling barrier to extract the sample's work function from this. From equation 6.1, plotting  $\ln(I_T)$  vs.  $d$  should yield a linear

curve. Hence, a deviation from a linear slope in a  $\ln(I_T)$  vs.  $d$  plot indicates that at least two different transmission channels with different  $\kappa$  are present.

From the discussions of the two scenarios above, scenario 2 is plausible and suitable to explain the spectroscopic data presented in Figure 6.6, Figure 6.7 and Figure 6.8. Scenario 1 implies that tip modifications could open an 0.8 eV band gap at 300 K, which even though not impossible, seems unlikely for a metallic tip. Hence, in the scope of this work scenario 2 will be used in the discussion of the tunnelling spectroscopy data. To simplify the description, the observation of different  $dI/dV$  characteristics corresponding to sample surface states with differently modified tips will be referred to as the addressability of states. Presuming that local sample surface structures have an influence on the available transmission channels, the combination of the electronic state of the (modified) STM tip and the local  $\text{Na}_2\text{IrO}_3$  surface structure determines the signal recorded in STS. This model, assuming the tip modifications result from sodium at the tip apex, is sketched in Figure 6.9.

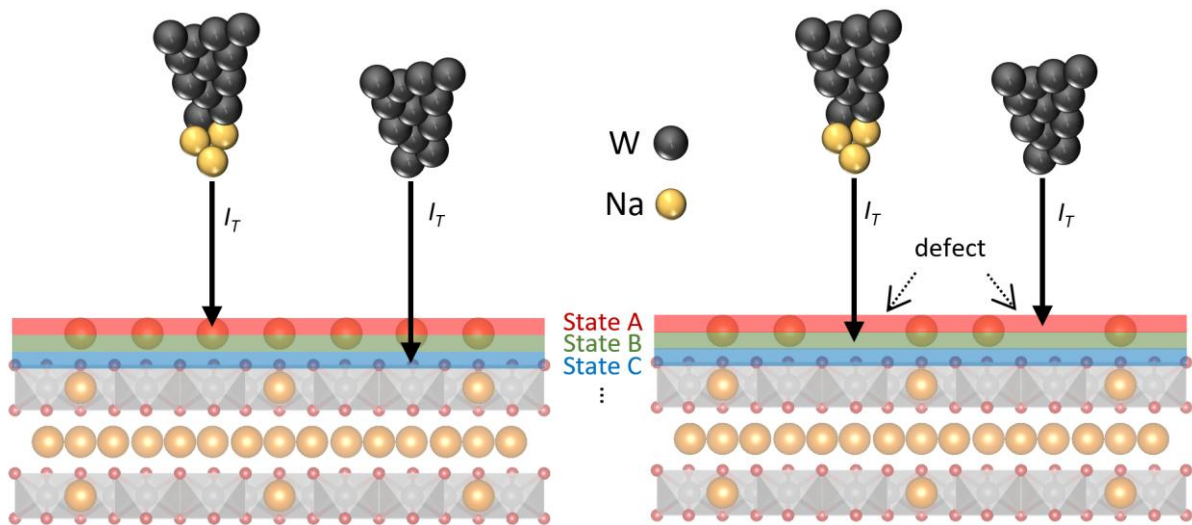


Figure 6.9 Model of the addressability of states depending on the electronic structures of STM tip and sample surface. Usually, STM and STS investigations seek to maintain clean tungsten STM tips to establish reproducible conditions. In the case of the  $\text{Na}_2\text{IrO}_3$  surface the addressability of states inherent to the material might be dependent on both, the modification of the STM tip with sodium and the local structure of the surface.

With the concept of scenario 2, spectroscopic data similar to that shown in Figure 6.6 c), e) and Figure 6.7 would not have been observed in former investigations since restoring the tip by cleaning off modifications would lead to addressing the same  $\text{Na}_2\text{IrO}_3$ -states in every STS measurement, that happen to be those corresponding to a large band gap for the (1x1)-reconstructed  $\text{Na}_2\text{IrO}_3$  surface at room temperature. The picture that all measured  $dI/dV$



spectra reflect the electronic characteristics of the  $\text{Na}_2\text{IrO}_3$  surface implies that the number of observable spectral types is limited, while the number of observable spectral types in scenario 1 could scale with the number of different tip modifications.

Independently of the scenario, it is important to note that  $dI/dV$  spectra were measured on the clean (1x1)-reconstructed surface that show spectral weight in the whole bias voltage range from -1 V to 1 V (e.g. Figure 6.6 c), e), Figure 6.7 c), Figure 6.8 a)). This implies that in-gap states are present at the freshly cleaved  $\text{Na}_2\text{IrO}_3$  surface (and addressed in dependence of the tip modification), as the  $dI/dV$  signal at a given energy is proportional to the tip LDOS multiplied with sample LDOS at this energy. This means, that the  $\text{Na}_2\text{IrO}_3$  surface exhibits a density of states within the previously interpreted  $\text{Na}_2\text{IrO}_3$  Mott gap energy interval (chapter 3.4).

Attempts to actively control the modification of the STM tip by sodium, e.g. by approaching the STM tip to the  $\text{Na}_2\text{IrO}_3$  surface to pick up single sodium atoms, were employed in this work but not successful, leaving observations like in Figure 6.6 and Figure 6.7 to be a matter of chance. Sampling with different tips on multiple crystals, and multiple positions on the respective cleaved surface yields data that can be searched for robust spectral features. Such an extensive collection of data was done in the experimental work for this thesis.

Summary on the addressability of  $\text{Na}_2\text{IrO}_3$  states:

- Three different spectral types are measured (addressed) on the  $\text{Na}_2\text{IrO}_3$  surface.
- The modification of the STM tip and the local surface structure determine the addressed spectral type.
- At least one spectral type with in-gap spectral weight was found.
- Discussing possible underlying processes, the measured spectral types are attributed to the electronic properties of the  $\text{Na}_2\text{IrO}_3$  surface.

### 6.3 Generic Spectral Types Found on the $\text{Na}_2\text{IrO}_3$ Surface

Large amounts of STM/STS-measurements, covering various STM tips and tip modifications as well as various  $\text{Na}_2\text{IrO}_3$  samples and local structures, were performed to investigate the spectral types found on the cleaved  $\text{Na}_2\text{IrO}_3$  surface. Measurements were performed at 80 K as well as 300 K. It was found that each measured  $dI/dV$  spectrum can be described using only the three generic spectral types shown in Figure 6.10.

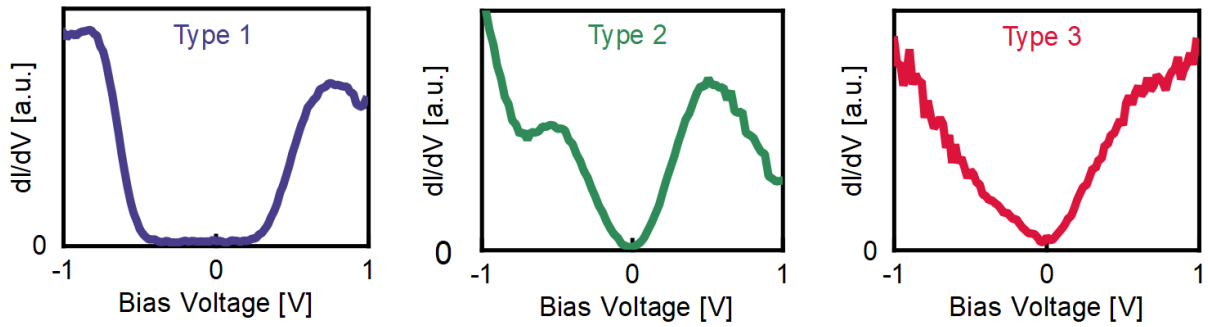


Figure 6.10 Three generic types of  $dI/dV$  spectra found on the freshly cleaved  $\text{Na}_2\text{IrO}_3$  surface. Each  $dI/dV$  spectrum measured on the  $\text{Na}_2\text{IrO}_3$  surface can be described via these three types.

These three spectral types will be detailed in the following. If not stated differently, all presented  $dI/dV$  data in this section were measured on the clean, (1x1)-reconstructed surface without adjacent defects. STM/STS measurements done at 8 K using optical excitation of charge carriers are treated separately in chapter 6.5, since the optical excitation might introduce additional effects that need to be considered.

### 6.3.1 Spectral Type 1 – Open Spectral Gap

A prototypical dataset of type 1 spectra for 300 K and 80 K is depicted in Figure 6.11. The corresponding topographies are depicted in Figure 6.11 a) and c).

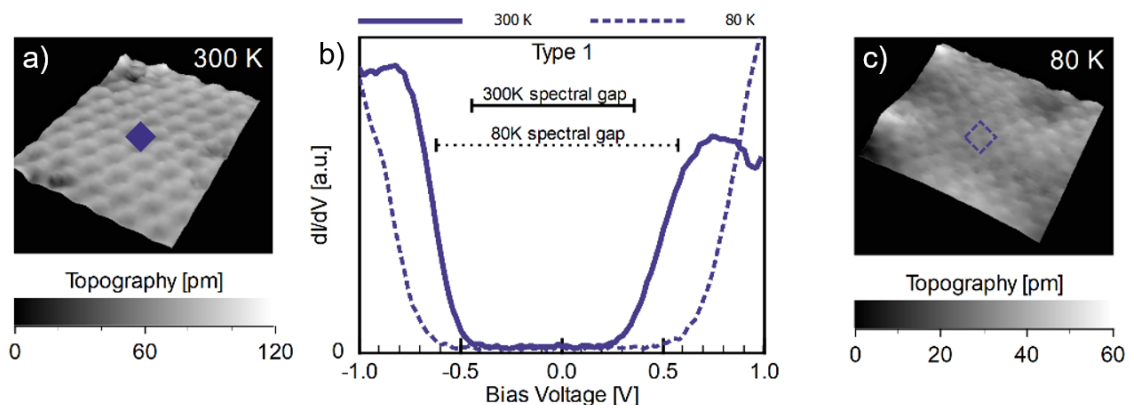


Figure 6.11 Type 1 tunnelling spectra showing a spectral gap between  $-0.45$  V and  $0.35$  V (300 K) and between  $-0.6$  V and  $0.6$  V (80 K). The onsets of conductance at the borders of the gap manifest as steep flanks, as can be seen in b). The topographies in a) and c) show the (1x1)-reconstructed  $\text{Na}_2\text{IrO}_3$ -surfaces where the spectra in b) were taken (marked by blue symbols). The setpoint for the topographies was  $-1$  V,  $100$  pA.

The  $dI/dV$  spectra in Figure 6.11 b) exhibit a voltage interval where the conductance is below the experimental resolution limit. This interval lies between -0.45 V and 0.35 V at 300 K and between -0.6 V and 0.6 V at 80 K. The according spectral gap has a size of  $\sim 0.8$  eV at 300 K and increases to 1.2 eV at 80 K. The gap size and its increase with decreasing temperature is similar to the values reported in previous STS measurements where the spectral gap was attributed to the  $\text{Na}_2\text{IrO}_3$  Mott gap [18], [29]. In contrast, (spatially resolved) ARPES and optical conductivity measurements report a Mott gap of 0.34 eV - 0.4 eV with no significant temperature dependence (chapter 3.1).

Two scenarios are discussed as possible pictures underlying type 1 spectra. The first scenario denotes the spectral gap to be the Mott gap between the Ir 5d  $j_{\text{eff}}=1/2$  Hubbard bands. The second scenario assumes that the Hubbard bands are not addressed when measuring type 1 spectra, leaving the spectral gap to be the energy gap between the Ir 5d  $j_{\text{eff}} = 3/2$  and the Ir 5d  $e_g$  bands (see chapter 2.2.3, Figure 2.6).

Scenario 1: The type 1 spectral gap corresponds to the Mott gap.

This scenario attributes type 1 spectra to the  $\text{Na}_2\text{IrO}_3$  Mott gap between the iridium 5d  $j_{\text{eff}} = 1/2$  bands, i.e. the Hubbard bands, illustrated in Figure 6.12.

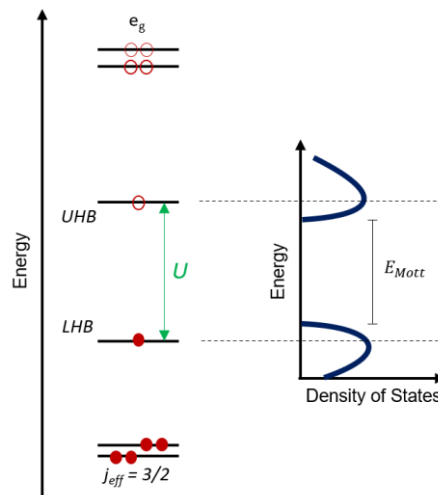


Figure 6.12 Assignment of the type 1 spectral gap to the  $\text{Na}_2\text{IrO}_3$  Mott gap. The  $\text{Na}_2\text{IrO}_3$  energy diagram (single iridium picture) for the Ir 5d states including crystal field splitting, spin-orbit coupling, and Hubbard repulsion is shown on the left. The highest occupied band is the LHB, the lowest unoccupied band is the UHB, that arise from the  $j_{\text{eff}}=1/2$  bands due to Hubbard repulsion  $U$ . A sketched density of states corresponding to type 1  $dI/dV$  spectra is plotted on the right. In this picture, the DOS outside the Mott gap arises from the LHB and UHB.

In the published STM/STS works [18], [29], this association was natural as only spectra of type 1 were found. Without the information that other spectral types exist, and since the Fermi level lies within the Mott gap, the observation of any spectral gap around the Fermi level has led to the assignment of this gap to the  $\text{Na}_2\text{IrO}_3$  Mott gap.

However, an absolute Mott gap size of  $\geq 0.8$  eV at the (1x1)-reconstructed surface was reported by STM/STS investigations only (Figure 3.10). ARPES and optical conductivity measurements neither report a comparably large Mott gap nor a significant temperature dependence of the Mott gap, Figure 3.8, Figure 3.9, and [19], [26]. Moreover, from the theory on Mott insulators, a significant temperature dependence - which is observed here - of the Mott gap is not expected (see chapter 2.2.3).

### Scenario 2: the type 1 spectral gap corresponds to the Ir 5d $j_{\text{eff}}=3/2$ - $e_g$ energy gap

With the information that spectral types with apparent spectral weight within the type 1 gap exist (chapter 6.2), the assignment of the type 1 spectral gap to an energy gap different from the Mott gap is considered. The premise for this scenario is that the  $j_{\text{eff}}=1/2$  Hubbard bands are not addressed in tunnelling spectroscopy when observing type 1 spectra. From the energy diagram for the Ir 5d states depicted in Figure 6.13, this leaves three possible energy gaps to consider:  $E_{j_{3/2},\text{UHB}}$ ,  $E_{\text{LHB},e_g}$  and  $E_{j_{3/2},e_g}$ . Presuming that the Mott gap size of 0.34 eV - 0.4 eV reported from ARPES and optical conductivity measurements is correct, the type 1 spectral gap would have to be very asymmetric if it corresponded to either  $E_{j_{3/2},\text{UHB}}$  or  $E_{\text{LHB},e_g}$ , since the LHB or UHB band edge would be much closer to the Fermi level than the  $j_{\text{eff}}=3/2$  or  $e_g$  band edges. Hence, the proposed picture in scenario 2 is that the type 1 spectral gap corresponds to the energy gap between the highest Ir 5d  $j_{\text{eff}}=3/2$  and the lowest Ir 5d  $e_g$  band, i.e.  $E_{j_{3/2},e_g}$ .

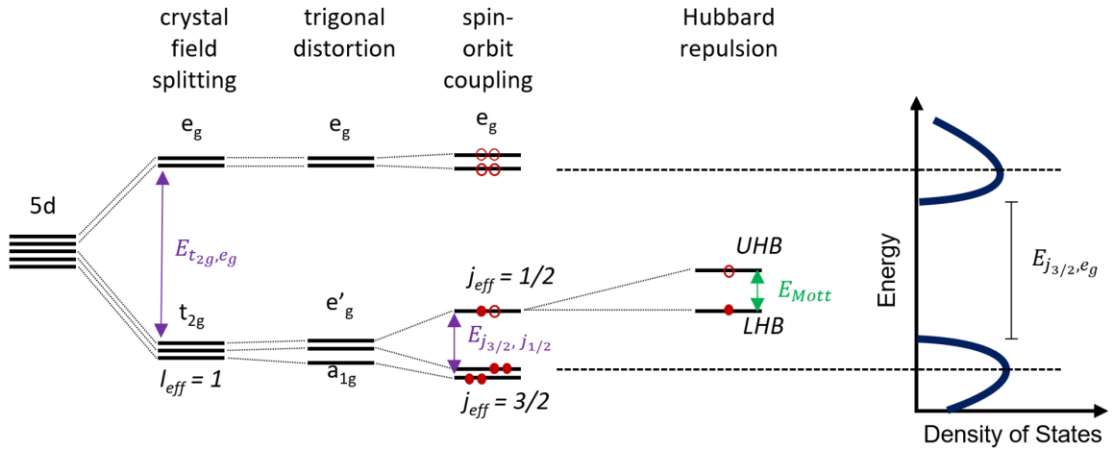


Figure 6.13 Assignment of the type 1 spectral gap the energy gap between  $j_{\text{eff}}=3/2$  and  $e_g$  states in  $\text{Na}_2\text{IrO}_3$ , i.e.  $E_{j_{3/2}, e_g}$ . The  $\text{Na}_2\text{IrO}_3$  energy diagram (single Ir picture) for the Ir 5d states (left) shows the influences of crystal field splitting, spin-orbit coupling and Hubbard repulsion. In the framework of scenario 2, the type 1  $dI/dV$  signal outside the spectral gap corresponds to density of states from  $j_{\text{eff}}=3/2$  and  $e_g$  states, while the  $j_{\text{eff}}=1/2$  states are not addressed (right).

The dispersion and the relative energetic positions of the  $j_{\text{eff}}=3/2$  and  $e_g$  bands are subject to ongoing research [44]. To the best knowledge of the author of this thesis, only the energy separation from crystal field splitting  $\Delta E_{e_g, t_{2g}} \approx 2 \text{ eV} - 3 \text{ eV}$  was estimated from experimental results (see chapter 2.2.1), and no temperature dependent investigation was conducted in this regard. From research works using optical conductivity measurements, ARPES, x-ray absorption spectroscopy and ab-initio calculations, the onset of the highest  $j_{\text{eff}}=3/2$  band is estimated to be between  $-0.4 \text{ eV}$  and  $-0.6 \text{ eV}$  at room temperature [44], [120]. The energy separation between the  $j_{\text{eff}}=3/2$  and the upper  $j_{\text{eff}}=1/2$  Hubbard band was reported to be  $\sim 0.72 \text{ eV}$  [120]. As the  $e_g$ -bands energetically lie above the UHB, the  $j_{\text{eff}}=3/2$ - $e_g$  energy gap must be larger than  $0.72 \text{ eV}$  at  $300\text{K}$ , which is in accordance with the type 1 spectra at  $300 \text{ K}$ .

Furthermore, the strong temperature dependence of type 1 spectral gap can be explained in this framework. From semiconductors, it is well known that an increase of band gaps occurs with decreasing temperature, arising e.g. from changing interatomic distances [121]. In  $\text{Na}_2\text{IrO}_3$ , a change of interatomic distances would also impact the energy splitting in Ir  $t_{2g}$  and Ir  $e_g$  bands due to crystal field splitting, potentially leading to a considerable temperature dependence of  $E_{j_{3/2}, e_g}$ . This picture is reinforced by the STM/STS-observation of Lüpke et al. [29], stating that the type 1 spectral gap varies by  $0.25 \text{ eV}$  in the vicinity of vacancies, i.e. close to local alterations of the interatomic distances. Hence, the rather large absolute change by  $50 \%$  of the type 1 spectral gap from  $0.8 \text{ eV}$  at  $300 \text{ K}$  to  $1.2 \text{ eV}$  at  $80 \text{ K}$  can be explained in scenario 2, while scenario

1 (type 1 spectral gap  $\hat{=}$  Mott gap) fails to explain the temperature dependence, since it emerges from onsite electron-electron correlation.

In the context of addressability, scenario 2 implies that the transfer matrix element for  $\text{Na}_2\text{IrO}_3$   $j_{\text{eff}}=1/2$  wave functions is (nearly) zero for tip states leading to the observation of type 1 spectra, i.e. that a  $dI/dV$  emerging from  $j_{\text{eff}}=1/2$  states is below the STS resolution limit.

#### Summary on the Type 1 $dI/dV$ Spectra

- Type 1 spectra taken on the clean (1x1)-reconstructed  $\text{Na}_2\text{IrO}_3$  surface show a spectral weight gap of 0.8 eV at 300 K and 1.2 eV at 80 K.
- It is proposed that the  $\text{Na}_2\text{IrO}_3$  Hubbard bands are not addressed when type 1 spectra are observed by means of STS.
- Assigning the type 1 spectral gap to the  $j_{\text{eff}}=3/2-e_g$  energy gap is plausible and in accordance with other spectroscopic works.

#### 6.3.2 Spectral Type 2 – Symmetric In-Gap States

A typical dataset showing the second spectral type found on  $\text{Na}_2\text{IrO}_3$  surfaces at 300 K and 80 K is shown in Figure 6.14 b). The setpoints were chosen identically to the data shown in Figure 6.11.

At 300 K, type 2 spectra exhibit broad, symmetric  $dI/dV$  peaks with maxima at -0.5 V and 0.5 V. These peaks will be referred to as D (-0.5 V) and  $D^*$  (0.5 V). The full width half maximum is 0.4 V - 0.5 V for both peaks. The tails of peaks D and  $D^*$  result in a small  $dI/dV$  signal in the vicinity of the Fermi level (Figure 6.14 b), that reaches the resolution limit at the minimum. At negative voltages below -0.7 V the onset of another spectral feature is visible. Considering the energetic position, this feature resembles the onset of spectral weight at negative voltage from the steep flank bordering the type 1 spectral gap. No analogous onset of spectral weight is seen in the  $dI/dV$  curve at positive voltages.

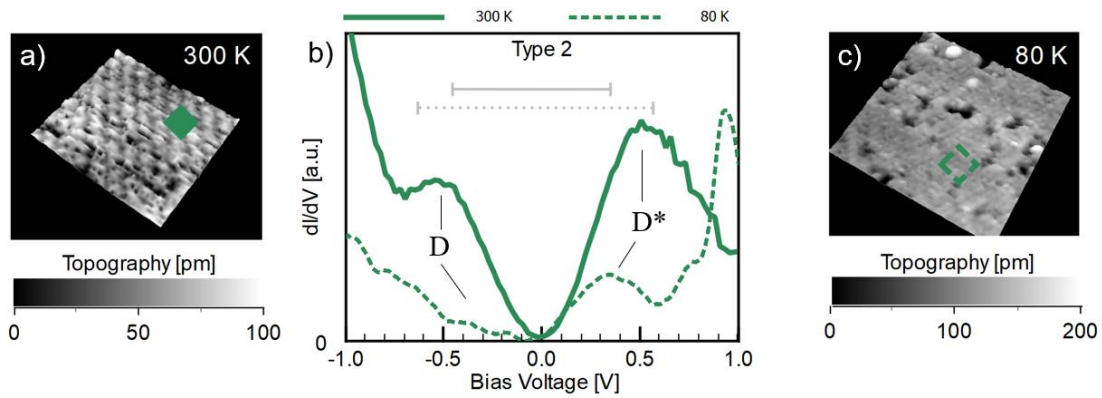


Figure 6.14. Type 2 tunnelling spectra showing  $dI/dV$  peaks, referred to as D and  $D^*$ , within the type 1 spectral gap voltage region. Measurements were done at 300 K (solid line) and 80 K (dashed line). The setpoint was -1 V, 100 pA. The topographies in a) and c) show the (1x1)-reconstructed  $\text{Na}_2\text{IrO}_3$ -surfaces where the spectra presented in b) were taken (marked by green symbols). b) At 300 K, the peak maxima are at -0.5 V (D) and 0.5 V ( $D^*$ ). The peaks are symmetrical with respect to the Fermi level with a FWHM of 0.4 V - 0.5 V for both peaks. At 80 K, the overall spectral weight of the peaks is reduced and only a small shoulder remains from D.  $D^*$  still manifests as distinct peak with the maximum at 0.35 V. For comparison, the type 1 spectral gap interval is marked in grey for 300 K (solid line) and 80 K (dashed line).

At 80 K, both peaks are less prominent. From D, only a tiny shoulder remains in the spectrum, while  $D^*$  is still observed as pronounced peak. The peak maximum of  $D^*$  is found at  $\sim 0.35$  V. The spectral weight in the vicinity of the Fermi level, i.e. the D and  $D^*$  tails, remains similar to the case at 300 K. Next to D and  $D^*$ , onsets of further spectral features are found at -0.5 V and 0.6 V. These onsets resemble the flanks bordering the spectral gap found in type 1 spectra at 80 K.

In the following, the possible origin of type 2 spectra is discussed in two scenarios. In scenario 1, D and  $D^*$  are assumed to emerge from the iridium  $j_{\text{eff}}=1/2$  states and hence represent the Hubbard bands. Scenario 2 incorporates the high defect density found on the cleaved  $\text{Na}_2\text{IrO}_3$  surface and denotes D and  $D^*$  to be related to defect states.

Scenario 1: the peaks D and  $D^*$  emerge from Ir-5d  $j_{\text{eff}}=1/2$  states.

The premise of this scenario is that the  $\text{Na}_2\text{IrO}_3$  Hubbard bands are not addressed in type 1 spectra but are addressed in type 2 spectra. Then, peak D corresponds to the LHB, while peak  $D^*$  corresponds to the UHB. This scenario is visualized in Figure 6.15.



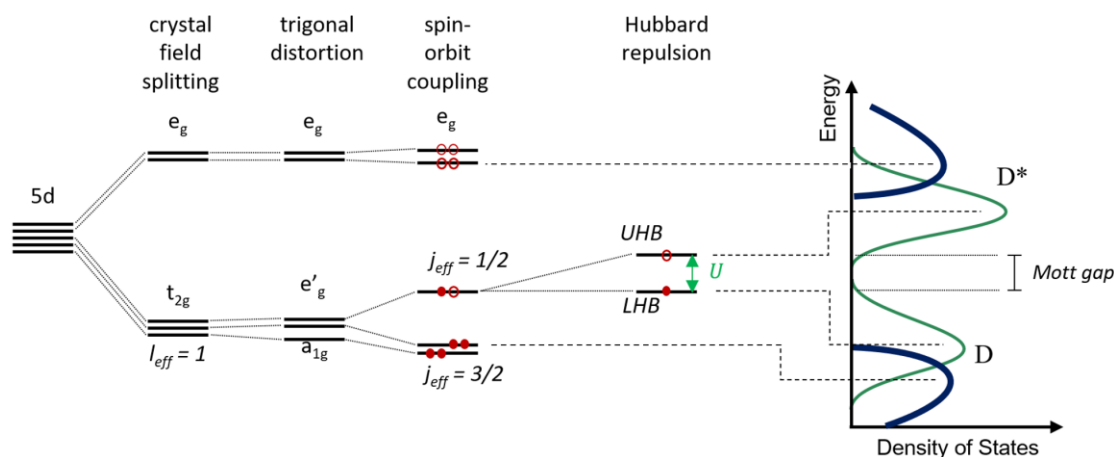


Figure 6.15 Assignment of the type 2 spectral peaks D and D\* to the Na<sub>2</sub>IrO<sub>3</sub> Hubbard bands. The Na<sub>2</sub>IrO<sub>3</sub> energy diagram (single iridium picture) for the iridium 5d-states (left) shows the influences of crystal field splitting, spin-orbit coupling and Hubbard repulsion. In the framework of this scenario, the type 2 dl/dV peak D emerges from the LHB and peak D\* emerges from the UHB (right).

The Mott gap in Na<sub>2</sub>IrO<sub>3</sub> was reported by ARPES and optical conductivity works to have a size between 0.34 eV and 0.4 eV (see chapters 2.3 and 3.1). Additionally, it was reported that the Mott gap size is temperature independent between 8 K and 300 K. Ignoring the tails of the peaks D and D\* in the vicinity of the Fermi level, the spectral gap between the peaks D and D\* in type 2 spectra is estimated to have a size between 0.2 eV and 0.3 eV at 300 K and does not increase at 80 K. Despite being slightly smaller, this type 2 spectral gap resembles the Mott gap reported from ARPES and optical conductivity measurements. This implies that the small spectral weight from the peak tails close to the Fermi level was either not observed or not considered in the literature. From the full width half maximum of D and D\* at 300 K, the related bandwidth of the LHB and UHB would be estimated to ~1 eV. Here, ARPES investigations provide an unprecise picture, reporting bandwidths of the LHB between 0.1 eV and 1 eV (see chapter 3.1). From the theory of Mott-Hubbard insulators (chapter 2.2.3) it is known that the opening of a Mott gap requires the Hubbard repulsion to be larger than the bandwidth. Hence, a narrow band aids the formation of a Mott gap. However, this does not mean that a bandwidth of 1 eV forbids the opening of a Mott gap; it only implies that the Hubbard repulsion needs to be stronger compared to the case for narrower bands. It is also clear from the Mott-Hubbard-insulator theory that the LHB and the UHB have similar densities of states, as they arise from the same band that is split by the Hubbard repulsion. This Hubbard repulsion symmetrically shifts the LHB and UHB away from the Fermi level. Consequently, it would be expected that LHB and UHB result in similar dl/dV peaks that are symmetric around the Fermi level, exactly as observed with the D and D\* peaks.

This scenario implies that the type 1 spectral weight gap does not correspond to the Mott gap. Then, the onsets of spectral weight in type 1 spectra would be interpreted to arise from iridium  $j_{\text{eff}}=3/2$  and  $e_g$  states. Consequently, the onsets of spectral features at  $-0.7$  V (300 K),  $-0.5$  V (80 K) and  $0.6$  V (80 K) in type 2 spectra could be assigned to  $j_{\text{eff}}=3/2$  and  $e_g$  states. The spectral weight from  $e_g$  states is not observed in type 2 spectra at 300 K. A possible explanation is that the conductance provided by the states underlying the  $D^*$  peak overshadows the  $e_g$  -conductance at 300 K but not at 80 K. In this case,  $D^*$  would mask the onset of spectral weight from the  $e_g$  -states.

### Scenario 2: D and $D^*$ are related to defect states.

The premise of this scenario is that the  $\text{Na}_2\text{IrO}_3$  Hubbard bands are addressed in type 1 spectra. Then, peaks D and  $D^*$  would emerge from states within the  $\text{Na}_2\text{IrO}_3$  Mott gap. As no bands are apparent in the Mott gap, this scenario assigns the peaks D and  $D^*$  to defect states, even though type 2 spectra are observed in tunnelling spectroscopy measurements on the clean,  $(1 \times 1)$ -reconstructed surface. Nevertheless, for a detailed analysis the consequences from such a scenario are discussed here.

The picture is as follows: the high density of defects results in a significant spectral weight arising from the defect states throughout the whole  $\text{Na}_2\text{IrO}_3$  surface (and possibly the bulk). On homogeneous surfaces, defect states usually correspond to sharp  $dI/dV$  peaks. The small average inter-defect distance of only a few nanometres results in a considerable overlap of the wavefunctions corresponding to the defect states, leading to a broadening of the spectral weight peaks in the  $dI/dV$  spectra. This might be in accordance with the bandwidth of  $\sim 1$  eV at 300 K derived from the FWHM of D and  $D^*$ . In this scenario, the peaks D and  $D^*$  are proposed to correspond to acceptor (D) and donator ( $D^*$ ) states.

Comparing the two presented scenarios, scenario 1 is favoured as it provides a simpler picture than scenario 2 to explain the observations tied to spectra of type 2. Furthermore, scenario 1 is consistent with the interpretation that the type 1 spectral gap corresponds to the  $j_{\text{eff}}=3/2$ - $e_g$  energy gap, fitting to the  $\text{Na}_2\text{IrO}_3$  Ir 5d energy diagram (Figure 6.15). Finally, it also provides a straightforward picture regarding the addressability of states. The  $\text{Na}_2\text{IrO}_3$  Hubbard bands arise from the  $j_{\text{eff}}=1/2$  states, corresponding to a single d-orbital, while the  $j_{\text{eff}}=3/2$  and the  $e_g$  states each correspond to two other d-orbitals. Hence, the observation of type 2 spectra would depend on the transfer matrix element of the transition between the  $j_{\text{eff}}=1/2$  orbital and the STM tip.

## Summary on the Type 2 dI/dV Spectra

- Type 2 spectra taken on the clean  $\text{Na}_2\text{IrO}_3$  surface show two dI/dV peaks within the type 1 spectral weight gap.
- These dI/dV peaks are assigned to the  $\text{Na}_2\text{IrO}_3$  Hubbard bands.
- The dI/dV peak position fits to a temperature independent Mott gap size of 0.2 eV – 0.3 eV.

### 6.3.3 Spectral Type 3 – Linear Band Gap Closing

The third and final generic spectral type found on the  $\text{Na}_2\text{IrO}_3$  surface is depicted in Figure 6.16. dI/dV curves at 300 K and 80 K are shown in Figure 6.16 b). The underlying clean  $\text{Na}_2\text{IrO}_3$ -surfaces are (1x1)-reconstructed as seen Figure 6.14 a) and c). The setpoints were chosen identically to the data shown in Figure 6.11 and Figure 6.14 (-1 V, 100 pA).

The defining characteristic of type 3 spectra is a V-shaped spectral weight within the spectral gap region in type 1 spectra. Here, the term “V-shaped” refers to the shape of the dI/dV vs. V curve within a voltage interval around the Fermi level. For 300 K, this interval spans from -0.4 V to 0.45 V. For 80 K, this interval is larger, extending from -0.65 V to 0.55 V (black arrows in Figure 6.16 b)). These temperature dependent intervals resemble the position of the spectral weight gaps found in type 1 spectra. Outside these voltage intervals, the type 3 dI/dV curves deviate from the V-shaped course. The minimum of the V-shape is always situated at the Fermi level and in close proximity of this minimum the dI/dV curve is slightly “rounded”, deviating from the otherwise linear course. This rounding can be attributed to thermal smearing.

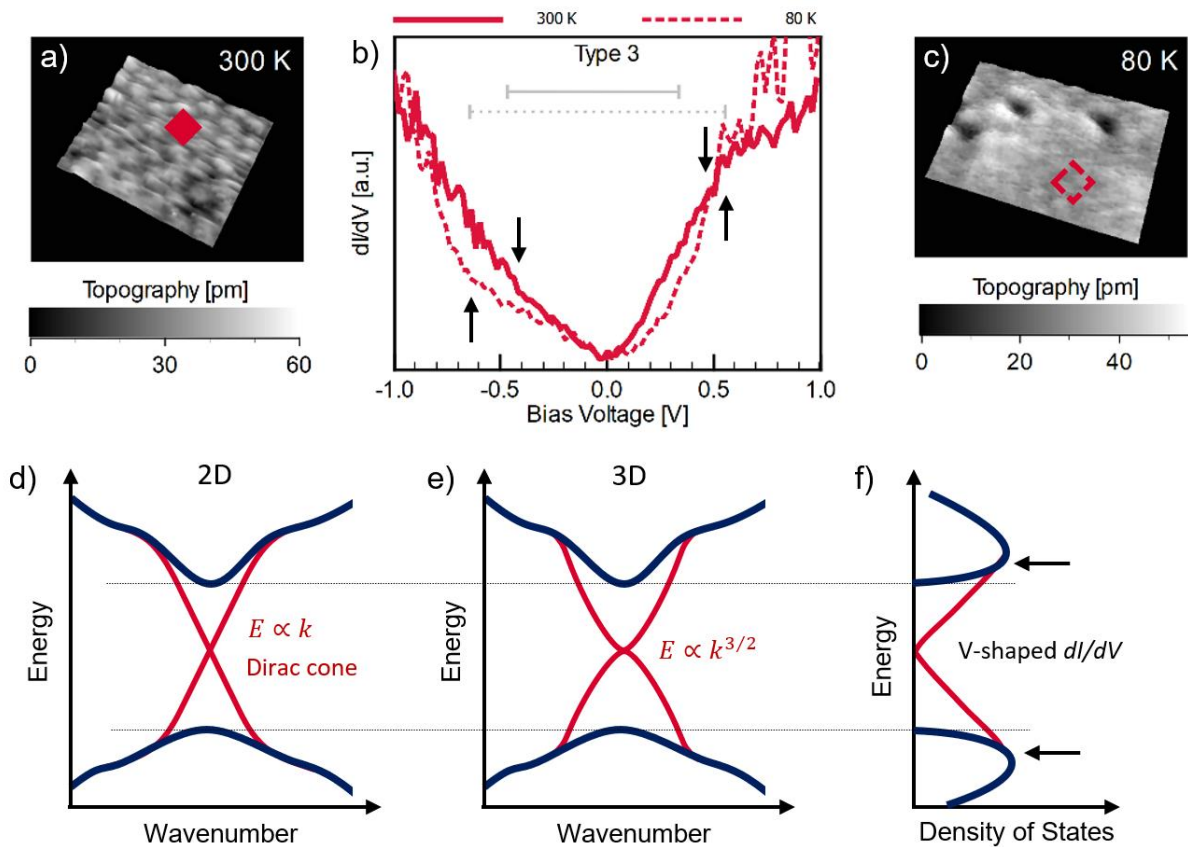


Figure 6.16 Type 3 tunnelling spectra showing in-gap states with a linear  $dI/dV$  vs.  $V$ . The topographies in a) and c) show the  $(1 \times 1)$ -reconstructed  $\text{Na}_2\text{IrO}_3$ -surface at 300 K and 80 K. The spectra in b) were taken at the position marked by the red symbols. The setpoint for the topographies as well as the spectroscopy setpoint was -1 V, 100 pA. Within the energy interval where type 1 spectra exhibit a spectral gap (marked by the solid (300 K) and dashed (80 K) grey lines), the type 3  $dI/dV$  has a linear course vs. the voltage, manifesting in a V-shape with the minimum at the Fermi level. At the minimum, the  $dI/dV$  value reaches the resolution limit of the measurement. The  $dI/dV$  curves deviate from the V-shape (black arrows) at -0.4 V and 0.45 V for 300 K and -0.65 V and 0.55 V at 80 K. The energetic positions of these changes from the V-shape resemble the energetic positions of the onsets of spectral weight in type 1 spectra. d), e) Sketch of the proposed band dispersion behind the spectra shown in b) for charge carriers with a direction independent group velocity. Presuming the in-gap states to be a feature of the two-dimensional surface, the spectral results imply the existence of a Dirac-cone in the band gap region. Presuming the in-gap states to be a feature of the three-dimensional bulk, the spectral results imply a  $E(k) \propto k^{3/2}$  dispersion relation. f) Schematic density of states corresponding to the V-shaped  $dI/dV$ .

As assumed in chapter 5.5.4, the  $dI/dV$  in tunnelling spectroscopy is proportional to the sample's density of states. Considering the situation of tip-dependent addressability of states, this statement is modified to: measured  $dI/dV$  in tunnelling spectroscopy on  $\text{Na}_2\text{IrO}_3$  is proportional to the addressed sample's density of states. Even though the absolute values are difficult to interpret, the shape of the  $dI/dV$  curve reveals deeper physical insights. According to equation 5.9, i.e.  $dI/dV \propto D_{\text{Sample}}$ , the linear in-gap  $dI/dV$  for type 3 spectra translates to an also linear course of the related sample density of states  $D_{\text{Sample}}$  versus the energy. It is important to note, that the observation of type 3 spectra is done on clean  $\text{Na}_2\text{IrO}_3$  surfaces and

is not an exclusive feature of structures like point defects or step edges. The underlying density of states (DOS) is therefore either a feature of the very surface or the whole crystal. The first case implies a 2D density of states, the second case a 3D-DOS. Under the restriction that the group velocity of the charge carriers is independent from the spatial direction, it is possible to relate the V-shape in type 3 spectra to band dispersion characteristics. The relation between the density of states  $D(E)$  and the dispersion relation  $E(\mathbf{k})$  has the proportionality [90], [92]:

$$D(E) \propto \int_{E(\vec{k})=\text{const.}} \frac{dS_E}{|\nabla_{\mathbf{k}}E(\vec{k})|}, \quad 6.2$$

with the surface element  $dS_E$  of the surface of constant energy  $E(\vec{k}) = E$  and  $\nabla_{\mathbf{k}}E(\vec{k}) = dE(\vec{k})/dk_{\perp}$ , where  $dk_{\perp}$  is perpendicular to  $dS_E$ . Using:

$$\frac{dI}{dV}(V) \propto \frac{dI}{dV}(E) \propto E \propto D_{\text{Sample}}(E) \quad 6.3$$

and the finding of the linearity in type 3 spectra

$$\int_{E(\vec{k})=\text{const.}} \frac{dS_E}{|\nabla_{\mathbf{k}}E(\vec{k})|} \propto E \quad 6.4$$

the proportionality in equation 6.2 can be simplified to:

$$D(E) \propto \left(\frac{\partial E}{\partial k}\right)^{-1} \cdot k^{(d-1)} \propto E, \quad 6.5$$

with the wavevector  $k$  and the dimensionality  $d = \{2,3\}$ . In two dimensions, the proportionality 6.5 is fulfilled for  $E(k) \propto k$ , i.e. a Dirac cone similar to the case of graphene. For a three-dimensional system, the proportionality 6.5 is fulfilled for  $E(k) \propto k^{3/2}$ . The according models are sketched in Figure 6.16 d) - f).

It is tempting to assign the band gap closing via a Dirac-cone to the bulk boundary correspondence for a topologically insulating  $\text{Na}_2\text{IrO}_3$ . However, this is not the only possible reasoning for the emergence a linear  $dI/dV$ . Therefore, a brief discussion on the possible physical origins of type 3 spectra will be given in the following.

### Scenario 1: The V-shaped $dI/dV$ corresponds to a Coulomb gap.

The premise for this scenario is two-fold. Firstly, it is presumed that the states underlying the V-shaped  $dI/dV$  are localized and mediate variable hopping conductance. This is in accordance with transport investigations showing that the electric conductance in  $\text{Na}_2\text{IrO}_3$  is variable range hopping mediated below room temperature (see chapter 4.1). Secondly, it is assumed that the inter-site electron-electron correlation is significant for these states.

As introduced in chapter 5.7.4, the emergence of a pseudo gap referred to as the Coulomb gap is the result of such correlation effects, modifying the variable range hopping ansatz. In the theoretical description of VRH, it is assumed that the relevant energy interval around the Fermi level  $E_F$  in which hopping takes place is rather narrow, yielding the simplification to a constant density of states around  $E_F$ . It was argued in chapter 5.7.4, that correlation effects enforce the emergence of a Coulomb gap around  $E_F$  with a DOS of the form

$$N(E) \propto N_0 |E - E_F|^n, \quad n = 1 \quad \text{in 2D} \quad , \quad n = 2 \quad \text{in 3D.} \quad 6.6$$

Hence, a linear (V-shaped) DOS in the vicinity of the Fermi energy resembles a Coulomb gap in a two-dimensional system. However, it needs to be kept in mind that the opening of a Coulomb gap is usually observed at low temperatures, which in-turn corresponds to small gap sizes. This would render the emergence of a Coulomb gap as underlying phenomenon in type 3 spectra to be highly unusual, as the V-shape persists at least up to 300 K. The macroscopic electrical resistance of materials exhibiting a Coulomb gap has a characteristic temperature dependence of  $\ln(R(T)) \propto 1/T^{1/2}$ , independent from the systems dimensionality (see chapter 5.7.4). Hence, it is instructive to discuss the transport results from chapter 7 before concluding on the role of inter-site correlation in the context of type 3 spectra.

### Scenario 2: Proximity to the Hubbard Metal-Insulator transition

It was recently reported for  $\text{Na}_2\text{IrO}_3$  and other  $j_{\text{eff}}=1/2$  systems like  $\text{Sr}_3(\text{Ir}_{1-x}\text{Ru}_x)_2\text{O}_7$  and  $(\text{Sr}_{1-x}\text{La}_x)_2\text{IrO}_4$  that disorder and doping can result in the narrowing or even closing of the Mott gap [26], [122], [123]. According STM/STS datasets taken on  $\text{Sr}_3(\text{Ir}_{1-x}\text{Ru}_x)_2\text{O}_7$  and  $(\text{Sr}_{1-x}\text{La}_x)_2\text{IrO}_4$  are shown in Figure 6.17.

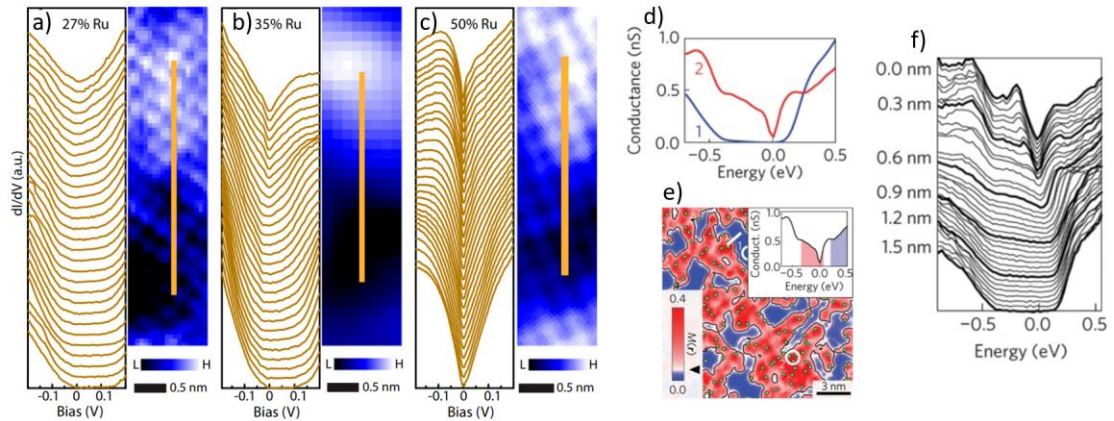


Figure 6.17 Closing of the Mott gap in  $(\text{Sr}_{1-x}\text{La}_x)_2\text{IrO}_4$  and  $\text{Sr}_3(\text{Ir}_{1-x}\text{Ru}_x)_2\text{O}_7$  due to doping and disorder, respectively. a)-c)  $dI/dV$  line cuts along the lines on the respective topography on the right sides measured on the  $\text{Sr}_3(\text{Ir}_{1-x}\text{Ru}_x)_2\text{O}_7$ -surface [122]. The doping level was reported to correlate with the topographic height. Hence, the colour scale in the topographies represents the local variations of doping induced by the substitution of iridium with ruthenium, where white represents high and black represents low doping. At 50% ruthenium substitution, all  $dI/dV$  spectra show a V-shaped Mott gap closing. For less substitutions, the local doping strength determines the form of the  $dI/dV$  spectrum. At low doping (a), an open Mott gap is observed that closes gradually with increasing local doping until the gap is again closed in a V-shaped fashion (b), c). Reprinted from [122]. d)-f). Closing of the Mott gap in  $(\text{Sr}_{1-x}\text{La}_x)_2\text{IrO}_4$  due to disorder [123]. Both, a Mott gap as well as a closed gap with a V-shaped characteristic around the Fermi level can be observed, d). e) Colour coded STM-topography according to the colours in d). Red areas predominantly have closed gaps, blue areas exhibit Mott gaps. f)  $dI/dV$  spectra along the white line in e), showing the gradual transition between V-shaped gap closing and a Mott gap upon moving between areas with high and low disorder. Reprinted from [123].

It was shown that the closing of the Mott gap in these materials gradually correlates with the degree of doping or defect density, where it is the actual Hubbard band edges that move closer to the Fermi level. The closing of the Mott gap occurs with a “V-shaped”  $dI/dV$  characteristic. This V-shape is similar to the characteristic of the in-gap  $dI/dV$  of type 3 spectra in  $\text{Na}_2\text{IrO}_3$ . Published work on a similar impact of disorder for  $\text{Na}_2\text{IrO}_3$  does not exist to the best knowledge of the author. However, work on the effect of doping at the  $\text{Na}_2\text{IrO}_3$  surface was performed [26]. It was argued that doping of the topmost iridate layer is dependent on the surface termination. For the Na-termination ((1x1)-reconstruction), each surface Na atom donates one electron. This electron donation is absent in the case of an iridate termination. It was proposed that this difference in electron donation results in a smaller Mott gap of  $\sim 0.4$  eV at the Na-terminated ((1x1)-reconstructed) surface compared to the iridate terminated surface with a Mott gap of  $\sim 1.0$  eV.

There are two arguments against a V-shaped Mott gap closing due to the proximity to an insulator-metal transition for  $\text{Na}_2\text{IrO}_3$ . The first argument arises from the prior results on the termination dependent doping effect in  $\text{Na}_2\text{IrO}_3$  mentioned earlier [26]. The according work used spatially resolved ARPES as well as evaporation of potassium



onto the cleaved  $\text{Na}_2\text{IrO}_3$  surface to study the effect of doping, observing a gradual change of the size of the measured Mott gap. Considering that the  $\text{Na}_2\text{IrO}_3$  bulk is robustly Mott insulating, the reported doping effect would go into the wrong direction for the data presented in this thesis. A Na-terminated surface results in electron doping of the underlying iridium layer that is close to the doping of an iridate layer deep in the bulk. In contrast, the iridate layer on top of an iridate terminated surface experiences less electron doping since a complete adjacent sodium layer is missing. Now, the work [26] reported an increased Mott gap size for the iridate termination, not a decreased one. In all the STM/STS-measurements presented in this thesis, the maximum Na-surface content is the one of the (1x1)-reconstruction where 2/3 of the surface Na is missing compared to bulk Na-layers. Hence, if anything, the Mott gap observed by means of STS should be equal or larger compared to the bulk Mott gap. This might be an interesting ansatz to explain the spectral gap size of 0.8 eV at 300 K measured in type 1 spectra, being larger than reported Mott gap values, but cannot explain the existence of type 3 spectra.

Independent of this, the second argument against a V-shaped gap closing in the proximity of a Mott insulator-metal transition is much simpler. No gradual transition between type 1, type 2 and type 3 spectra upon moving across the sample surface could be related to local structures, e.g. defects. Even though there is an impact of the local surface structure on the addressability of the different spectral types, no clear correlation to a spatially dependent gradual change of  $dI/dV$  data was found. This either means that type 3 spectra cannot be explained in an insulator-metal transition framework or that the proximity to the transition is constant throughout the surface. The latter point is unrealistic considering the high defect density and variation on the  $\text{Na}_2\text{IrO}_3$  surface that introduces both, local disorder and doping.

Consequently, a doping or disorder induced Mott insulator-metal transition is not adequate to describe the emergence of type 3 spectra in the context of the surface morphology and the simultaneous existence of type 1 and type 2 spectra.

### Scenario 3: Non-trivial Topology

As described in chapter 3.2, non-trivial topology was proposed for  $\text{Na}_2\text{IrO}_3$  in a weak 3D sense, where individual layers of the crystal structure form 2D TIs with conductive edge channels, i.e. quantum-spin-Hall systems. However, the prospect of a strong 3D-TI characteristic was also theoretically considered, even though it was argued that this would require an increase of the inter-layer distance of ~30% (chapter 3.3).

The type 3 in-gap spectral weight is observed at clean surfaces and not exclusively found at step edges. Thus, presuming that the V-shaped  $dI/dV$  emerges from topologically protected boundary states, the underlying topology would be of strong 3D-TI type. The bulk-boundary correspondence of a strong 3D-TI, i.e. the in-gap states at the boundary to a topologically trivial material, is realized by the emergence of a Dirac-cone. Here, the vacuum serves as topologically trivial medium [124] at the boundary, i.e. the  $\text{Na}_2\text{IrO}_3$  sample surface. This is fitting to the measured linear in-gap  $dI/dV$  of type 3 spectra for a 2D system. Topologically protected surface states do not depend on the surface structure. Hence, this scenario implies that type 3 spectra must also be apparent on the iridate terminated,  $(\sqrt{3}\times\sqrt{3})\text{R}30^\circ$ -reconstructed surface. Successful STM/STS-measurements on the  $(\sqrt{3}\times\sqrt{3})\text{R}30^\circ$ -reconstructed surface are scarce and the identification of this reconstruction usually requires adjacent  $(1\times 1)$ -reconstructed terraces, as the  $(\sqrt{3}\times\sqrt{3})\text{R}30^\circ$ -reconstructed surface is commonly densely populated with defects. Such a rare dataset is depicted in Figure 6.18.

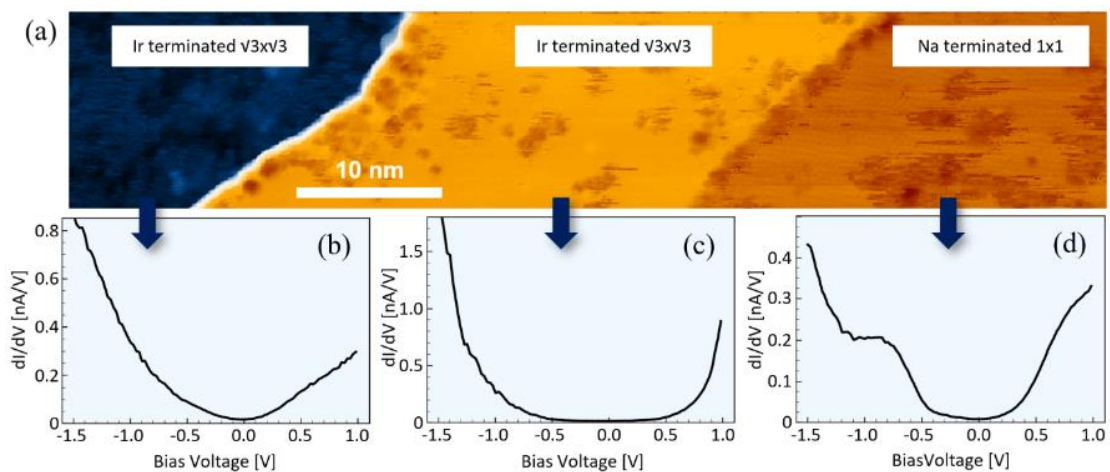


Figure 6.18 Simultaneous observation of an open spectral gap as well as a V-shaped gap closing for the  $(\sqrt{3}\times\sqrt{3})\text{R}30^\circ$ -reconstructed surface at 300 K. (a) Constant current topography map covering one  $(1\times 1)$ -terrace and two  $(\sqrt{3}\times\sqrt{3})\text{R}30^\circ$ -terraces, recorded using a setpoint of -1.5 V and 100 pA. (b)-(d)  $dI/dV$  curves taken at the terraces indicated by blue arrows. (b) Shows a type 3 V-shaped gap closing on the  $(\sqrt{3}\times\sqrt{3})\text{R}30^\circ$ -reconstructed surface. (c) Shows a type 1 spectral gap on the  $(\sqrt{3}\times\sqrt{3})\text{R}30^\circ$ -reconstructed surface. (d) Shows a combination of type 1 and type 3 spectra on the  $(1\times 1)$ -reconstructed surface.

One  $(1\times 1)$ -reconstructed and two  $(\sqrt{3}\times\sqrt{3})\text{R}30^\circ$ -reconstructed surfaces are depicted in Figure 6.18 a). Spectra taken on the respective free surface are shown in Figure 6.18 b) to d). As can be seen, both, type 1 and type 3 spectra were found on the  $(\sqrt{3}\times\sqrt{3})\text{R}30^\circ$ -reconstructed surface, confirming that the in-gap spectral weight with a linear  $dI/dV$  characteristic can be found on both terminations of the  $\text{Na}_2\text{IrO}_3$  surface.

The observation that the same tip shows deviating spectroscopic results at two adjacent terraces with the same termination is not unique for the  $(\sqrt{3}\times\sqrt{3})R30^\circ$ -reconstruction. This is discussed for the  $(1\times 1)$ -reconstruction in chapter 6.4.

Considering the known ARPES data on  $\text{Na}_2\text{IrO}_3$  surface, only one work reports in-gap states with a linear dispersion (chapter 3.1). Other ARPES works report a band gap with no in-gap states or no linear dispersion. Therefore, ARPES as the usual method to confirm surface states being related to topology fails to paint a clear picture. Another method to gain insights on potential topological behaviour is the search for quasiparticle interference, that requires an excellent signal to noise ratio in STM/STS measurements. To achieve this, employing measurements at low temperatures is mandatory. STM measurements at LHe temperature on  $\text{Na}_2\text{IrO}_3$  were successfully performed for the first time in the experimental work for this thesis (see chapter 6.5), but no hallmarks of quasiparticle interference could be observed. Measurements at 80 K did not show clear patterns in the STS-maps that could be related to any  $\vec{k}$ -dependencies of scattering by Fourier transforming such STS maps, independent of the considered energy. Quasiparticle interference measurements require an excellent signal to noise ratio. Hence it is possible that lower measurement temperatures than 80K are required to measure quasiparticle interference on the  $\text{Na}_2\text{IrO}_3$  surface.

From the three scenarios presented to approach the physical picture underlying type 3 spectra, scenario 2 can be directly discarded. Scenario 1 suggests a large coulomb gap of 0.8 eV that persists up to 300 K. This appears to be very unlikely but requires further investigation, e.g. via macroscopic transport measurements. This leaves non-trivial topology as the most likely picture among the scenarios presented here. It predicts the emergence of a highly conductive metallic surface channel that should be observable in macroscopic surface transport measurements, as the bulk conductance is hopping mediated and follows a different temperature dependence than metallic conductance.

Summary on the Type 3  $dI/dV$  Spectra:

- Type 3 spectra taken on both  $\text{Na}_2\text{IrO}_3$  surface terminations show in-gap states resembling a linear DOS vs energy.
- The in-gap states cannot be explained in the framework of a Mott-Hubbard insulator.
- The picture of  $\text{Na}_2\text{IrO}_3$  being a strong 3D-topological insulator fits to all characteristics of type 3 spectra.
- Published photoemission spectroscopy investigations are inconsistent and further ARPES work is required in the context of the emergence of type 3 spectra in  $\text{Na}_2\text{IrO}_3$ .

## 6.4 Robustness of the Surface In-Gap States

Since vacuum is topologically trivial, the surface of a strong 3D topologically non-trivial material in vacuum must exhibit in-gap states with a linear dispersion at the band crossing, i.e. the emergence of a Dirac-cone (chapter 3.2). These boundary states are not dependent on the surface properties and therefore robust against any alterations, like defects, non-magnetic impurities etc. For a strong 3D-TI, this also means that the boundary states are robust across extended defect structures like step edges. Presuming now that type 3 spectra are the hallmark of a topology related band gap closing at the surface via a Dirac-cone, step edges should not inhibit the emergence of type 3 spectra. A dataset probing the robustness of the type 3 spectrum is depicted in Figure 6.19.

Here, single  $dI/dV$ -spectra were taken across a step edge separating two (1x1)-reconstructed terraces, as shown in the inset of Figure 6.19 a). The spatial distance between single spectroscopy measurements is 1 nm. Starting on the upper terrace, spectra of type 3 with the V-shaped  $dI/dV$  are observable. Upon approaching the step edge, the overall conductance in the V-shape voltage-interval decreases but qualitatively persists, as shown in the zoom-in depicted in Figure 6.19 b). Hence, the spectral type 3 does not change across the step edge and the step edge itself does not add or inhibit any distinct spectral features. Instead, it acts only as a transition zone between the upper and the lower terrace. The higher overall conductance in vicinity of the Fermi level on the upper terrace may be an addressability related issue. It is under current investigation, why equivalent terraces (both (1x1)-reconstructed) exhibit different absolute in-gap  $dI/dV$  values for type 3 spectra. However, it is evident that type 3 spectra are robust across step edges, fitting to the ansatz that relates them to strong 3D topology induced surface in-gap states.

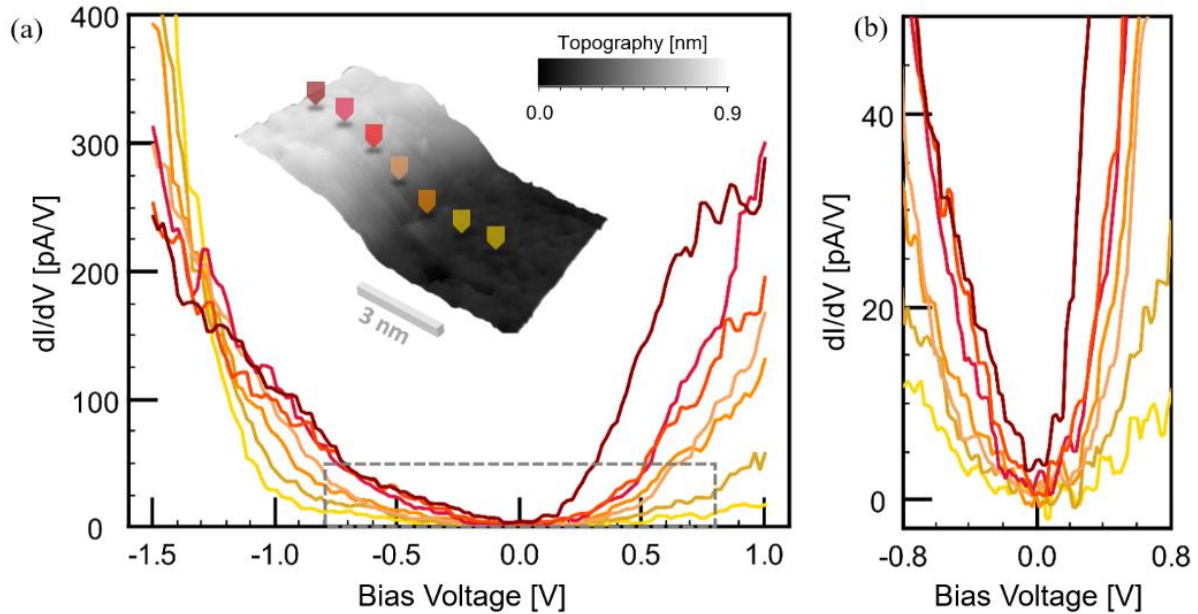


Figure 6.19 Influence of step edges on type 3 spectra. (a)  $dI/dV$  spectra recorded equidistantly across a single step on a  $(1 \times 1)$ -reconstructed surface. The lateral distance between the spectra is 1 nm. The recording positions are marked in the inset and colour coded according to the  $dI/dV$  curves. A smooth transition of the curves is observed when crossing the step edge, without a change in the qualitative shape of the spectra. However, the overall conductivity is altered. The deviation regarding the spectral weight onset at bias voltages lower than  $-0.8$  V is due to the fact that the integral of the  $dI/dV$  curves from the setpoint to the Fermi level has to be constant. (b) Zoom-in according to the dashed grey box in (a). The band gap closing resembles a V-shape on an energy scale of several hundred meV.

Summary on the robustness of type 3 spectra across step edges:

- Type 3 spectra are robust across step edges.
- The measured overall conductance varies between two adjacent terraces with the same reconstruction.

## 6.5 STM Measurements on $\text{Na}_2\text{IrO}_3$ at 8 K Using Optically Excited Charge Carriers

STM investigations require the probed material to be sufficiently conductive to establish a stationary tunnelling current. Transport in  $\text{Na}_2\text{IrO}_3$  was reported to be variable range hopping mediated at low temperatures, where the resistance exponentially increases upon cooling. At the minimum achievable temperature of 8 K, the  $\text{Na}_2\text{IrO}_3$  conductance is too low to establish sufficiently high currents through the sample between the tunnelling junction and the contacts attached to the sample. No tunnelling current could be established using the standard STM-

procedure at 8 K, causing immediate crashes of the tip into the sample, as the tip height adjustment is based on the distance-dependent tunnelling current.

An approach based on the works of P. Kloth [125], [126] was employed, where charge carriers are optically excited at the  $\text{Na}_2\text{IrO}_3$  surface to generate sufficient conductance for a stable tunnelling current. Figure 6.20 displays this approach schematically.

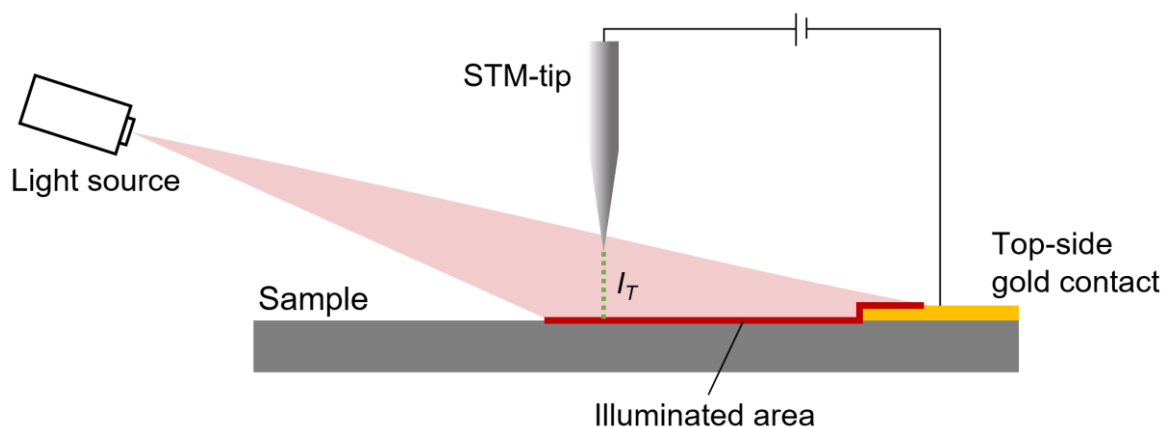


Figure 6.20 Scheme of the optical excitation assisted STM measurements on the  $\text{Na}_2\text{IrO}_3$  surface at 8 K. A laser with a wavelength of 785 nm and a power of 4.25 mW was used to simultaneously illuminate the STM tunnelling junction and the sample surface area between tunnelling junction and sample contact. The optical excitation of charge carriers introduces a sufficiently high conductance to establish a stable tunnelling current despite the sample being highly insulating.

In contrast to the STM measurements at 80 K and 300 K, electrical contacts were not only applied at the bottom of the sample but also on the top, following the same preparation procedure as used for macroscopic transport measurements (see chapter 5.3.2). After cleaving at room temperature in UHV, the residual top contacts border the freshly cleaved surface. With this, current passing through the tunnelling junction can flow in the crystallographic in-plane direction, where the resistivity is two to three orders of magnitude lower than in the out-of-plane direction (chapter 4.1). As this alone is not sufficient at 8 K, and since there is no other way to establish stable tunnelling, the next step is to illuminate the tunnelling junction as well as the sample surface between a surface contact and the tunnelling junction. For this, a laser with a wavelength of 785 nm at 4.25 mW was used. A detailed description of the technical laser setup for the STM is found in [125], [126]. The conductance induced by optical excitation is sufficient to carry small tunnelling currents between 10 pA and 50 pA at a setpoint voltage of 2 V. With this, for the first time STM measurements on  $\text{Na}_2\text{IrO}_3$  at 8 K were possible. A topography acquired with this setup is depicted in Figure 6.21.

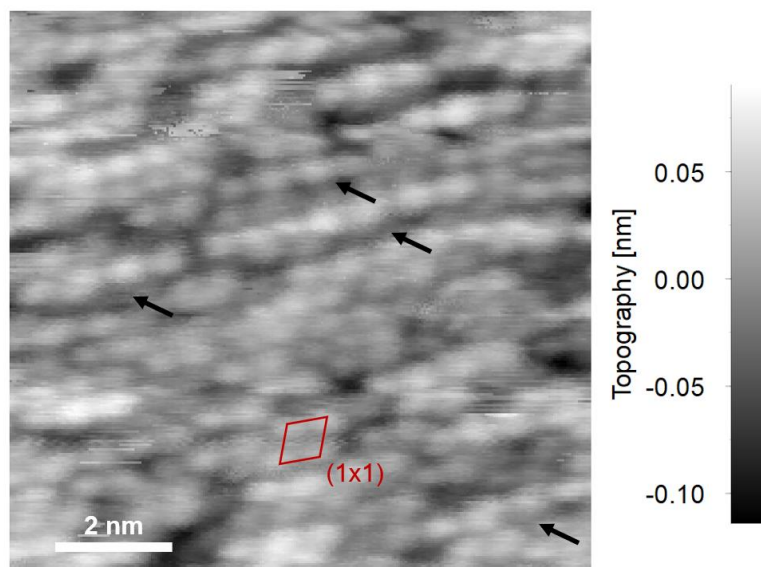


Figure 6.21 STM topography of the freshly cleaved  $\text{Na}_2\text{IrO}_3$  surface at 8 K. The setpoint parameters are 2 V and 10 pA. A quasi-hexagonal surface corrugation with an average feature-to-feature distance of  $0.6 \text{ nm} \pm 0.04 \text{ nm}$  is visible. This is in agreement with the structural parameters of the (1x1)-reconstructed  $\text{Na}_2\text{IrO}_3$  surface. Additionally, local chain-like rearrangements are found (black arrows) that are absent at higher temperatures.

The surface shows a quasi-hexagonal reconstruction with an average distance between neighbouring features of  $0.6 \text{ nm} \pm 0.04 \text{ nm}$ . This is in agreement with the known sodium terminated, (1x1)-reconstructed surface observed at higher temperatures. It is concluded that the corrugation in Figure 6.21 arises from surface sodium atoms. Additionally, local rearrangements of sodium atoms into short, chain-like structures are observed (black arrows, Figure 6.21). These short chains are not seen at 80 K or 300 K and their origin is yet an open issue.

Next to topographic data, first spectroscopic investigations were done at 8 K. In contrast to the findings at higher temperatures, only one type of spectrum was found regardless of local surface structures or the STM tip. Such a  $dI/dV$  spectrum is depicted in Figure 6.22. The initial setpoint was 2 V at 50 pA. Between -2 V and 1.5 V, the  $dI/dV$  is V-shaped, showing similarity to type 3 spectra. Upon approaching the initial setpoint and above 1.5V, the  $dI/dV$  curve deviates from the linear course and decreases sharply close to 2 V. The minimum of the spectrum is found in the vicinity of the Fermi level.



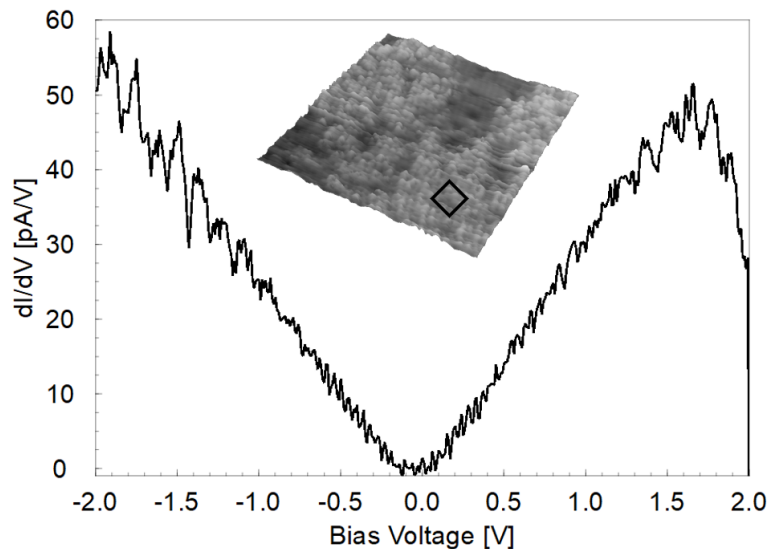


Figure 6.22  $dI/dV$  spectrum taken on the (1x1)-reconstructed  $\text{Na}_2\text{IrO}_3$  surface at 8 K. The position on the surface is marked in black in the topography. The initial setpoint was 2 V at 50 pA. Between -2 V and 1.5 V, the spectrum is V-shaped. This linear course deviates close to the setpoint.

As the STM/STS work on  $\text{Na}_2\text{IrO}_3$  at 8 K is at early stages, the origin of such spectra is yet under current investigation. However, from the similarities to type 3 spectra, it could be speculated that the spectrum in Figure 6.22 might have the same origin. At higher temperatures, the type 3 V-shape maintains the  $dI/dV$  linearity roughly within the type 1 spectral gap region. In turn, the size of the type 1 spectral gap increases with decreasing temperatures (0.8 eV at 300 K vs 1.2 eV at 80 K). If these phenomena – type 1 spectral gap and type 3 V-shape – are connected, and if the type 1 spectral weight gap size is drastically increased at 8 K, Figure 6.22 might show type 3 spectra. However, this is speculative at this point. Importantly though, no signature corresponding to type 1 or type 2 spectra is found at 8 K.

Summary on the STM/STS investigation of the  $\text{Na}_2\text{IrO}_3$  surface at 8 K:

- First successful STM/STS measurements on the freshly cleaved  $\text{Na}_2\text{IrO}_3$  surface at 8 K were performed using optical excitation of charge carriers.
- The (1x1)-reconstruction with local chain-like rearrangements of sodium was found.
- Tunnelling spectroscopy measurements show an extended V-shaped  $dI/dV$  and no signatures of type 1 or type 2 spectra.

## 7 Macroscopic Transport Measurements

The investigation of the freshly cleaved  $\text{Na}_2\text{IrO}_3$  surface by means of scanning tunnelling techniques revealed multiple electronic characteristics of the surface that were not reported in published works. From the discussion of these characteristics, it is clear that further experimental work using alternative methods is required to conclusively assign a model that underlies the found electronic characteristics. Transport measurements of the freshly cleaved surface can yield deeper insights. Such transport measurements were performed using the home-built setup described in chapter 5.6 and will be presented in the following. Previously published transport works on  $\text{Na}_2\text{IrO}_3$ , which focused on the bulk transport properties, are used as reference to the data from uncleaved samples.

In the context of this thesis, samples from three different synthetization batches were investigated for the transport characteristics of the  $\text{Na}_2\text{IrO}_3$  surface. Samples from two of the three batches showed that a conductive channel exists at the  $\text{Na}_2\text{IrO}_3$  surface, which is not hopping mediated in contrast to the bulk transport. Early results from the first batch are found in the bachelor thesis of S. Maamar [127]. The transport investigations presented here were done on a sample from the second synthetization batch, detailing the finding of a conductive surface channel. On-going investigations on the third batch show no enhanced surface conductance. This suggests that the occurrence of high  $\text{Na}_2\text{IrO}_3$  surface conductance critically depends on the peculiarities during the synthetization of the samples. This connection might also be a reason for the incoherence of the reports on the  $\text{Na}_2\text{IrO}_3$  electronic properties in literature (see chapters 2.3 and 3.4).

### 7.1 Electronic Transport of Uncleaved $\text{Na}_2\text{IrO}_3$

The experimental procedure was as follows:  $\text{Na}_2\text{IrO}_3$  samples contacted via four gold electrodes – two on the top and two on the bottom facet of the plate shaped crystal, see chapter 5.3.2 – were positioned in a sample stage within an UHV-environment. The stage was cooled using  $\text{LN}_2$  until thermal equilibrium is reached. Then, the  $\text{LN}_2$  was disposed and the stage with the sample heated up slowly towards room temperature. Upon warming up, voltage sweeps from -1 V to 1 V within 20 s were applied between two contacts on the same crystal facet while measuring the current. Between each voltage sweep, it was waited for 40 s, i.e. one I-V-curve was taken every minute. The differential resistance was calculated from the I-V-curves.

Generally, all presented data focus on the in-plane transport, since this is the comparative measure for the surface related transport, as the cleaving plane is parallel to the crystal layers.

A transport dataset for an uncleaved  $\text{Na}_2\text{IrO}_3$  crystal is depicted in Figure 7.1. The overall geometry is shown in Figure 7.1 a). The contacts on the top side of the crystal are referred to as A and B, forming the A-B channel. The spacing between these two contacts was 1 mm. As the cleaver is always glued to the samples top side, channel A-B of the uncleaved sample is the direct reference for the transport measurements on the freshly cleaved surface (chapter 7.3). The contacts on the bottom side of the crystal are referred to as C and D, forming the C-D channel. The C-D contact distance was also 1 mm.

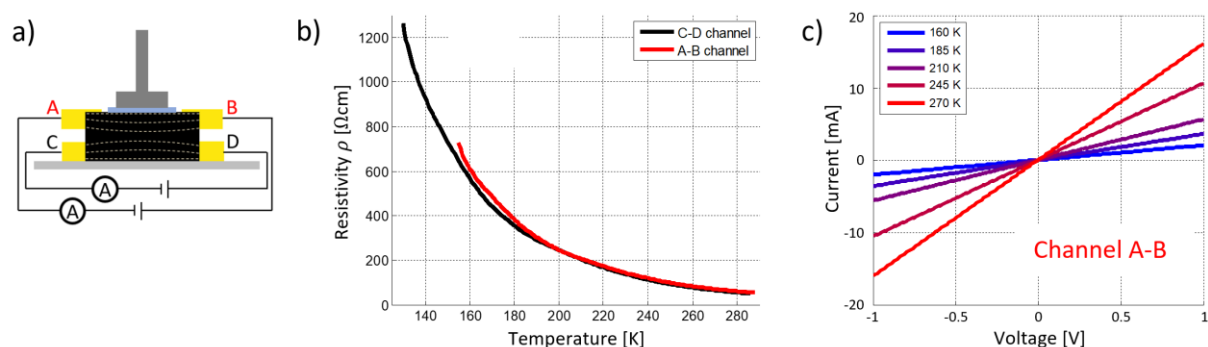


Figure 7.1 Electric transport measurements for uncleaved  $\text{Na}_2\text{IrO}_3$ . Two gold contact pairs from the channels A-B (top contacts) and C-D (bottom contacts), as sketched in a). b) Differential resistivity  $\rho$  at 0 V versus temperature for both channels, showing a monotonic decay of the resistivity with temperature. c) I-V characteristic from -1 V to 1 V for the A-B channel at different temperatures. The current rises linearly with the voltage, showing ohmic behaviour.

Figure 7.1 b) shows the differential resistivity at 0 V for both channels as calculated from the I-V curves. The  $\rho(T)$ -curves for the A-B and the C-D channel are nearly identical. The resistivity decays monotonically with rising temperature and is similar for both channels. At high temperatures, e.g. 286 K, the resistivity takes values of 56  $\Omega\text{cm}$  (A-B channel) and 50  $\Omega\text{cm}$  (C-D channel). At 155 K, the resistivity is higher by an order of magnitude, with 723  $\Omega\text{cm}$  for the A-B channel and 647  $\Omega\text{cm}$  for the C-D-channel. Such values are in agreement with published  $\text{Na}_2\text{IrO}_3$  bulk transport data for both, 155 K and 286 K [28], [63], and minor deviations can be attributed to different contact and sample geometries. Next, a selection of I-V-curves from -1 V to 1 V for the A-B channel for different temperatures is depicted in Figure 7.1 c). In all cases, the I-V curves show a nearly linear dependence on the voltage, with  $1.00 > \rho(1\text{ V})/\rho(0\text{ V}) > 0.97$ . This small decrease of resistivity with increasing voltage is attributed to Joule heating, thus the sample shows ohmic behaviour in electronic transport.

Recording the temperature during transport measurements as in Figure 7.1 is not trivial, since the sample itself is exposed to thermal radiation and the temperature is not measured directly

on the sample. To account for this, a temperature calibration procedure was used for all transport data, including the data in Figure 7.1. A thermocouple is positioned at the sample stage, measuring the temperature of the stage. Subsequent temperature investigations using an additional thermocouple attached to the samples top side (i.e. the A-B channel) showed, that the minimal temperature achieved with LN<sub>2</sub> cooling is 155 K - 160 K. Since the bottom side of the sample (i.e. the C-D-channel) is in direct contact to the substrate and not directly exposed to thermal radiation, a lower minimal temperature than ~155 K is expected. To further calibrate the temperature axes, resistance data of the uncleaved Na<sub>2</sub>IrO<sub>3</sub> crystal were compared to PPMS-data provided by the group of P. Gegenwart, Augsburg University. To account for varying sample and contact geometries, the ratio between the measured resistances and the respective resistance value at 282 K, i.e.  $R(T) \rightarrow R(T)/R(282 \text{ K})$ , was used for the data comparison. The best agreement was found for minimum temperatures of 155 K for the A-B channel and 130 K for the C-D-channel. The calibration of the temperature axes was done accordingly. Furthermore, the comparison to the PPMS-data was used to calibrate the differential resistance to a resistivity for better comparability among datasets. An exemplary comparison between the calibrated A-B-channel data from Figure 7.1 b) with PPMS data is depicted in Figure 7.2.

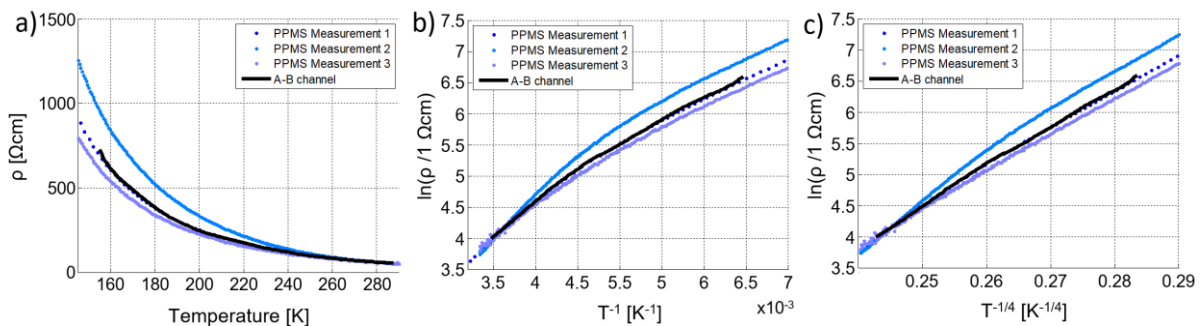


Figure 7.2 Comparison of measured and temperature calibrated Na<sub>2</sub>IrO<sub>3</sub> bulk transport data with three datasets taken with a PPMS at the group of P. Gegenwart, Augsburg University. The black curve represents the resistivity data from the A-B channel. The curves in shades of blue were taken on different Na<sub>2</sub>IrO<sub>3</sub> samples in a PPMS. All three plots show the same data but plotted with different scaling of the axes.

The three plots in Figure 7.2 depict the same data but with different scaling of the axes. a) shows  $\rho$  vs.  $T$  for comparison of the overall  $\rho(T)$ -course. b) shows  $\ln(\rho/1 \Omega\text{cm})$  vs.  $T^{-1}$  for comparison in the thermal excitation context that was shown to be the dominant conduction mechanism near and above room temperature. And c) shows  $\ln(\rho/1 \Omega\text{cm})$  vs.  $T^{-1/4}$  for comparison in the 3D-VRH context reported to be the dominant conduction mechanism at low

temperatures. The data show good agreement, with the only curve deviating significantly being also measured with a PPMS (PPMS Measurement 2).

As the resistivity measured for channels A-B and C-D yields similar results for the uncleaved  $\text{Na}_2\text{IrO}_3$  sample, it can be assumed that no significant difference - e.g. due to different contact qualities - between the measurements using channels A-B and C-D exists. Therefore, channel C-D might serve as reference after cleaving the crystal. Furthermore, the contact resistance can be neglected compared to the sample resistance, as the overall measured resistance is not higher than in PPMS measurements, and no contact induced non-ohmic characteristics are observed.

Next, the temperature dependence of the differential resistance is analysed in the context of the transport mechanisms proposed for  $\text{Na}_2\text{IrO}_3$  is done. It was reported that 3D variable range hopping is the dominant transport mechanism for  $\text{Na}_2\text{IrO}_3$  below room temperature. In chapter 5.7.3 it was shown that the temperature dependence of the resistivity for a d-dimensional VRH system is given by

$$\rho(T) \propto \rho_0 e^{\left(\frac{T_0}{T}\right)^{\frac{1}{d+1}}} . \quad 7.1$$

Close to and above room temperature, thermal excitation was reported to dominate the transport properties, with a temperature dependence of the resistivity characterized by

$$\rho(T) \propto \rho'_0 e^{\frac{E_g}{2k_B T}} . \quad 7.2$$

Plotting  $\ln(\rho(T))$  versus  $T^{-1}$  as well as  $T^{-1/(d+1)}$  and fitting a linear graph in the temperature regime of interest provides insight to the nature of the transport mechanisms. In the following, this is separately done for the data below 210 K and above 260 K, as the data suggest that the transport mechanism changes between these two temperatures. Following the conduction mechanisms proposed in literature, the data will be investigated for 3D-VRH as well as for conduction from thermally excited charge carriers. Additionally, the data will be examined for 2D-VRH behaviour as well as Efros-Shklovskii Hopping (ESH). The characteristic temperature dependence of the resistivity for ESH mediated transport was shown to be:

$$\rho(T) \propto \rho_0 e^{\left(\frac{T_{ES}}{T}\right)^{\frac{1}{2}}} , \quad 7.3$$

with  $T_{ES} = \beta e^2 / \kappa \alpha$  (chapter 5.7.4).

The analysis for temperatures below 210 K is presented in Figure 7.3, using the resistivity data at 0 V from the A-B-channel. Here, all plots in Figure 7.3 show the same data but are plotted with different temperature scaling.

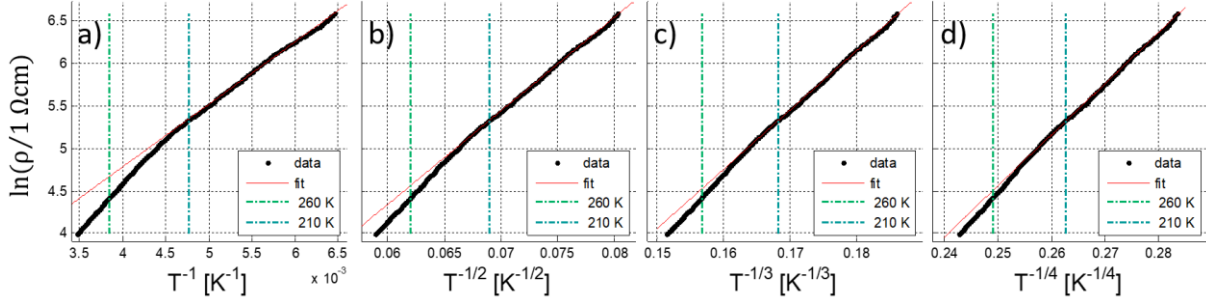


Figure 7.3 In-plane resistivity versus temperature for the A-B channel of an uncleaved  $\text{Na}_2\text{IrO}_3$  crystal measured with a contact-contact distance of 1 mm at 0 V. All plots show the same data. All curves were fitted with a linear function below 210 K (dashed blue line). The temperature axes are scaled according to the investigated transport mechanism: a) thermal excitation of charge carriers, b) ESH, c) 2D-VRH, d) 3D-VRH.

The  $\rho$ -scale is logarithmic in all plots, the temperature is scaled via: a)  $T^{-1}$  (thermal excitation of charge carriers), b)  $T^{-1/2}$  (ESH), c)  $T^{-1/3}$  (2D-VRH), and d)  $T^{-1/4}$  (3D-VRH) to account for two and three dimensional variable range hopping (equation 7.1), the thermal excitation ansatz (equation 7.2) and Efros-Shklovskii hopping 7.3. From a visual inspection, it is not clear which of the linear fits in Figure 7.3 is best suited to describe the course of the measured data. The fitted values for  $T_0$ ,  $T_{\text{ES}}$  and  $E_g/2k_B$  as well as the fitting errors are shown in Table 7.1.

Table 7.1 Values of  $T_0$  as well as the absolute error and the root mean squared error per datapoint extracted the linear fits between 155 K and 210 K in Figure 7.3.

Model	Characteristic Parameters	RMSE
3D VRH   Figure 7.3 d)	$T_0 = 1.304 \cdot 10^7 \text{K} \pm 0.019 \cdot 10^7 \text{K}$	$6.3 \cdot 10^{-3}$
2D VRH   Figure 7.3 c)	$T_0 = 3.351 \cdot 10^5 \text{K} \pm 0.038 \cdot 10^5 \text{K}$	$6.4 \cdot 10^{-3}$
ESH   Figure 7.3 b)	$T_{\text{ES}} = 1.210 \cdot 10^4 \text{K} \pm 0.011 \cdot 10^4 \text{K}$	$7.2 \cdot 10^{-3}$
Thermal excitation   Figure 7.3 a)	$E_g/2k_B = 735.6 \text{K} \pm 4.6 \text{K}$	$1.05 \cdot 10^{-2}$

The root mean squared errors per data point (RMSE) from the linear fits in Figure 7.3 a)-d) are all rather similar. Hence, also an analysis of the fitting errors for the presented data does not provide a clear picture regarding the conduction mechanism in  $\text{Na}_2\text{IrO}_3$  at low temperatures. This shows, that next to the attribution to 3D variable range hopping (see chapter 4.1), other transport mechanisms or 2D-VRH might be worth considering for the in-plane transport in  $\text{Na}_2\text{IrO}_3$ . Regarding the absolute value of  $T_0$ , the result of  $T_0 = 1.304 \cdot 10^7 \text{K} \pm 0.019 \cdot 10^7 \text{K}$  for

the 3D-VRH fit is close to the results from previous works, where values between  $T_0 \approx 10^6\text{K}$  [37] and  $T_0 \approx 10^7\text{K}$  [63] were reported.

The same analysis is shown in Figure 7.4 for temperatures above 260 K.

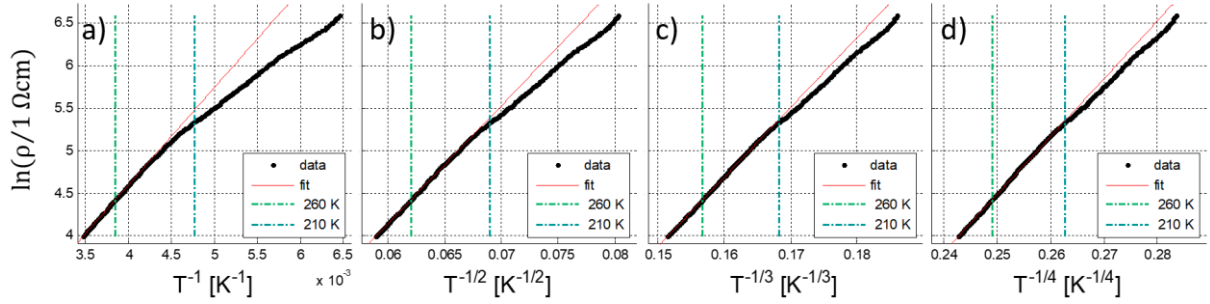


Figure 7.4 In-plane resistivity versus temperature for the A-B channel of an uncleaved  $\text{Na}_2\text{IrO}_3$  crystal measured with a contact-contact distance of 1 mm at 0 V. All plots show the same data. All curves were fitted with a linear function above 260 K (dashed green line). The temperature axes are scaled according to the investigated transport mechanism: a) thermal excitation of charge carriers, b) ESH, c) 2D-VRH, d) 3D-VRH.

Again, a visual inspection of the fitted curves does not yield a conclusive picture. Hence, the values for  $T_0$ ,  $T_{\text{ES}}$  and  $E_g/2k_B$  as well as the fitting errors are shown in Table 7.2.

Table 7.2 Values of  $T_0$  as well as the absolute error and the root mean squared error per datapoint extracted from the linear fits above 260 K in Figure 7.4.

Model	Characteristic Parameters	RMSE
3D VRH   Figure 7.4 d)	$T_0 = 2.152 \cdot 10^7\text{K} \pm 0.02 \cdot 10^7\text{K}$	$8.8 \cdot 10^{-4}$
2D VRH   Figure 7.4 c)	$T_0 = 5.421 \cdot 10^5\text{K} \pm 0.036 \cdot 10^5\text{K}$	$8.4 \cdot 10^{-4}$
ESH   Figure 7.4 b)	$T_{\text{ES}} = 1.918 \cdot 10^4\text{K} \pm 0.00832 \cdot 10^4\text{K}$	$7.7 \cdot 10^{-4}$
Thermal excitation   Figure 7.4 a)	$E_g/2k_B = 1146\text{K} \pm 2\text{K}$	$6.7 \cdot 10^{-4}$

Similar to the analysis below 210 K, the RSME per datapoint is rather small and none of the conduction mechanisms reproduces the data significantly better than the others. Assuming the underlying effect is conduction of thermally excited charge carriers as proposed in literature, the band gap can be calculated from  $E_g/2k_B = 1146\text{K}$  to  $E_g \approx 198\text{meV}$ . This value is lower than the previously reported Mott gap (minimum: 340 meV).

The following discussion proposes alternative models to the suggested models from literature for low temperature and above room temperature. The discussion of the ESH picture is covered in chapter 7.2 in the context of the STM/STS results. It is important to note, that the measured (in-plane) transport data are in agreement with previous works and in the following



only an alternative interpretation is proposed. Hence, the aim is not to invalidate the established picture, but to provide new perspectives for the interpretation of the  $\text{Na}_2\text{IrO}_3$  transport data, initiated by the finding that the transport data can be fitted equally well with different models (Table 7.1 and Table 7.2).

#### Model: $\text{Na}_2\text{IrO}_3$ Transport below 210 K is 2D-VRH mediated

Since the first published work on transport in  $\text{Na}_2\text{IrO}_3$  by Singh et al. from 2010 [28], it was accepted that the conductance of  $\text{Na}_2\text{IrO}_3$  is 3D-VRH mediated below room temperature ([30], [37], [62]–[64]). Manni et al. [63] showed, that the  $\text{Na}_2\text{IrO}_3$  in-plane conductance is higher by two to three orders of magnitude than the out-of-plane conductance, see Figure 4.1 e) in chapter 4.1. For the in-plane conductance, no anisotropy between the crystallographic a and b directions was reported.

An issue in this context is the yet unanswered question: which states mediate the VRH conductance in  $\text{Na}_2\text{IrO}_3$ ? Most works denote this to defects hosting localized states with energies in vicinity of the Fermi level [63], [64], without specifying what kind of defects exactly mediate the VRH. Other works argue that the Hubbard bands extend to the Fermi level, providing a non-zero DOS at  $E_F$ , hosting the VRH conductance [37]. In any case, to result in VRH conduction, the mediating states must be Anderson-type localized.

In a 2D-system, any disorder from the lattice periodicity leads to Anderson-type localization of the involved states, where in a 3D-system the localization depends on the degree of disorder. Hence, presuming that the VRH in  $\text{Na}_2\text{IrO}_3$  is mediated by states influenced by disorder, a restriction to two dimensions would enforce Anderson-type localization of the states. Consequently, all such states with the energy in the vicinity of the Fermi level could contribute to the macroscopically observed hopping conductance below 210 K. The  $\text{Na}_2\text{IrO}_3$  conductance anisotropy found by Manni et al. (chapter 4.1) matches the anisotropy from the layer structure of the crystal. Therefore, the natural assumption is that the crystalline layer structure affects the dimensionality of the hopping system. Identifying the iridate layers as 2D-systems, defect induced disorder could localize the iridium 5d states. Here, the Hubbard bands are in the vicinity of the Fermi level. Therefore, localized states in the Hubbard bands close to the Fermi level would mediate 2D-VRH conduction in this picture.

With the experimental methods used in this thesis, the dimensionality of the hopping system cannot be determined directly. However, the data from Figure 7.3 and Table 7.1 show that both, 2D- and 3D-VRH fit equally well to the  $R(T)$  data below 210 K.

Therefore, for the in-plane conductance of  $\text{Na}_2\text{IrO}_3$  that is probed in the transport investigation in this thesis, the 2D-VRH model is at least equally suitable to analyse the data as the 3D-VRH model, considering the discussion above.

#### Model: $\text{Na}_2\text{IrO}_3$ Transport above 260 K is Nearest Neighbour Hopping Mediated

For high temperatures, i.e. close to and above room temperature, conductance of thermally excited charge carriers is the reported transport model for  $\text{Na}_2\text{IrO}_3$  in the literature [30], [63]. The data analysis shown in Figure 7.4, leading to the results in Table 7.2 suggests that a VRH ansatz fits the  $\rho(T)$  data above 260 K equally well. It can be seen from Table 7.1 and Table 7.2, that the extracted value of  $T_0$  below 210 K is roughly half the value of  $T_0$  above 260 K. In chapter 5.7.3,  $T_0$  is shown to be defined as  $T_0 = c \cdot (k_B \alpha^d D_{\text{EF}})^{-1}$ , with the localization length  $\alpha$ , the density of states at the Fermi level  $D_{\text{EF}}$  and a numerical constant  $c$ . As none of these parameters is temperature dependent, also  $T_0$  must be temperature independent. Hence, if the transport in  $\text{Na}_2\text{IrO}_3$  below 210 K is correctly described by VRH, the transport above 260 K cannot be VRH mediated.

This leaves the conduction from thermally excited charge carriers as possible mechanism underlying transport above 260 K. Within this picture, electrons are thermally excited from the LHB to the UHB, leaving holes in the LHB. The temperature dependence of the overall conductance is then approximately proportional to the number of excited carries, resulting in  $\sigma = \exp(-E_{\text{Mott}}/2k_B T)$ , with  $E_{\text{Mott}}$  being the Mott gap. However, from the data in Figure 7.4 d), an energy gap of  $\approx 198$  meV was calculated, being significantly smaller than the smallest reported Mott gap size for  $\text{Na}_2\text{IrO}_3$  (340 meV). This discrepancy can occur due to two possible reasons: either both measurements probed the Mott gap but obtained different sizes of the gap, or the value of  $\approx 198$  meV extracted from the transport measurements does not represent the size of the Mott gap in  $\text{Na}_2\text{IrO}_3$ .

Considering the STS spectra of type 2 (chapter 6.3.2) showing an energy gap of 0.2 eV to 0.3 eV that might represent the  $\text{Na}_2\text{IrO}_3$  Mott gap, and the general inconsistent picture regarding the size of the Mott gap in literature (see chapter 2.3), it is possible that the thermal excitation ansatz is correct for transport in  $\text{Na}_2\text{IrO}_3$  close to and above room temperature, and that the reported Mott gap size of 340 meV is not a good benchmark for comparisons with the data from this thesis. To provide another perspective, the possibility that the here measured 198 meV gap does not represent the Mott gap will be explored in the following.

Hopping conductance does not vanish upon increasing temperatures. The question arises if the energy gap of  $E_g \approx 198$  meV is smaller than the reported Mott gaps due to conductance being provided by hopping concurrently to conductance from thermally excited charge carriers. Then, the conductance from thermally excited charge carriers gradually gains dominance over to overall conductance with increasing temperatures. Such a transition would result in an increase of the slope in the  $\ln(\rho(T))$  vs  $T^{-1}$  plot with increasing temperature. This is observed in the temperature region between 210 K and 260 K in Figure 7.4 a). Above 260 K, the slope stays approximately constant in the plot, and the energy gap extracted from the thermally excitation fit remains at 198 meV. Other datasets like in Figure 4.1 b) from chapter 4.1 suggest that the slope of  $\ln(\rho(T))$  vs  $T^{-1}$  still increases with the temperature above 300 K. Hence, the picture remains inconclusive, and the ansatz that conductance from thermally excited charge carriers dominates above room temperature cannot be discarded.

However, it is worth discussing another picture potentially suitable to explain the (in-plane-)  $R(T)$ -characteristic of  $\text{Na}_2\text{IrO}_3$  above 260 K. This is a transition from variable range hopping to nearest neighbour hopping between 210 K and 260 K. Here, the localized states mediating the hopping conductance remain unchanged but electrons occupying these states have enough thermal energy to overcome the energy difference to any other localized state in the hopping system. As the hopping probability decreases exponentially with the spatial distance between two localized states, hopping occurs predominantly to nearest neighbour states once sufficient thermal energy is provided. As introduced in chapter 5.7.3, nearest neighbour hopping (NNH) has with  $\rho \propto \exp(1/T)$  the same qualitative temperature dependence of the conductance as the conductance from thermally excited charge carriers. The energetic difference between hopping sites takes a minor role compared to the inter-site distance when  $\langle r \rangle / \alpha \gg \Delta E / k_B T$  is valid, with the average spatial inter-site distance  $\langle r \rangle$  and the average energetic inter-site difference  $\Delta E$ . Upon cooling, NNH transitions to VRH when  $\langle r \rangle / \alpha \approx \Delta E / k_B T$  is reached (see chapter 5.7.3), i.e. when  $\Delta E$  impacts the hopping resistance equally to  $\langle r \rangle$ . Hence, at the temperature where  $\Delta E$  for NNH, i.e.  $\Delta E_{\text{NNH}}$ , and  $\Delta E$  for VRH, i.e.  $\Delta E_{\text{VRH}}$ , are equal, an NNH-VRH transition could be expected.

From the fit in Figure 7.4 a),  $\Delta E_{\text{NNH}} \approx 99$  meV is obtained. For VRH, the extraction of  $\Delta E$  is slightly more complicated. Here, the  $R(T)$ -behaviour is determined by  $R = R_0 \exp(T_0/T)^{1/(d+1)}$ . The definition of  $T_0$  is dimensionality dependent, with  $T_{0,2D} = 13.8 / (k_B D_{\text{EF}} \alpha^2)$  and  $T_{0,3D} = 21.2 / (k_B D_{\text{EF}} \alpha^3)$  (see chapter 5.7.3). From equation 5.18 it is known that  $\Delta E^{d+1} = (k_B T)^d / (D(E_F) \alpha^d)$ . For 2D- and 3D-VRH this results in:

$$\Delta E_{2D} = \frac{k_B T_{0,2D}^{1/3}}{13.8^{1/3}} \cdot T^{2/3} \quad 7.4$$

and

$$\Delta E_{3D} = \frac{k_B T_{0,3D}^{1/4}}{21.2^{1/4}} \cdot T^{3/4} \quad 7.5$$

with the values for  $T_0$  from Table 7.1, this results in  $\Delta E$  vs  $T$  for NNH, 2D-VRH and 3D-VRH as plotted in Figure 7.5.

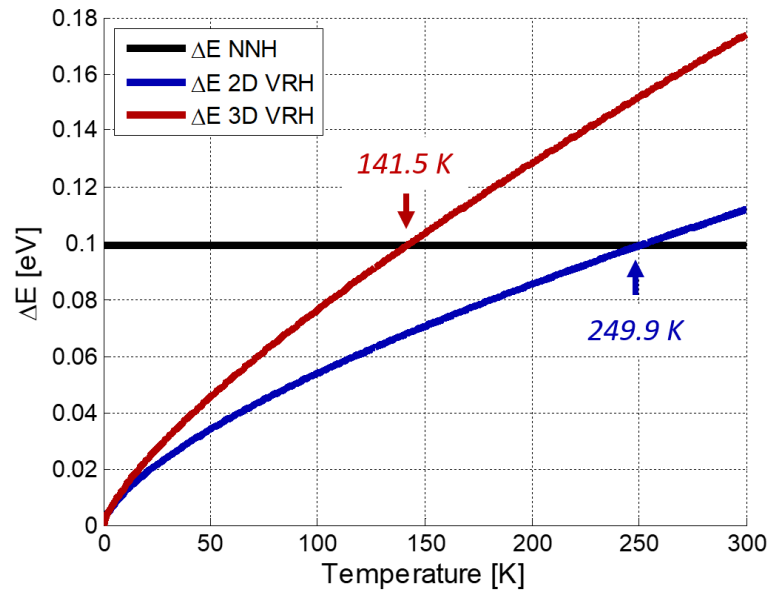


Figure 7.5 Temperature dependent activation energies for the  $\text{Na}_2\text{IrO}_3$  bulk conductance extracted from experimental transport data, considering different transport mechanisms. The blue curve represents the activation energy for 2D-VRH. The red curve represents the activation energy for 3D-VRH. The black curve represents the constant activation energy for NNH.

Here,  $\Delta E_{2D}$  and  $\Delta E_{\text{NNH}}$  intersect at 249.9 K. In the NNH-VRH-framework presented here, this means that below 249.9 K, the requirement for 2D-VRH is fulfilled and the system is expected to begin the transition from NNH to 2D-VRH mediated transport upon further cooling. In Figure 7.4, it is found that the bulk resistivity deviates from the  $\rho \propto \exp(1/T)$  behaviour below  $\sim 260$  K, being close to the value of 249.9 K. The intersection between  $\Delta E_{3D}$  and  $\Delta E_{\text{NNH}}$  occurs at 141.5 K. This is below the temperature regime covered by the presented transport data and does not fit to the experimental observation that the  $\text{Na}_2\text{IrO}_3$  transport characteristic changes just below 260 K.

In summary, a transition from NNH to 2D-VRH at  $\sim 250$  K upon cooling is consistent with the experimental  $\text{Na}_2\text{IrO}_3$  transport data in this thesis, providing an alternative

interpretation of the data for the full temperature range. However, it is important to note that the analysis done in Figure 7.5 is crucially dependent on the parameters extracted from the fits in Figure 7.3 and Figure 7.4. Hence, the picture in this model provides a contribution to scientific discussion for further works and does not make the thermal excitation ansatz from literature obsolete.

The presented pictures, i.e. 2D-VRH at low temperatures and NNH close to and above room temperature, model the  $\text{Na}_2\text{IrO}_3$  transport data equally well as the mechanisms proposed in literature. However, it is not intended to discard the accepted models but to provide an additional view on the transport data for of  $\text{Na}_2\text{IrO}_3$ .

Summary of the transport measurements on uncleaved  $\text{Na}_2\text{IrO}_3$ :

- Channels A-B and C-D show the same transport characteristics. Hence, channel C-D may serve as reference for transport investigations on cleaved  $\text{Na}_2\text{IrO}_3$ .
- It was found that 2D-VRH at low temperatures and nearest neighbour hopping at high temperatures model the transport data equally well as 3D-VRH and conduction from thermally excited charge carriers.

## 7.2 Discussion of the $\text{Na}_2\text{IrO}_3$ Bulk Electronic Properties in the Context of STM/STS and Transport Measurements

It was argued in chapter 7.1 that the  $\text{Na}_2\text{IrO}_3$  bulk conductance is variable range hopping mediated at low temperatures, and that the bulk conductance at high temperatures arises either from thermally excited charge carriers or from (nearest neighbour-) hopping (or both concurrently).

Another transport mechanism being considered is Efros-Shklovskii hopping conduction. As described in chapter 5.7.4, the temperature dependence of ESH conductance is  $\sigma \propto \exp(-1/T^{1/2})$ , regardless of the system's dimensionality. It was shown in chapter 7.1 that the description by such a  $\sigma(T)$  dependence is not worse than the other suggested mechanisms. In chapter 5.7.4, it detailed that a Coulomb gap is present in the ground state of systems where the transport is ESH mediated. The Coulomb gap is either V-shaped (2D system) or parabolic (3D system), with the minimum at the Fermi level. At this minimum, the density of states is

zero, i.e. the Coulomb gap is a pseudo gap. For 2D, this resembles the V-shaped course of type 3 spectra in the vicinity of the Fermi level  $E_F$ . For 3D, the  $dI/dV$  vs  $V$  of type 2 spectra in the vicinity of  $E_F$  might resemble a parabolic shape. Even though the transport data might fit to the Coulomb gap picture, the persistence of the V-shape in type 3 spectra and the spectral weight in the vicinity of  $E_F$  in type 2 spectra up to 300 K does not, since the emergence of considerable spectral weight at  $E_F$  and a vanishing of the Coulomb gap would be expected, which is not observed in the tunnelling spectroscopy measurements. This renders the Coulomb gap picture to be unlikely to model the experimental findings. Hence, the findings in this thesis are not attributed to ESH and the existence of a Coulomb gap in  $\text{Na}_2\text{IrO}_3$ .

In the following, the discussion focuses on what states mediate the bulk (variable range) hopping conductance in  $\text{Na}_2\text{IrO}_3$ , and which spectral type corresponds to these states. As there are no  $\text{Na}_2\text{IrO}_3$  energy bands other than the LHB and the UHB in the vicinity of the Fermi level, only localized states from the randomly distributed defects or disorder induced localization of LHB and UHB states are plausible mediators for the hopping conductance. In chapter 6.3.2, it was proposed that the peaks D and D\* found in type 2  $dI/dV$  spectra resemble the  $\text{Na}_2\text{IrO}_3$  Hubbard bands. This assignment is used in the following.

For the consideration of defect mediated transport that is independent from the  $\text{Na}_2\text{IrO}_3$  Hubbard bands, the assignment of type 2 spectra to the Hubbard bands leaves only the in-gap states in type 3 spectra to consider, since type 1 spectra show no spectral weight in the vicinity of the Fermi level. However, as defect states usually manifest as peaks in the DOS (chapter 5.7.2.2), the V-shaped in-gap  $dI/dV$  of type 3 spectra would be unconventional for defect states.

Hence, the picture of localized Hubbard band states mediating the bulk hopping transport is suggested here. For pristine  $\text{Na}_2\text{IrO}_3$ , the states in the Hubbard bands are not expected to be localized. However, it was introduced in chapter 6.3.2, that the D and D\* peaks in type 2 spectra exhibit tails reaching towards  $E_F$ . It is proposed that these tails emerge from heavy defect doping, inducing an energetic broadening of the Hubbard bands and potentially band tailing. The picture to this is shown in Figure 7.6.

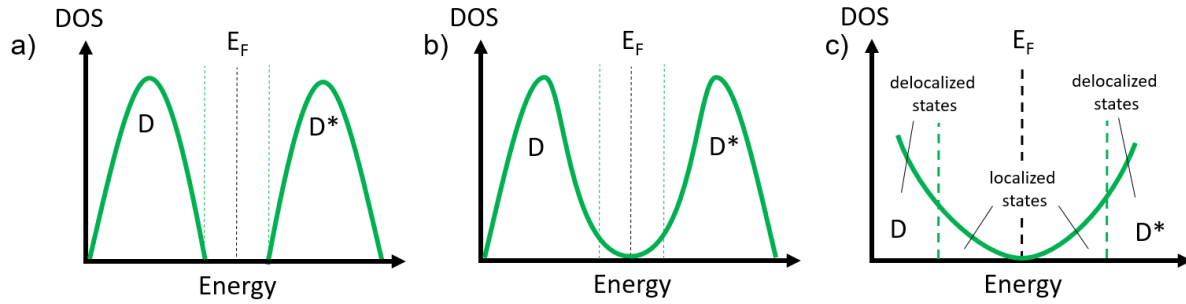


Figure 7.6 Model for band tailing due to heavy defect doping for type 2 spectra. a) Type 2  $dI/dV$  peaks D and  $D^*$  in the absence of defects. No band tailing is seen, and an open band gap is apparent. b) Type 2  $dI/dV$ -peaks D and  $D^*$  with heavy defect doping. The former band gap is bridged by band tails emerging from the defect states merging with the bands that underly the peaks D and  $D^*$ . The dashed green lines mark the former band edges. c) Zoom-in into b). The states close to the Fermi energy are localized. The localization length increases the closer the states are to the former band edges.

The hopping conduction would then be mediated via Anderson type localized states at the edges/tails of the LHB and the UHB close to  $E_F$ . At high temperatures, electrons could be thermally excited from the LHB to delocalized states of the UHB. Similarly, a transition from VRH to nearest neighbour hopping might occur with rising temperature (see chapter 7.1). In this case, thermal excitation is not required to explain the transport findings, as only the localized Hubbard band states close to  $E_F$  would be considered for transport. The model presented here fits to all experimental observations in this thesis and is also in accordance with the finding that in- and out-of-plane  $\text{Na}_2\text{IrO}_3$  bulk resistivity is different (chapter 4.1), as the LHB and UHB emerge from the  $\text{Ir } j_{\text{eff}}=1/2$  bands, that in turn correspond to Ir d-orbitals being located in the iridate layers, i.e. two-dimensional systems. With type 1 and type 2 spectra being attributed to the  $j_{\text{eff}}=3/2 - e_g$  energy gap and the Mott gap, respectively, the discrepancy between STS and ARPES/optical conductivity measurements in regard of the size of the Mott gap and its temperature dependence would be resolved. Furthermore, since the Hubbard band states emerge from only one orbital, i.e. the  $j_{\text{eff}}=1/2$  orbital, it can be argued that the tip dependent addressability of type 2 states is tied to the transfer matrix element corresponding to the  $j_{\text{eff}}=1/2$  orbital.

In summary, it is proposed that the  $\text{Na}_2\text{IrO}_3$  bulk transport is mediated by localized LHB and UHB states in the vicinity of the Fermi level, where the localization is induced by disorder from the high defect density.



### 7.3 Conductance of the Freshly Cleaved $\text{Na}_2\text{IrO}_3$ Surface

In the following, the transport characteristics of the freshly cleaved  $\text{Na}_2\text{IrO}_3$  surface are investigated and discussed. For this, the same setup as in chapter 7.1 was used to maintain comparability with the transport data of the uncleaved sample. The cleaver glued onto the top facet hosting the A and B contacts was used to cleave the sample to get a fresh surface in UHV (see chapter 5.4). Upon cleaving, parts of the gold contacts A and B were removed as these parts adhered on the cleaved-off piece of material. From this, the spacing between contacts A and B increased from 1 mm to 1.6 mm. The increased contact-contact distance is accounted for in the translation of the differential resistance into the resistivity values shown for the cleaved surface. Afterwards, temperature dependent transport measurements were performed using the channels A-B and C-D. A dataset showing transport measurement results for the freshly cleaved  $\text{Na}_2\text{IrO}_3$  crystal is presented in Figure 7.7, where Figure 7.7 a) sketches the measurement geometry.

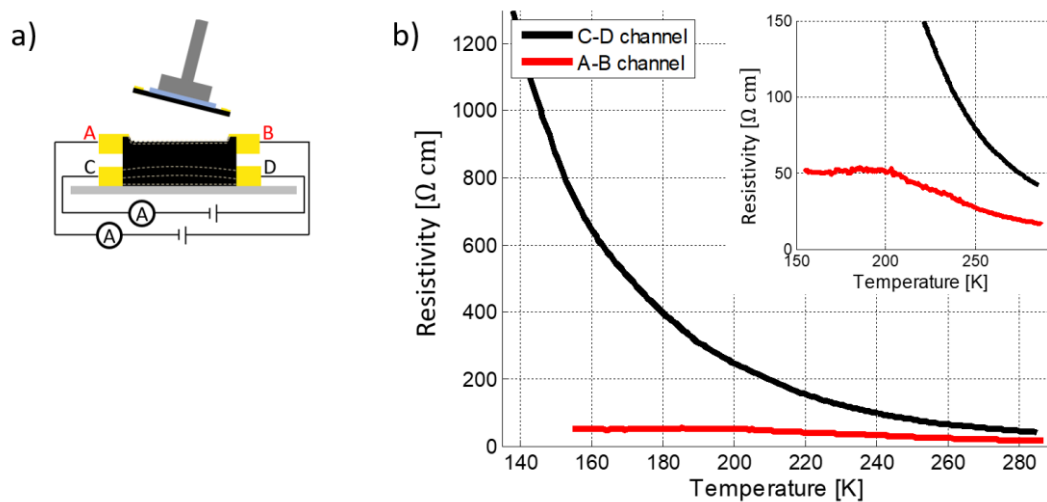


Figure 7.7 Electric transport measurements for freshly cleaved  $\text{Na}_2\text{IrO}_3$ . Two gold contact pairs from the channels A-B (top contacts) and C-D (bottom contacts), as sketched in a). b) Differential resistivity at 0 V versus temperature for both channels, showing a monotonic decay of the resistivity with temperature for the bottom contact measurement. Above  $\sim 205$  K, the top contact measurement also exhibits a monotonic  $\rho(T)$ -decay but with considerably reduced resistivity. Below  $\sim 205$  K, the course of the A-B-contact  $\rho(T)$  curve becomes approximately constant with a resistivity value of  $50 \text{ } \Omega\text{cm}$ . Since this behaviour is absent from the C-D-contact measurement, the resistivity plateau is assigned to the freshly cleaved surface.

Starting the analysis with the C-D channel data shown in Figure 7.7 b), black curve, it is observed that the in-plane  $\rho(T)$ -characteristic measured at the bottom channel remains unaffected by the crystal cleaving. The transport data collected using the top channel A-B,

which probes the freshly cleaved surface, show strongly different characteristics compared to the C-D-measurement and the transport investigation on the uncleaved sample in chapter 7.1. At temperatures above  $\sim 205$  K, the resistivity monotonically decreases with the temperature similar to the  $\rho(T)$ -curve taken with the A-B-channel on the uncleaved sample. However, compared to the uncleaved case, the absolute resistivity values are lower at high temperatures despite the increased contact-contact spacing, e.g. decreased from  $56 \text{ } \Omega\text{cm}$  to  $16.5 \text{ } \Omega\text{cm}$  at  $286$  K after cleaving. Below  $\sim 205$  K, the A-B  $\rho(T)$ -curve in Figure 7.7 b) shows an extended plateau with a resistivity of  $52 \text{ } \Omega\text{cm}$ .

The  $\rho$ -plateau as low temperature  $\rho(T)$ -characteristic cannot be explained by transport via hopping or thermally excited charge carriers alone and is therefore not covered by the transport pictures provided in the literature on  $\text{Na}_2\text{IrO}_3$  or in chapter 7.1. As the existence of the freshly cleaved surface is the key difference, the changes of the transport characteristics in the A-B-channel are assigned to the freshly cleaved  $\text{Na}_2\text{IrO}_3$  surface.

The transport characteristics measured via the C-D channel remained unchanged after cleaving. It is assumed that the induced current density between contacts C-D does not reach far enough into the crystal (out-of-plane direction) to probe the freshly cleaved surface. To estimate the current density in the crystalline out-of-plane direction, simulations using COMSOL version 5.5 were done modelling the  $\text{Na}_2\text{IrO}_3$  crystal by a resistor network. The geometry was chosen according to the contact geometry in the transport experiments, the in-plane resistivity values were taken from the transport data of the uncleaved crystal. For the out-of-plane resistivity, the in-plane resistivity was multiplied with a factor of  $10^3$  to account for the anisotropic transport in  $\text{Na}_2\text{IrO}_3$  (see chapter 4.1). The results of the simulation are shown in Figure 7.8.

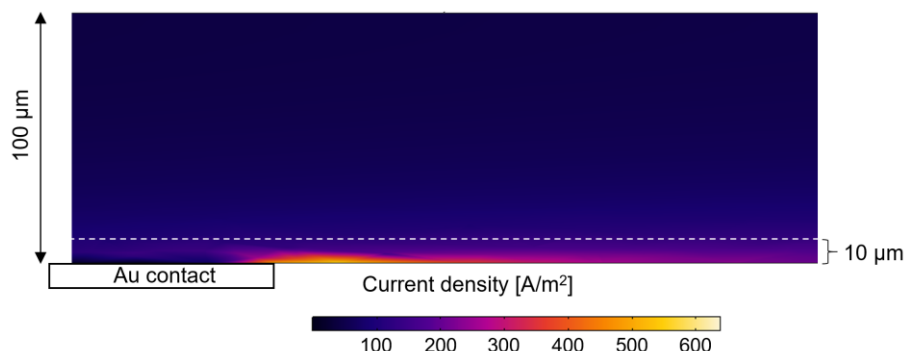


Figure 7.8 Simulation of the current density distribution in a  $\text{Na}_2\text{IrO}_3$  single crystal with two gold contacts attached in a geometry for in-plane transport measurements. The second contact is not shown in the depiction and lies far to the right. The contact-contact spacing was set to  $1 \text{ mm}$  and the voltage to  $1 \text{ V}$ . The current density rapidly decreases in out-of-plane direction and becomes neglectable above  $\sim 10 \text{ } \mu\text{m}$ .

The simulation results show that significant current density reaches not further than 10  $\mu\text{m}$  into the crystal for transport investigations via two contacts on the same crystal side (the second contact is not shown in Figure 7.8), being 1 mm apart. Hence, according to the simulation, if the remaining thickness of the  $\text{Na}_2\text{IrO}_3$  sample after cleaving is larger than 20  $\mu\text{m}$ , measurements performed with contacts A and B can be treated independently from measurements using contacts C and D. This is in accordance with the observation that the transport via the C-D-channel is unaffected by the cleaving. The sample thickness before cleaving was  $\sim 100 \mu\text{m}$  (chapter 5.4). The remaining thickness after cleaving is difficult to determine, as the sample is surrounded by epoxy adhesive, but was estimated by examination in an optical microscope to be between 55  $\mu\text{m}$  and 60  $\mu\text{m}$ .

For the further analysis of the transport characteristics of the freshly cleaved  $\text{Na}_2\text{IrO}_3$  surface probed via the contacts A and B, a simple model will be provided. As mentioned, above 205 K the A-B  $\rho(T)$ -curve qualitatively resembles the same monotonic decay with temperature as the uncleaved crystal, but with reduced overall resistance. In the proposed model, this  $\rho(T)$ -behaviour is assigned to bulk conductance in  $\text{Na}_2\text{IrO}_3$ . This conductance via the bulk is referred to as the bulk channel in the following. The freshly cleaved surface provides a second conducting channel in the model, referred to as the surface channel. In this two-channel model, the surface and the bulk channels are represented by two parallel resistors, i.e.  $R_{\text{surface}}$  and  $R_{\text{bulk}}$ , being electrically connected to terminal A and B. A simplifying assumption is that the resistors are independent from each other. An overview over the two-channel model is depicted in Figure 7.9.

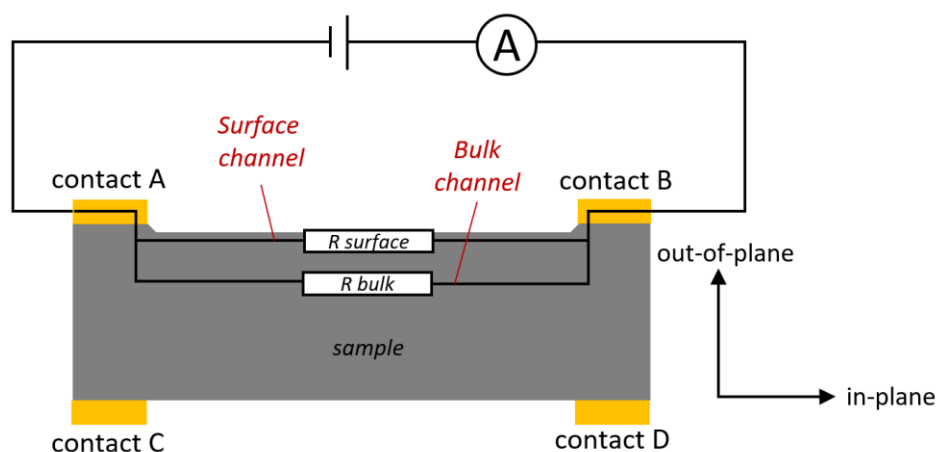


Figure 7.9 Two-channel model to analyse the surface related transport properties for freshly cleaved  $\text{Na}_2\text{IrO}_3$ . The A-B-channel measurement are treated as measurements of two parallel resistors, namely  $R_{\text{surface}}$  and  $R_{\text{bulk}}$ .

Within the framework of the two-channel model, bulk ( $\rho_{\text{bulk}}$ ) and surface ( $\rho_{\text{surface}}$ ) related resistivity are disentangled from the overall resistivity of the A-B-channel  $\rho_{\text{A-B}}$  using:

$$1/\rho_{\text{A-B}} = 1/\rho_{\text{bulk}} + 1/\rho_{\text{surface}} \quad . \quad 7.6$$

The simplicity of this model does not reflect any possible entanglements between the bulk and the surface channel. Since the picture underlying the surface transport mechanism is still under discussion, the characteristics of entanglements between both channels are not yet clear. Hence, the two-channel model is sufficient to roughly estimate the resistivity of the freshly cleaved  $\text{Na}_2\text{IrO}_3$  surface but should not be used to extract detailed insights to the temperature characteristics of the surface channel.

As the reference data for the bulk channel the A-B-channel transport measurements on the uncleaved crystal are taken. This is shown in Figure 7.10.

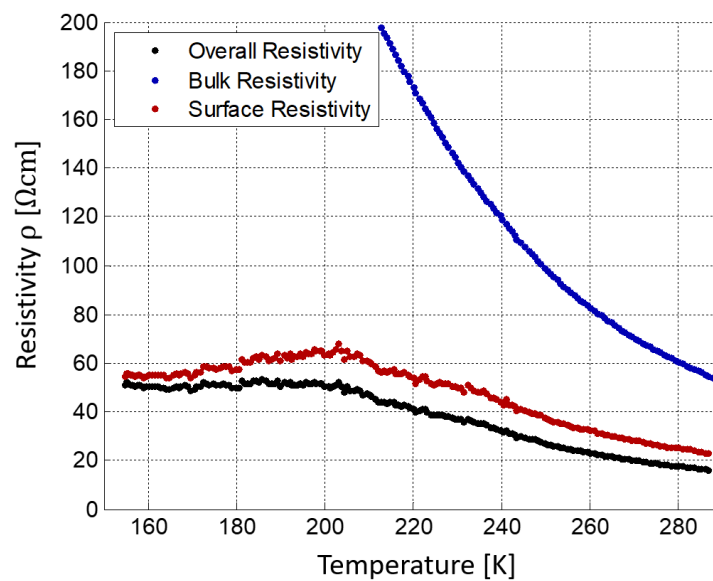


Figure 7.10 Disentangled differential resistivity contributions of the bulk and surface at 0 V. The bulk reference data (blue curve) is taken from the A-B-channel transport measurement on the uncleaved sample. Using equation 7.6 in the framework of the two-channel-model, this yields the temperature dependent resistivity of the surface (red curve). The surface resistivity stays in the same order of magnitude for the whole temperature range, indicating a different physical origin of the surface conductance compared to the bulk conductance.

Here, the red curve in Figure 7.10 shows the differential surface resistivity. In contrast to the bulk resistivity, which decreases with temperature, the surface resistivity remains in the same order of magnitude, having a maximum of 67  $\Omega\text{cm}$  and a minimum of 23.5  $\Omega\text{cm}$ . Furthermore, the surface conductance does not increase with decreasing temperature below  $\sim 205$  K. Hence,

at low temperatures the surface related transport cannot be explained by hopping conductance or by conductance from thermally excited charge carriers. What is clear is the fact that the surface resistivity is much lower than the bulk resistivity and that the surface transport does not freeze out, as sketched in Figure 7.11 in the framework of the two-channel model.

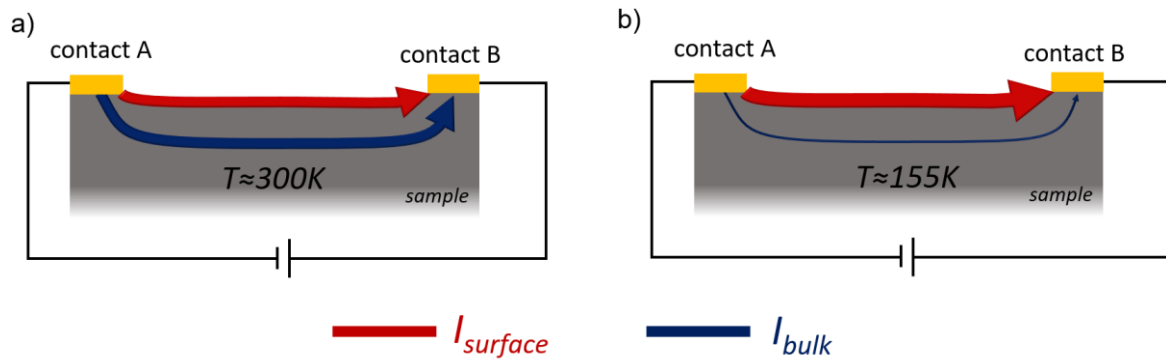


Figure 7.11 Model in the two-channel picture on the  $\rho(T)$  findings for the freshly cleaved surface found in transport measurements using the A-B-channel. a), b) Current densities through the surface (red) and bulk (blue) channels at a given voltage between contacts A and B. At high temperatures, surface and bulk channel carry similar current densities. Upon decreasing temperature, the bulk channel freezes out and the surface channel dominates the overall conductance.

The bulk channel hopping conductivity is marked in blue in Figure 7.11 and the high surface conductivity is marked in red. At high temperatures the conductivities from the bulk and the surface channel are in the same order of magnitude, which is reflected in Figure 7.11 a). Upon cooling the sample, the bulk channel freezes out while the surface channel resistivity stays in the same order of magnitude, Figure 7.11 b). Consequently, the share of overall current flowing through the surface channel rises upon cooling, until the residual current going through the bulk channel becomes neglectable. At this point, the surface channel dominates the overall A-B conductance and the characteristics of the bulk channel disappear from in the measured transport data. This corresponds to the observed resistivity plateau below  $\sim 205\text{ K}$  in Figure 7.7.

Finally, the absolute resistance of the surface channel is discussed. Presuming that the surface transport current density is indeed confined to the  $\text{Na}_2\text{IrO}_3$  surface, the surface sheet resistance is between  $0.5\text{ k}\Omega/\square$  and  $2.0\text{ k}\Omega/\square$  at  $155\text{ K}$ , depending on the estimated contact area between the gold contacts and the sample surface that was evaluated using an optical microscope. This is comparable with a  $\text{Si}(111)7 \times 7$  surface ( $\approx 1.25\text{ k}\Omega/\square$  at  $300\text{ K}$ ) and graphene on  $6\text{H-SiC}$  ( $\approx 0.6\text{ k}\Omega/\square$  at  $200\text{ K}$  and  $\approx 0.8\text{ k}\Omega/\square$  at  $300\text{ K}$ ) [128], [129]. It is a remarkably low value considering the high defect density at the  $\text{Na}_2\text{IrO}_3$  surface and the relatively poor bulk conductance at low temperatures. Even for metallic surfaces, it would be

expected that the high defect concentration leads to a rather bad metal with defect scattering inhibiting a high conductance (chapter 5.7.1). Regarding the contact quality: it was argued in chapter 7.1 that contacts A and B had good quality before cleaving. If cleaving reduced that quality, i.e. increased the contact resistance, the found surface conductance would be underestimated in Figure 7.10 in the whole temperature range. Hence, if contact A and/or B had bad quality after cleaving, the freshly cleaved  $\text{Na}_2\text{IrO}_3$  surface would have an even lower sheet resistance than  $0.5 \text{ k}\Omega/\square$  -  $2.0 \text{ k}\Omega/\square$  at 155 K.

Summary of the transport on the freshly cleaved  $\text{Na}_2\text{IrO}_3$  surface:

- A highly conductive channel was found on the freshly cleaved  $\text{Na}_2\text{IrO}_3$  surface.
- Below  $\sim 205 \text{ K}$ , the surface channel dominates the overall conductance.
- Transport mediated by the freshly cleaved surface cannot be explained in the hopping framework or with a thermal excitation ansatz as for the  $\text{Na}_2\text{IrO}_3$  bulk.
- The conductive surface channel is not found for every  $\text{Na}_2\text{IrO}_3$  sample, suggesting a critical dependency on the synthesis process.

## 7.4 The Effect of Air Dosing on the Surface Conductance

Former investigations on the chemical stability of  $\text{Na}_2\text{IrO}_3$  revealed its degeneration upon simultaneous exposure to  $\text{H}_2\text{O}$  and  $\text{CO}_2$ , where the concentrations in ambient air are sufficient to initiate the degeneration process (chapter 4.2). The previous chapter showed that transport measurements on freshly cleaved  $\text{Na}_2\text{IrO}_3$  surfaces exhibit vastly different characteristics compared to measurements on uncleaved samples. In the following, it will be investigated if the transport characteristics of the uncleaved crystal are restored by air dosing the fresh surface.

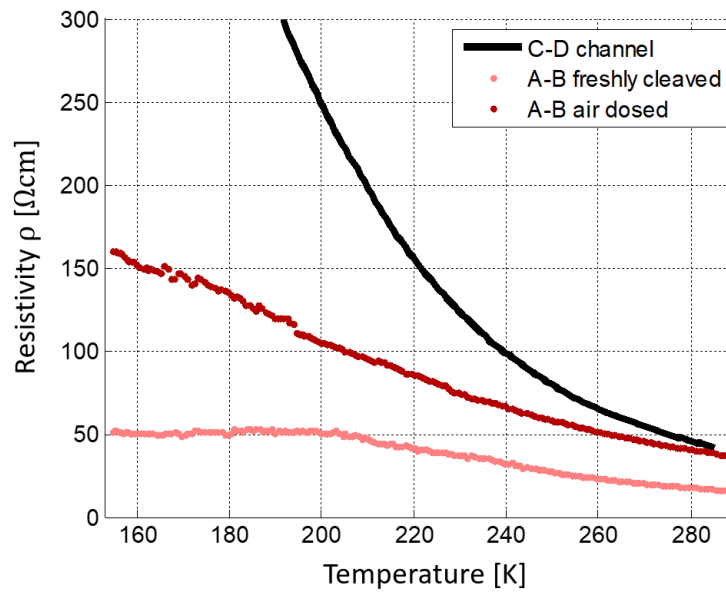


Figure 7.12 Comparison of differential resistivity  $\rho(T)$  at 0V between the freshly cleaved surface (pink curve) and the air dosed surface (red curve). After dosing the fresh  $\text{Na}_2\text{IrO}_3$  surface with ambient air for 13 h, the resistivity plateau below  $\sim 205$  K vanishes. The overall resistivity after air dosing is increased but does not match the bulk reference data, implying that the surface related conductivity is not entirely suppressed.

The measurement procedure was as follows: after performing the transport investigations on the freshly cleaved surface, the UHV chamber was vented with ambient air without removing the sample from the stage. After waiting for 13 hours, the chamber was re-evacuated to UHV, and the transport measurements were repeated with the exact same procedure as for the freshly cleaved surface. Hence, the sample and contact geometry did not change compared to the measurements on the freshly cleaved surface presented in chapter 7.3.

The impact of air dosing is depicted in Figure 7.12. The results for the A-B channel yield the following insights: firstly, the overall resistivity increased considerably after air dosing in the whole covered temperature range. Secondly, the resistivity plateau (pink curve) below  $\sim 205$  K vanishes after air dosing. Instead, the resistivity monotonically increases with decreasing temperature. And finally: the bulk characteristics (black line) are not fully restored after 13 hours of surface degeneration in ambient air.

Using the two-channel model and the analysis procedure presented in chapter 7.3, i.e. using the  $\rho(T)$ -data from the uncleaned A-B-channel transport measurement as reference, allows to disentangle the surface and bulk channel resistivity for the A-B channel after air dosing. This is shown in Figure 7.13.



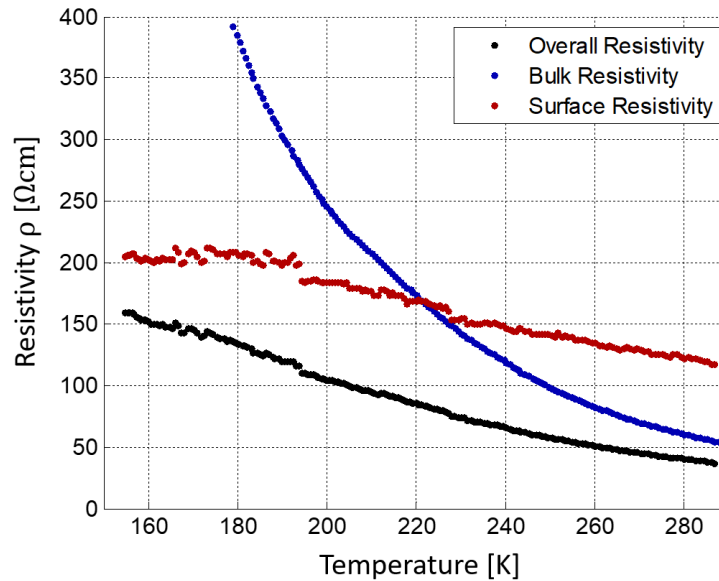


Figure 7.13 Disentangled contribution of the bulk and surface resistivity to the overall A-B-channel resistivity after air dosing the freshly cleaved  $\text{Na}_2\text{IrO}_3$  surface for 13 hours. The data shows the differential resistivity at 0 V.

Compared to the freshly cleaved surface, the air dosed surface channel has an overall higher resistivity, e.g.  $56 \Omega\text{cm}$  for the fresh surface versus  $205 \Omega\text{cm}$  for the air dosed surface at 155 K. At 286 K the surface resistivity for the freshly cleaved sample is  $23.5 \Omega\text{cm}$  and for the air dosed sample it is  $118 \Omega\text{cm}$ . Along with the  $\rho(155 \text{ K})$  value, this indicates that the surface resistivity increased by a factor of 3.6-5.0 upon 13 h of ambient air exposure. This is a remarkably slow degeneration of the surface, considering that it was reported that  $\text{Na}_2\text{IrO}_3$  fully degenerates in air within  $\sim 20$  hours [65], chapter 4.2. As these reports are based on x-ray diffraction measurements on  $\text{Na}_2\text{IrO}_3$  powder and not on single crystals, this indicates that single crystals might be more resilient to  $\text{H}_2\text{O}$  and  $\text{CO}_2$  induced degeneration.

The finding that air dosing changes the surface transport properties towards the bulk transport characteristics evidences that the highly conductive channel was correctly assigned to the  $\text{Na}_2\text{IrO}_3$  surface in chapter 7.3.

#### Summary on the effect of air dosing on the surface conductivity

- Air dosing the freshly cleaved surface with ambient air for 13 hours increases the surface channel resistivity by a factor of 3.6 - 5.0, slowly restoring the bulk transport characteristics.
- The degeneration process is slow for the single crystal surface compared to the degeneration of  $\text{Na}_2\text{IrO}_3$  powder.

## 8 Discussion of the Na<sub>2</sub>IrO<sub>3</sub> Surface Electronic Properties in the Joint Context of STM/STS and Transport Measurements

The published works on the Na<sub>2</sub>IrO<sub>3</sub> surface electronic properties paint a diffuse picture, reporting different band gap sizes (0.34 eV – 1.2 eV) or the occurrence of in-gap states and no apparent band gap (chapter 3.4). To this day, it is not clear why some ARPES works show an open band gap while others find no gap at all. The following discussion on the Na<sub>2</sub>IrO<sub>3</sub> surface electronic properties based on the findings presented in this thesis aims to contribute to resolve this situation.

These findings are summarized as follows:

- I. High surface conductance (sheet resistance between 0.5 k $\Omega$  $\square^{-1}$  and 2.5 k $\Omega$  $\square^{-1}$ ) despite high defect density.
- II. The surface conductance cannot be explained in a hopping picture or by transport via thermally excited charge carriers.
- III. Surface conductance stays in the same order of magnitude in the probed temperature regime.
- IV. Type 3 spectra, showing a V-shaped band gap closing resembling a Dirac-cone in a 2D system, have spectral weight in the vicinity of  $E_F$ .
- V. The tails of the type 2 D and D\* peaks introduce density of states in the vicinity of  $E_F$ .
- VI. Degeneration from air dosing the fresh surface slowly restores bulk transport properties.

Usually, a high conductance is associated with a density of delocalized states at the Fermi level  $E_F$  and no substantial scattering. In chapters 6.3.3 and 6.4, it was suggested that the emergence of type 3 spectra is a consequence of the bulk-boundary correspondence for a topologically insulating Na<sub>2</sub>IrO<sub>3</sub>. It was argued that Na<sub>2</sub>IrO<sub>3</sub> being a strong 3D-TI would be in accordance with the result that type 3 spectra occur on the free surface and not exclusively at step edges. Furthermore, it was shown that type 3 spectra are robust against extended defects like step edges. As described in chapter 5.7.5, topologically protected surface conductance is metallic and does not extend significantly into the bulk of the material. Furthermore, “backscattering” from non-magnetic impurities is forbidden, significantly reducing the impact of

defect scattering, i.e. allowing for a high conductance found in the transport investigation despite the high defect density found on the  $\text{Na}_2\text{IrO}_3$  surface.

However, topologically protected surface conductance should not decrease upon air dosing. In chapter 7.4 it was shown that the surface conductance does decrease from air dosing. A model potentially explaining this phenomenon for  $\text{Na}_2\text{IrO}_3$  is presented in Figure 8.1.

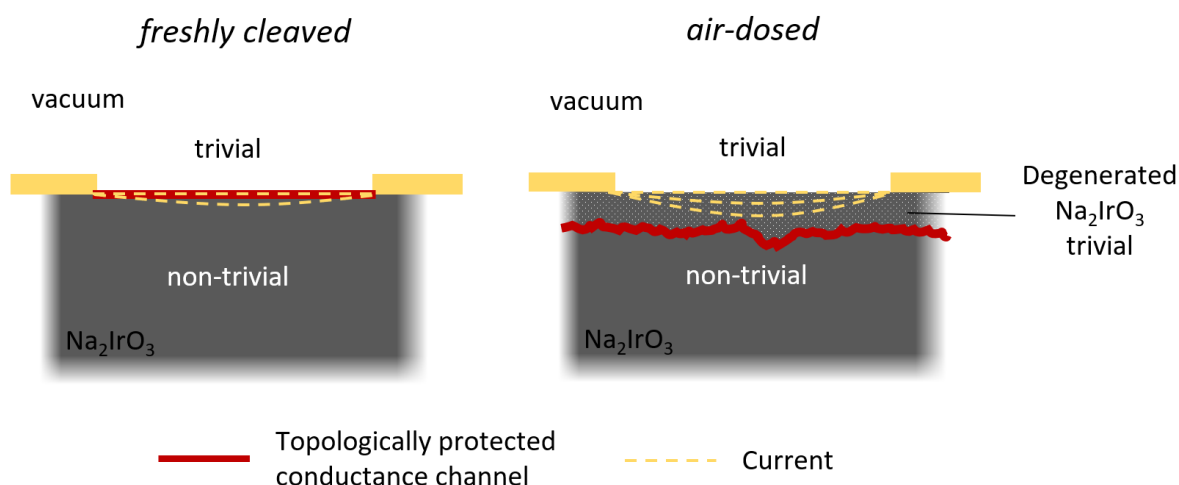


Figure 8.1 Model for the impact of the degeneration of  $\text{Na}_2\text{IrO}_3$  in air on the surface transport in the framework of strong 3D topology. After cleaving in UHV (left), the interface between the trivial vacuum and the non-trivial  $\text{Na}_2\text{IrO}_3$  is at the freshly cleaved surface. Upon applying a voltage between the surface contacts (gold), the electric current flows through the topologically protected surface states and through the  $\text{Na}_2\text{IrO}_3$  bulk. After air dosing (right), the exposed  $\text{Na}_2\text{IrO}_3$  degenerates, beginning at the surface and slowly continuing into the bulk. The degenerated  $\text{Na}_2\text{IrO}_3$  would be topologically trivial and the non-trivial to trivial interface would gradually move inside the sample. Upon applying a voltage between the surface contacts, the current needs to pass the degenerated material. The share of current density passing through the topologically protected states depends on the thickness of the degenerated volume. Hence, the observed metallicity at the surface gets gradually weaker upon air dosing.

For the freshly cleaved surface, the interface between the topologically trivial vacuum and a topologically non-trivial  $\text{Na}_2\text{IrO}_3$  volume would be the freshly cleaved surface itself. Hence, the surface transport channel is easily addressed by the contacts adjacent to the surface and therefore prominent in the transport measurements. After dosing the surface with air, the probed material degenerates. Assuming that degenerated  $\text{Na}_2\text{IrO}_3$  is topologically trivial, the trivial-to-non-trivial interface is found at the interface between the degenerated and the pristine  $\text{Na}_2\text{IrO}_3$  within the bulk of the sample. This interface gradually moves into the bulk upon continued air dosing. Consequently, the share of current density reaching the topologically protected conductive states in transport measurements decreases with air dosing, and the overall transport is increasingly bulk transport mediated. This could equally explain why uncleaned  $\text{Na}_2\text{IrO}_3$  samples do not show the highly conductive channel, as they were in contact with air during the pre-characterization and measurement preparation process, pushing the

topologically protected conductive states into the bulk of the material. In this context, any surface-sensitive investigation that did not cleave the  $\text{Na}_2\text{IrO}_3$  sample in UHV would not have observed in-gap states, potentially explaining why different ARPES investigations yield vastly different results.

To conclusively resolve if non-trivial topology is responsible for the transport characteristics of the  $\text{Na}_2\text{IrO}_3$  surface, further experimental evidence of prohibited backscattering for the assumed topologically protected channel is required. In STM/STS measurements, this can be provided by quasiparticle interference measurements. The STS experiments conducted in the scope of this thesis showed that for temperatures at and above 80 K, no quasiparticle interference pattern could be observed. Hence, either there is no such pattern, disproving that non-trivial topology is found in  $\text{Na}_2\text{IrO}_3$ , or the signal to noise ratio is insufficient to observe clear QPI-patterns. This underlines the importance of the first successful STM measurements at 8 K on  $\text{Na}_2\text{IrO}_3$  done in this work, providing a new path for future investigations of the  $\text{Na}_2\text{IrO}_3$  surface in the context of topology.

It is worth discussing other phenomena than topology as possible source of the  $\text{Na}_2\text{IrO}_3$  surface conductance. One such phenomenon is an insulator-metal transition induced by heavy doping (see chapter 5.7.2.2). It is worth noting that this is not the same as the Mott-Hubbard-insulator-metal transition discussed in chapter 6.3.3 for type 3 spectra. The STM investigations showed a high defect density on the  $\text{Na}_2\text{IrO}_3$  surface, and two spectral types – types 2 and 3 – show spectral weight in the vicinity of  $E_F$ . However, as was argued in chapter 7.2 for type 2 spectra, the states close to  $E_F$  are likely to be localized due to disorder. Assuming that the V-shape in type 3 spectra emerges due to band tailing, the picture regarding the localization of the states for the type 2 spectra applies equally for type 3 spectra, since the Fermi level is found at the minimum of the type 3 V-shape and not within a band tail. Hence, hopping transport would be expected in such a case and a doping induced insulator-metal transition does not fit to the combination of transport and STM/STS findings.

Another picture to consider is the existence of surface states that are not topology related, i.e. states that emerge due to the termination of a material with a surface, resulting in a change of the band structure at the interface between bulk and vacuum. As air dosing  $\text{Na}_2\text{IrO}_3$  changes the chemical composition of the material at the surface, also the surface states would be expected to be affected, possibly fitting to the observation that the surface conductance decreases upon air dosing. However, surface states would also be affected by scattering, and considering the high defect density, the found surface conductance is rather high for this picture. Additionally, surface states should have been observed in prior STM/STS measurements, which was not the case (chapter 3.4).

From the discussion of the possible phenomena underlying the surface conductance in  $\text{Na}_2\text{IrO}_3$ , strong 3D topological non-triviality fits best to the experimental findings. Furthermore, the spectral type showing the hallmark of topology would be type 3, which is in accordance with the assignment of the spectral types 1 and 2 to the  $\text{Na}_2\text{IrO}_3$  bulk electronic properties.

However, to conclusively assign the surface conductance to topologically protected states, the confirmation of prohibited backscattering is required. At the time this thesis is written, work on this is done in the group of M. Wenderoth, Göttingen University. Until this validation/falsification is done, it is not clear if non-trivial topology causes the high  $\text{Na}_2\text{IrO}_3$  surface conductance or if another, yet unconsidered exotic mechanism underlies the experimental findings. On the one hand, it highlights the challenging high complexity of the material in regards of its electronic properties. On the other hand, it provides a fantastic opportunity for investigations including a broad field of physical phenomena, potentially leading to insights that reach beyond the  $\text{Na}_2\text{IrO}_3$  sample system.

## 9 Summary and Outlook

The work on this thesis was initiated by the theoretical prospect of  $\text{Na}_2\text{IrO}_3$  being a topological insulator. In this thesis, for the first time, a highly conductive surface channel was found for freshly cleaved  $\text{Na}_2\text{IrO}_3$  single crystals. To perform the revealing transport measurements, a new experimental UHV-setup was developed, enabling the investigation of the freshly cleaved surface, avoiding any contact with degenerating ambient air. The conductivity of the surface was found to show a fundamentally different temperature characteristic than the  $\text{Na}_2\text{IrO}_3$  bulk transport. With a low surface sheet resistance between  $0.5 \text{ k}\Omega/\square$  and  $2.0 \text{ k}\Omega/\square$ , the surface channel is highly conductive. The low resistance becomes even more remarkable considering the very high defect density on the freshly cleaved surface found for all investigated samples by STM, suggesting that defect scattering has only a minor impact on the surface conductance. As two samples from two different synthesis batches showed this high surface conductance, while no sample of a third batch showed similar results, it is suspected that the emergence of the conductive surface channel is strongly dependent on the sample synthesis. Tunnelling spectroscopy measurements reveal the existence of in-gap states that resemble a Dirac cone. These in-gap states were found to be a feature of the surface and robust against defects and step edges. This combination of a highly conductive surface, in-gap states resembling a Dirac cone and robustness against defects is the hallmark of the bulk-boundary correspondence for a strong 3D topological insulator.

To conclusively prove the existence of a topologically non-trivial phase in  $\text{Na}_2\text{IrO}_3$ , the prohibition of backscattering needs to be verified for the surface channel. This can be achieved, e.g. via quasiparticle interference investigations in STM/STS measurements and spin-resolved ARPES. In the literature, the ARPES data neither provides a coherent picture regarding the characteristics of the  $\text{Ir-}j_{\text{eff}}=1/2$  Hubbard bands, nor a clear answer to the question if in-gap states exist on the  $\text{Na}_2\text{IrO}_3$  surface. Hence, quasiparticle interference investigations of the  $\text{Na}_2\text{IrO}_3$  surface are highly desirable.

For this, STM experiments were extended by a laser setup. QPI measurements require an excellent signal to noise ratio that is not provided in scanning tunnelling experiments at 80 K or above. As the  $\text{Na}_2\text{IrO}_3$  bulk conductance freezes out upon cooling, STM experiments below 80 K were not successful up to now. The new setup changed this by providing conductance via optically excited charge carriers, where the laser spot was adjusted in a way that ensures the illumination of the tunnelling junction as well as the sample surface between the tunnelling junction and a gold contact. As a result, the first successful STM measurements on  $\text{Na}_2\text{IrO}_3$  at 8 K were executed, exhibiting that the (1x1)-reconstruction of the surface persists at low

temperatures. This new technique opens the path for future low temperature STM/STS investigations not only for  $\text{Na}_2\text{IrO}_3$ , but also for  $\alpha\text{-Li}_2\text{IrO}_3$  and other materials that feature hopping mediated conductance.

Next to the findings on the conductive surface channel, the results and discussions in this thesis resolve the discrepancy between STM/STS publications and ARPES/optical conductivity works regarding the size and temperature dependence of the  $\text{Na}_2\text{IrO}_3$  Mott gap. By using modified STM tips, it was shown that different spectral types corresponding to the inherent  $\text{Na}_2\text{IrO}_3$  electronic structure can be observed by means of STS. Next to the spectral type showing in-gap states resembling a Dirac cone (spectral type 3) mentioned above, two further spectral types were found. Type 1 exhibits a 0.8 eV spectral gap at 300 K as well as a 1.2 eV spectral gap at 80 K, and was already reported in the STM/STS works of Lüpke et al. [18], [29]. As type 1 was the only spectral type observed in those STM/STS works, the according spectral gap was assigned to the Mott gap, even though non-STM/STS works found substantially smaller and temperature independent Mott gaps. The observation of type 2 spectra in this thesis, showing two  $dI/dV$  peaks at  $\pm 0.5$  eV, resolves the discrepancy between STM/STS and non-STM/STS works. With this, the type 1 spectral gap could be assigned to the  $\text{Na}_2\text{IrO}_3$   $j_{\text{eff}} = 3/2 - e_g$  energy gap, while the spectral weight peaks in type 2 spectra were assigned to the Hubbard bands. This attribution fits to the energy diagram of the Ir 5d states, being energetically split by crystal field splitting, spin-orbit coupling and Hubbard repulsion, as well as to results from ARPES and optical conductivity works.

Finally, the  $\text{Na}_2\text{IrO}_3$  bulk transport characteristics were analysed, and it was found that the established picture, i.e. that 3D variable range hopping mediates the low temperature transport and conduction from thermally excited charge carriers mediates the transport above room temperature, is not the only suitable model. Here, it was argued that 2D variable range hopping describes the low temperature in-plane transport equally well and that nearest neighbour hopping might describe the bulk transport above room temperature.

Independently of the exact bulk transport mechanism, it is not clear from the literature what states mediate the hopping conductance. In this thesis, it was found that all  $\text{Na}_2\text{IrO}_3$  samples exhibit a high defect density, at least at the surface. Furthermore, it was shown that the  $dI/dV$  peaks in type 2 spectra have band tails that reach into the vicinity of the Fermi level. These peaks are attributed to the Hubbard bands. With both findings combined, it is proposed that the bulk hopping conductance is mediated by the Hubbard band states close to the Fermi level that are localized due to defect-induced disorder.

In summary, this thesis provides new insights to the electronic properties of  $\text{Na}_2\text{IrO}_3$  as well as a thorough discussion of the underlying mechanisms. It may serve as a guide for further



experimental studies to the honeycomb iridates and related materials. In this context,  $\text{Na}_2\text{IrO}_3$  is an ideal sample material, showing a rich variety of understood and still puzzling properties, opening another path to gain insights into the physics of strongly correlated materials.

## 10 Bibliography

- [1] M. Mitchell Waldrop, "More than Moore," *Nature*, vol. 530, pp. 144–147, 2016, doi: doi:10.1038/530144a.
- [2] S. Kumar, "Fundamental Limits to Moore's Law," *arXiv*, pp. 1–3, 2015, [Online]. Available: <http://arxiv.org/abs/1511.05956>.
- [3] F. D. M. Haldane, "Model for a quantum hall effect without Landau levels: Condensed-matter realization of the 'parity anomaly,'" *Phys. Rev. Lett.*, vol. 61, no. 18, pp. 2015–2018, 1988, doi: 10.1103/PhysRevLett.61.2015.
- [4] F. D. M. Haldane, "Nobel lecture: Topological quantum matter," *Rev. Mod. Phys.*, vol. 89, no. 4, pp. 1–10, 2017, doi: 10.1103/RevModPhys.89.040502.
- [5] M. König *et al.*, "Quantum Spin Hall Insulator State in HgTe Quantum Wells," *Science*, vol. 318, no. 5851, pp. 766–770, 2007, doi: 10.1126/science.1148047.
- [6] M. König *et al.*, "The quantum spin Hall effect: Theory and experiment," *J. Phys. Soc. Japan*, vol. 77, no. 3, pp. 1–14, 2008, doi: 10.1143/JPSJ.77.031007.
- [7] C. L. Kane and E. J. Mele, "Z<sub>2</sub> topological order and the quantum spin hall effect," *Phys. Rev. Lett.*, vol. 95, no. 14, pp. 3–6, 2005, doi: 10.1103/PhysRevLett.95.146802.
- [8] M. Z. Hasan and C. L. Kane, "Colloquium: Topological insulators," *Rev. Mod. Phys.*, vol. 82, no. 4, pp. 3045–3067, 2010, doi: 10.1103/RevModPhys.82.3045.
- [9] Y. Ando, "Topological insulator materials," *J. Phys. Soc. Japan*, vol. 82, no. 10, pp. 1–32, 2013, doi: 10.7566/JPSJ.82.102001.
- [10] F. Reis *et al.*, "Bismuthene on a SiC substrate : A candidate for a high-temperature quantum spin Hall material," *Science*, vol. 357, no. 6348, pp. 287–290, 2017.
- [11] S. Blügel, Y. Mokrousov, T. Schäpers, and Y. Ando, *Topological Matter - Topological Insulators, Skyrmions and Majoranas*. Forschungszentrum Jülich GmbH, 2017.
- [12] S. Hwan Chun *et al.*, "Direct evidence for dominant bond-directional interactions in a honeycomb lattice iridate Na<sub>2</sub>IrO<sub>3</sub>," *Nat. Phys.*, vol. 11, no. 6, pp. 462–466, 2015, doi: 10.1038/nphys3322.
- [13] P. Gegenwart and S. Trebst, "Spin-orbit physics: Kitaev matter," *Nat. Phys.*, vol. 11, no. 6, pp. 444–445, 2015, doi: 10.1038/nphys3346.
- [14] V. Hermann *et al.*, "High-pressure versus isoelectronic doping effect on the honeycomb iridate Na<sub>2</sub>IrO<sub>3</sub>," *Phys. Rev. B*, vol. 96, no. 19, pp. 1–10, 2017, doi: 10.1103/PhysRevB.96.195137.
- [15] S. M. Winter, Y. Li, H. O. Jeschke, and R. Valentí, "Challenges in design of Kitaev materials: Magnetic interactions from competing energy scales," *Phys. Rev. B*, vol. 93, no. 21, pp. 1–21, 2016, doi: 10.1103/PhysRevB.93.214431.
- [16] J. Chaloupka, G. Jackeli, and G. Khaliullin, "Kitaev-heisenberg model on a honeycomb lattice: Possible exotic phases in iridium oxides A<sub>2</sub>IrO<sub>3</sub>," *Phys. Rev. Lett.*, vol. 105, no. 2, 2010, doi: 10.1103/PhysRevLett.105.027204.
- [17] Y. Singh *et al.*, "Relevance of the Heisenberg-Kitaev model for the honeycomb lattice iridates A<sub>2</sub>IrO<sub>3</sub>," *Phys. Rev. Lett.*, vol. 108, no. 12, 2012, doi: 10.1103/PhysRevLett.108.127203.

- [18] F. Lüpke, S. Manni, S. C. Erwin, I. I. Mazin, P. Gegenwart, and M. Wenderoth, "Highly unconventional surface reconstruction of Na<sub>2</sub>IrO<sub>3</sub> with persistent energy gap," *Phys. Rev. B - Condens. Matter Mater. Phys.*, vol. 91, no. 4, 2015, doi: 10.1103/PhysRevB.91.041405.
- [19] R. Comin *et al.*, "Na<sub>2</sub>IrO<sub>3</sub> as a novel relativistic mott insulator with a 340-meV gap," *Phys. Rev. Lett.*, vol. 109, no. 26, 2012, doi: 10.1103/PhysRevLett.109.266406.
- [20] D. Pesin and L. Balents, "Mott physics and band topology in materials with strong spin-orbit interaction," *Nat. Phys.*, vol. 6, no. 5, pp. 376–381, 2010, doi: 10.1038/NPHYS1606.
- [21] A. Shitade, H. Katsura, J. Kuneš, X.-L. Qi, S.-C. Zhang, and N. Nagaosa, "Quantum Spin Hall Effect in a Transition Metal Oxide Na<sub>2</sub>IrO<sub>3</sub>," *Phys. Rev. Lett.*, vol. 102, no. 25, p. 256403, 2009, doi: 10.1103/PhysRevLett.102.256403.
- [22] H. C. Jiang, Z. C. Gu, X. L. Qi, and S. Trebst, "Possible proximity of the Mott insulating iridate Na<sub>2</sub>IrO<sub>3</sub> to a topological phase: Phase diagram of the Heisenberg-Kitaev model in a magnetic field," *Phys. Rev. B - Condens. Matter Mater. Phys.*, vol. 83, no. 24, 2011, doi: 10.1103/PhysRevB.83.245104.
- [23] M. Laubach, J. Reuther, R. Thomale, and S. Rachel, "Three-band Hubbard model for Na<sub>2</sub>IrO<sub>3</sub>: Topological insulator, zigzag antiferromagnet, and Kitaev-Heisenberg material," *Phys. Rev. B*, vol. 96, no. 12, pp. 4–9, 2017, doi: 10.1103/PhysRevB.96.121110.
- [24] C. H. Kim, H. S. Kim, H. Jeong, H. Jin, and J. Yu, "Topological quantum phase transition in 5d transition metal oxide Na<sub>2</sub>IrO<sub>3</sub>," *Phys. Rev. Lett.*, vol. 108, no. 10, 2012, doi: 10.1103/PhysRevLett.108.106401.
- [25] B. H. Kim, K. Seki, T. Shirakawa, and S. Yunoki, "Topological property of a t<sub>2</sub>g<sub>5</sub> system with a honeycomb lattice structure," *Phys. Rev. B*, vol. 99, no. 15, pp. 1–16, 2019, doi: 10.1103/PhysRevB.99.155135.
- [26] L. Moreschini *et al.*, "Quasiparticles and charge transfer at the two surfaces of the honeycomb iridate Na<sub>2</sub>IrO<sub>3</sub>," *Phys. Rev. B*, vol. 96, no. 16, pp. 2–6, 2017, doi: 10.1103/PhysRevB.96.161116.
- [27] R. Comin *et al.*, "Na<sub>2</sub>IrO<sub>3</sub> as a Novel Relativistic Mott Insulator with a 340 meV Gap," *Phys. Rev. Lett.*, vol. 109, no. 26, 2012.
- [28] Y. Singh and P. Gegenwart, "Antiferromagnetic Mott insulating state in single crystals of the honeycomb lattice material Na<sub>2</sub>IrO<sub>3</sub>," *Phys. Rev. B - Condens. Matter Mater. Phys.*, vol. 82, no. 6, 2010, doi: 10.1103/PhysRevB.82.064412.
- [29] F. Lüpke, "Raster-Tunnel-Spektroskopie an Natrium-Iridat," Georg-August Universität Göttingen, Master Thesis, 2013.
- [30] S. M. Winter *et al.*, "Models and Materials for Generalized Kitaev Magnetism," *J. Phys. Condens. Matter*, vol. 29, no. 49, 2017.
- [31] S. Manni *et al.*, "Effect of isoelectronic doping on the honeycomb-lattice iridate A<sub>2</sub>IrO<sub>3</sub>," *Phys. Rev. B - Condens. Matter Mater. Phys.*, vol. 89, no. 24, 2014, doi: 10.1103/PhysRevB.89.245113.
- [32] S. K. Choi *et al.*, "Spin waves and revised crystal structure of honeycomb iridate Na<sub>2</sub>IrO<sub>3</sub>," *Phys. Rev. Lett.*, vol. 108, no. 12, 2012, doi: 10.1103/PhysRevLett.108.127204.
- [33] F. Ye *et al.*, "Direct evidence of a zigzag spin-chain structure in the honeycomb lattice: A neutron and x-ray diffraction investigation of single-crystal Na<sub>2</sub>IrO<sub>3</sub>," *Phys. Rev. B - Condens. Matter Mater. Phys.*, vol. 85, no. 18, 2012, doi: 10.1103/PhysRevB.85.180403.

- [34] B. J. Kim *et al.*, “Novel  $j_{\text{eff}}=1/2$  mott state induced by relativistic spin-orbit coupling in  $\text{Sr}_2\text{IrO}_4$ ,” *Phys. Rev. Lett.*, vol. 101, no. 7, 2008, doi: 10.1103/PhysRevLett.101.076402.
- [35] G. Jackeli and G. Khaliullin, “Mott insulators in the strong spin-orbit coupling Limit: From Heisenberg to a Quantum Compass and Kitaev Models,” *Phys. Rev. Lett.*, vol. 102, no. 1, 2009, doi: 10.1103/PhysRevLett.102.017205.
- [36] A. Dhingra *et al.*, “Electronic band structure of iridates,” *Mater. Horizons*, vol. 8, no. 8, pp. 2151–2168, 2021, doi: 10.1039/d1mh00063b.
- [37] J. Rodriguez *et al.*, “Competition between magnetic order and charge localization in  $\text{Na}_2\text{IrO}_3$  thin crystal devices,” *Phys. Rev. B*, vol. 101, no. 23, pp. 2–7, 2020, doi: 10.1103/PhysRevB.101.235415.
- [38] S. Francoeur, M. J. Seong, A. Mascarenhas, S. Tixier, M. Adamczyk, and T. Tiedje, “Band gap of  $\text{GaAs}_{1-x}\text{Bi}_x$ ,  $0 < x < 3.6\%$ ,” *Appl. Phys. Lett.*, vol. 82, no. 22, pp. 3874–3876, 2003, doi: 10.1063/1.1581983.
- [39] O. Korneta, “A Systematic Study of Transport, Magnetic and Thermal Properties of Layered Iridates,” University of Kentucky, PhD Thesis, 2012.
- [40] F. S. Freund, “Synthese und physikalische Untersuchungen von Kitaev-Honigwabeniridate,” Universität Augsburg, PhD Thesis, 2019.
- [41] F. A. Cotton, *Chemical Applications of Group Theory*, 3rd ed. Wiley-Interscience, 1990.
- [42] B. H. Kim, G. Khaliullin, and B. I. Min, “Electronic excitations in the edge-shared relativistic Mott insulator:  $\text{Na}_2\text{IrO}_3$ ,” *Phys. Rev. B - Condens. Matter Mater. Phys.*, vol. 89, no. 8, 2014, doi: 10.1103/PhysRevB.89.081109.
- [43] H. Gretarsson *et al.*, “Crystal-field splitting and correlation effect on the electronic structure of  $\text{A}_2\text{IrO}_3$ ,” *Phys. Rev. Lett.*, vol. 110, no. 7, 2013, doi: 10.1103/PhysRevLett.110.076402.
- [44] K. Foyevtsova, H. O. Jeschke, I. I. Mazin, D. I. Khomskii, and R. Valentí, “Ab initio analysis of the tight-binding parameters and magnetic interactions in  $\text{Na}_2\text{IrO}_3$ ,” *Phys. Rev. B - Condens. Matter Mater. Phys.*, vol. 88, no. 3, 2013, doi: 10.1103/PhysRevB.88.035107.
- [45] T. J. O’Reilly and E. L. Offenbacher, “Molecular Orbital Calculation for Trigonal Distorted Octahedral Complexes,” *J. Chem. Phys.*, vol. 54, no. 7, 1971, doi: 10.1063/1.1675294.
- [46] H. Haken and H. C. Wolf, *Atom- und Quantenphysik*, 8th ed. Springer-Verlag Berlin Heidelberg, 2004.
- [47] N. F. Mott, “The basis of the electron theory of metals, with special reference to the transition metals,” *Proc. Phys. Soc. Sect. A*, vol. 62, no. 7, pp. 416–422, 1949, doi: 10.1088/0370-1298/62/7/303.
- [48] H. Bluhm, T. Brückel, M. Morgenstern, G. von Plessen, and C. Stampfer, *Electrons in Solids*. de Gruyter, 2019.
- [49] J. Hubbard, “Electron correlations in narrow energy bands,” *Proc. R. Soc. London a Math. Phys. Eng. Sci.*, vol. 276, no. 1365, pp. 238–257, 1963.
- [50] S. Maekawa, T. Tohyama, S. E. Barnes, S. Ishihara, W. Koshibae, and G. Khaliullin, *Physics of Transition Metal Oxides*. Springer-Verlag Berlin Heidelberg, 2004.
- [51] J. Hubbard, “Electron Correlations in Narrow Energy Bands,” *Proc. R. Soc. London a Math. Phys. Eng. Sci.*, vol. 276, no. 1365, pp. 238–257, 1963.
- [52] V. Ambegaokar, B. I. Halperin, and J. S. Langer, “Hopping conductivity in disordered systems,”

- Phys. Rev. B*, vol. 4, no. 8, pp. 2612–2620, 1971, doi: 10.1103/PhysRevB.4.2612.
- [53] T. Dziuba, I. M. Pietsch, M. Stark, G. A. Traeger, P. Gegenwart, and M. Wenderoth, “Surface Conductivity of the Honeycomb Spin–Orbit Mott Insulator Na<sub>2</sub>IrO<sub>3</sub>,” *Phys. Status Solidi Basic Res.*, vol. 258, no. 1, 2021, doi: 10.1002/pssb.202000421.
- [54] J. M. Kosterlitz, “Nobel lecture: Topological defects and phase transitions,” *Rev. Mod. Phys.*, vol. 89, no. 4, pp. 1–7, 2017, doi: 10.1103/RevModPhys.89.040501.
- [55] J. E. Moore, “The birth of topological insulators,” *Nature*, vol. 464, no. 7286, pp. 194–198, 2010, doi: 10.1038/nature08916.
- [56] M. V. Berry, “Quantal phase factors accompanying adiabatic changes,” *Proc. R. Soc. A*, vol. 392, no. 1802, 1984, doi: <https://doi.org/10.1098/rspa.1984.0023>.
- [57] M. Nakahara, *Geometry, Topology and Physics*, 2nd ed. CRC Press, 2003.
- [58] D. J. Thouless, M. Kohmoto, M. P. Nightingale, and M. den Nijs, “Quantized Hall conductance in a two dimensional periodic potential,” *Phys. Rev. Lett.*, vol. 49, no. 6, pp. 405–408, 1982.
- [59] H. Weng, X. Dai, and Z. Fang, “Exploration and prediction of topological electronic materials based on first-principles calculations,” *MRS Bull.*, vol. 39, no. 10, pp. 849–858, 2014, doi: 10.1557/mrs.2014.216.
- [60] D. Pesin and L. Balents, “Mott physics and band topology in materials with strong spin-orbit interaction,” *Nat. Phys.*, vol. 6, no. 5, pp. 376–381, 2010, doi: 10.1038/nphys1606.
- [61] N. Alidoust *et al.*, “Observation of metallic surface states in the strongly correlated Kitaev–Heisenberg candidate Na<sub>2</sub>IrO<sub>3</sub>,” *Phys. Rev. B - Condens. Matter Mater. Phys.*, vol. 93, no. 24, 2016, doi: 10.1103/PhysRevB.93.245132.
- [62] K. Mehlawat and Y. Singh, “Density wave like transport anomalies in surface doped Na<sub>2</sub>IrO<sub>3</sub>,” *AIP Adv.*, vol. 7, no. 5, 2017, doi: 10.1063/1.4974916.
- [63] S. Manni, “Synthesis and investigation of frustrated Honeycomb lattice iridates and rhodates,” Georg-August-Universität, PhD Thesis, 2014.
- [64] M. Jenderka, J. Barzola-Quiquia, Z. Zhang, H. Frenzel, M. Grundmann, and M. Lorenz, “Mott variable-range hopping and weak antilocalization effect in heteroepitaxial Na<sub>2</sub>IrO<sub>3</sub> thin films,” *Phys. Rev. B - Condens. Matter Mater. Phys.*, vol. 88, no. 4, 2013, doi: 10.1103/PhysRevB.88.045111.
- [65] J. W. Krizan, J. H. Roudebush, G. M. Fox, and R. J. Cava, “The chemical instability of Na<sub>2</sub>IrO<sub>3</sub> in air,” *Mater. Res. Bull.*, vol. 52, pp. 162–166, 2014, doi: 10.1016/j.materresbull.2014.01.021.
- [66] A. Vasdev, L. Yadav, S. Kamboj, K. Mehlawat, Y. Singh, and G. Sheet, “Dynamic surface modification due to effusion of Na in Na<sub>2</sub>IrO<sub>3</sub>,” *J. Appl. Phys.*, vol. 124, no. 5, pp. 2–7, 2018, doi: 10.1063/1.5030606.
- [67] W. H. Bragg and W. L. Bragg, “The reflection of X-rays by crystals,” *Proc. R. Soc. A*, vol. 88, no. 605, 1913, doi: <https://doi.org/10.1098/rspa.1913.0040>.
- [68] J. Chaloupka, G. Jackeli, and G. Khaliullin, “Zigzag magnetic order in the iridium oxide Na<sub>2</sub>IrO<sub>3</sub>,” *Phys. Rev. Lett.*, vol. 110, no. 9, 2013, doi: 10.1103/PhysRevLett.110.097204.
- [69] D. Gotfryd, J. Rusnačko, K. Wohlfeld, G. Jackeli, J. Chaloupka, and A. M. Oleś, “Phase diagram and spin correlations of the Kitaev–Heisenberg model: Importance of quantum effects,” *Phys. Rev. B*, vol. 95, no. 2, pp. 46–49, 2017, doi: 10.1103/PhysRevB.95.024426.
- [70] X. Liu *et al.*, “Long-range magnetic ordering in Na<sub>2</sub>IrO<sub>3</sub>,” *Phys. Rev. B - Condens. Matter*

- Mater. Phys.*, vol. 83, no. 22, 2011, doi: 10.1103/PhysRevB.83.220403.
- [71] G. Binnig, H. Rohrer, C. Gerber, and E. Weibel, "Surface Studies by Scanning Tunneling Microscopy," *Phys. Rev. Lett.*, vol. 49, no. 57, 1982, doi: <https://doi.org/10.1103/PhysRevLett.49.57>.
- [72] G. Binnig and H. Rohrer, "Scanning Tunneling Microscopy - From Birth to Adolescence," *Nobelprize.org*, 1986.
- [73] I. Giaever, "Energy gap in superconductors measured by electron tunneling," *Phys. Rev. Lett.*, vol. 5, no. 4, pp. 147–148, 1960, doi: 10.1103/PhysRevLett.5.147.
- [74] A. Messiah, *Quantum Mechanics I*. New York: de Gruyter & Co., 1976.
- [75] J. Bardeen, "Tunneling from a many-particle point of view," *Phys. Rev.*, vol. 6, pp. 57–59, 1961, doi: <https://doi.org/10.1103/PhysRevLett.6.57>.
- [76] J. Tersoff and D. R. Hamann, "Theory of the scanning tunneling microscope," *Phys. Rev. B*, vol. 31, no. 2, pp. 805–813, 1985, doi: 10.1103/PhysRevB.31.805.
- [77] J. Chen, *Introduction to Scanning Tunneling Microscopy*. Oxford University Press, 1993.
- [78] D. Bonnell, *Scanning Probe Microscopy and Spectroscopy: Theory, Techniques, and Applications*, 2nd ed. Wiley-VCH, 2000.
- [79] R. J. Hamers, "Atomic-Resolution Surface Spectroscopy with the Scanning Tunneling Microscope," *Annu. Rev. Phys. Chem.*, vol. 40, pp. 531–559, 1989.
- [80] B. Voigtlaender, *Scanning Probe Microscopy*, 1st ed. Springer-Verlag Berlin Heidelberg, 2015.
- [81] R. M. Feenstra, "Tunneling spectroscopy of the GaAs(110) surface," *J. Vac. Sci. Technol. B Microelectron. Nanom. Struct.*, vol. 5, no. 4, p. 923, 1987, doi: 10.1116/1.583691.
- [82] J. K. Garleff, M. Wenderoth, K. Sauthoff, R. G. Ulbrich, and M. Rohlfing, "2 X 1 reconstructed Si(111) surface: STM experiments versus ab initio calculations," *Phys. Rev. B - Condens. Matter Mater. Phys.*, vol. 70, no. 24, pp. 1–7, 2004, doi: 10.1103/PhysRevB.70.245424.
- [83] K. Besocke, "An easily operable scanning tunneling microscope," *Surf. Sci.*, vol. 181, no. 1–2, pp. 145–153, 1987, doi: 10.1016/0039-6028(87)90151-8.
- [84] K. Sauthof, "Rastertunnelspektroskopie an einzelnen Donatoren und Donatorkomplexen nahe der GaAs(110)-Oberfläche.," Georg-August University Goettingen, 2003.
- [85] G. J. de Raad, "Voltage-Dependent Scanning Tunneling Microscopy on the (110)- surfaces of GaAs, AlGaAs, and their heterostructures," Eindhoven University of Technology, 2001.
- [86] H. Schleiermacher, "Charakterisierung von Spitzen für das Rastertunnelmikroskop," Georg-August-University Goettingen, Diplomarbeit, 2003.
- [87] M. A. Rosentreter, "Rastertunnelmikroskopie auf der GaAs(110)-Oberfläche bei Temperaturen von 8 K - 300 K," Georg-August-University Göttingen, PhD Thesis, 1997.
- [88] A. Weismann, "Scanning Tunneling Spectroscopy of Subsurface Magnetic Atoms in Copper Electron Focusing and Kondo Effect," Georg-August-University Göttingen, PhD Thesis, 2008.
- [89] R. Y. Umetsu, R. Tu, and T. Goto, "Thermal and electrical transport properties of zr-based bulk metallic glassy alloys with high glass-forming ability," *Mater. Trans.*, vol. 53, no. 10, pp. 1721–1725, 2012, doi: 10.2320/matertrans.M2012163.
- [90] S. Hunklinger, *Festkörperphysik*, 5th ed. de Gruyter Oldenbourg, 2018.

- [91] S. Nakatsuji, V. Dobrosavljević, D. Tanasković, M. Minakata, H. Fukazawa, and Y. Maeno, "Mechanism of hopping transport in disordered mott insulators," *Phys. Rev. Lett.*, vol. 93, no. 14, 2004, doi: 10.1103/PhysRevLett.93.146401.
- [92] R. Gross and A. Marx, *Festkörperphysik*, 2nd ed. Oldenbourg, 2014.
- [93] R. A. Abram, G. J. Rees, and B. L. H. Wilson, "Heavily doped semiconductor devices," *Adv. Phys.*, vol. 27, no. 6, pp. 799–892, 1978.
- [94] G. D. Mahan and J. W. Conley, "The density of states in metal-semiconductor tunneling," *Appl. Phys. Lett.*, vol. 11, pp. 29–31, 1967, doi: 10.1080/14786436008241201.
- [95] F. Cyrot-Lackmann and J. P. Gaspard, "On the electronic structure of an impurity band: A cumulant approach," *J. Phys. C Solid State Phys.*, vol. 7, no. 10, pp. 1829–1839, 1974, doi: 10.1088/0022-3719/7/10/010.
- [96] P. W. Chapman, O. N. Tufte, J. D. Zook, and D. Long, "Electrical Properties of Heavily Doped Silicon," *J. Appl. Phys.*, vol. 34, no. 11, pp. 3291–3295, 1963.
- [97] C. Guan and X. Guan, "A brief introduction to Anderson Localization." Department of Physics, Massachusetts Institute of Technology, 2019, [Online]. Available: <https://web.mit.edu/8.334/www/grades/projects/projects19/GuanChenguang.pdf>.
- [98] N. F. Mott and E. A. Davis, *Electronic processes in non-crystalline materials*, 2nd ed. Oxford: Oxford : Clarendon Press, 1979.
- [99] P. W. Anderson, "Absence of Diffusion in Certain Random Lattices," *Phys. Rev.*, vol. 109, p. 1492, 1958.
- [100] A. Lagendijk, B. van Tiggelen, and D. S. Wiersma, "Fifty years of Anderson localization," *Phys. Today*, vol. 62, no. 8, 2009.
- [101] A. Aspect and M. Inguscio, "Anderson localization of ultracold atoms," *Phys. Today*, vol. 62, no. 8, pp. 30–35, 2009, doi: 10.1063/1.3206092.
- [102] N. F. Mott, "Conduction in glasses containing transition metal ions," *J. Non. Cryst. Solids*, vol. 1, no. 1, pp. 1–17, 1968, doi: 10.1016/0022-3093(68)90002-1.
- [103] M. Pollak, "A percolation treatment of dc hopping conduction," *J. Non. Cryst. Solids*, vol. 11, no. 1, pp. 1–24, 1972, doi: 10.1016/0022-3093(72)90304-3.
- [104] B. Shklovskii and A. Éfros, "Impurity Band and Conductivity of Compensated Semiconductors," *J. Exp. Theor. Phys.*, vol. 33, no. 2, p. 468, 1971.
- [105] V. K. S. Shante and S. Kirkpatrick, *An introduction to percolation theory*, vol. 20, no. 85. 1971.
- [106] A. B. Pinto, "Structural, magnetic and electrical transport properties of GaN-based magnetic semiconductors and hybrid structures," Georg-August-University, PhD Thesis, 2010.
- [107] K. J. Hayden and P. N. Butcher, "Analysis of hopping conduction in impurity bands in inversion layers," *Philos. Mag. B Phys. Condens. Matter; Stat. Mech. Electron. Opt. Magn. Prop.*, vol. 38, no. 6, pp. 603–617, 1978, doi: 10.1080/13642817808246337.
- [108] A. S. Skal, B. I. Shklovskii, and A. L. Efros, "Activation energy of hopping conduction," *Sov. Phys. Solid State*, vol. 17, no. 2, pp. 316–320, 1975.
- [109] A. S. Skal and B. I. Shklovskii, "Mott equation for low temperature edge conductivity," *Sov. Phys. Solid State*, vol. 67, p. 1820, 1971.
- [110] D. Ovchinnikov, A. Allain, Y.-S. Huang, D. Dumcenco, and A. Kis, "Electrical Transport



- Properties of Single-Layer WS<sub>2</sub>,” *Phys. Rev. B - Condens. Matter Mater. Phys.*, vol. 90, no. 15, pp. 8174–8181, 2014, doi: <https://doi.org/10.1021/nn502362b>.
- [111] S. D. Baranovskii, A. L. Efros, B. L. Gelmont, and B. I. Shklovskii, “Coulomb gap in disordered systems: Computer simulation,” *Solid State Commun.*, vol. 27, no. 1, pp. 1–3, 1978, doi: 10.1016/0038-1098(78)91038-4.
- [112] A. L. Efros, Nguyen Van Lien, and B. I. Shklovskii, “Impurity band structure in lightly doped semiconductors,” *J. Phys. C Solid State Phys.*, vol. 12, no. 10, pp. 1869–1881, 1979, doi: 10.1088/0022-3719/12/10/018.
- [113] D. Joung and S. I. Khondaker, “Efros-Shklovskii variable-range hopping in reduced graphene oxide sheets of varying carbon fraction,” *Phys. Rev. B*, vol. 86, no. 23, p. 235423, 2012, [Online]. Available: <http://arxiv.org/abs/1210.1876> <http://link.aps.org/doi/10.1103/PhysRevB.86.235423>.
- [114] X. Qi and S. Zhang, “The quantum spin Hall effect and topological insulators,” *Phys. Today*, vol. 63, no. 1, p. 33, 2010, doi: 10.1063/1.3293411.
- [115] L. Fu, C. L. Kane, and E. J. Mele, “Topological insulators in three dimensions,” *Phys. Rev. Lett.*, vol. 98, no. 10, 2007, doi: 10.1103/PhysRevLett.98.106803.
- [116] J. E. Moore and L. Balents, “Topological invariants of time-reversal-invariant band structures,” *Phys. Rev. B - Condens. Matter Mater. Phys.*, vol. 75, no. 12, pp. 3–6, 2007, doi: 10.1103/PhysRevB.75.121306.
- [117] R. Roy, “Topological phases and the quantum spin Hall effect in three dimensions,” *Phys. Rev. B - Condens. Matter Mater. Phys.*, vol. 79, no. 19, 2009, doi: 10.1103/PhysRevB.79.195322.
- [118] D. Hsieh *et al.*, “A tunable topological insulator in the spin helical Dirac transport regime,” *Nature*, vol. 460, no. 7259, pp. 1101–1105, 2009, doi: 10.1038/nature08234.
- [119] P. Roushan *et al.*, “Topological surface states protected from backscattering by chiral spin texture,” *Nature*, vol. 460, pp. 1106–1109, 2009, doi: 10.1038/nature08308.
- [120] C. H. Sohn *et al.*, “Mixing between  $J_{eff}=1/2$  and  $3/2$  orbitals in Na<sub>2</sub>IrO<sub>3</sub>: A spectroscopic and density functional calculation study,” *Phys. Rev. B - Condens. Matter Mater. Phys.*, vol. 88, no. 8, 2013, doi: 10.1103/PhysRevB.88.085125.
- [121] K. P. O’Donnell and X. Chen, “Temperature dependence of semiconductor band gaps,” *Appl. Phys. Lett.*, vol. 58, no. 25, pp. 2924–2926, 1991, doi: 10.1063/1.104723.
- [122] Z. Wang *et al.*, “Disorder induced power-law gaps in an insulator-metal Mott transition,” *Proc. Natl. Acad. Sci. U. S. A.*, vol. 115, no. 44, pp. 11198–11202, 2018, doi: 10.1073/pnas.1808056115.
- [123] I. Battisti *et al.*, “Universality of pseudogap and emergent order in lightly doped Mott insulators,” *Nat. Phys.*, vol. 13, no. 1, pp. 21–25, 2017, doi: 10.1038/nphys3894.
- [124] M. Z. Hasan and C. L. Kane, “Colloquium: Topological insulators,” *Rev. Mod. Phys.*, vol. 82, no. 4, pp. 3045–3067, 2010, doi: 10.1103/RevModPhys.82.3045.
- [125] P. Kloth, “Optical Excitation in Scanning Tunneling Microscopy: From Surface Photovoltages to Charge Dynamics on the Atomic Scale,” Georg-August-Universität Göttingen, PhD Thesis, 2016.
- [126] P. Kloth, T. Thias, O. Bunjes, J. Von Der Haar, and M. Wenderoth, “A versatile implementation of pulsed optical excitation in scanning tunneling microscopy,” *Rev. Sci. Instrum.*, vol. 87, no. 12, 2016, doi: 10.1063/1.4971189.

- [127] S. Maamar, “Anzeichen für Leitfähigkeit von Natriumiridatspaltflächen im UHV,” Georg-August University Göttingen, Bachelor Thesis, 2018.
- [128] S. Hasegawa *et al.*, “Direct measurement of surface-state conductance by microscopic four-point probe method,” *J. Phys. Condens. Matter*, vol. 14, no. 35, pp. 8379–8392, 2002, doi: 10.1088/0953-8984/14/35/309.
- [129] A. Sinterhauf *et al.*, “Substrate induced nanoscale resistance variation in epitaxial graphene,” *Nat. Commun.*, vol. 11, no. 1, pp. 1–9, 2020, doi: 10.1038/s41467-019-14192-0.

## 11 Danksagung

Zum Schluss möchte ich mich herzlich bei allen bedanken, die zum Gelingen der Promotion beigetragen haben und mit tatkräftiger Unterstützung halfen.

Als erstes danke ich PD Dr. Martin Wenderoth, der mir die Teilnahme an diesem Promotionsprojekt ermöglichte. Vielen Dank für die zahllosen Diskussionen, Erklärungen und Ideen, die dieses Projekt maßgeblich nach vorne gebracht haben. Als ich 2016 anfangs sagte Martin mir, dass er sich vor allem als Sparringspartner sehe. In den fünf Jahren im Ring habe ich viel gelernt und freute mich festzustellen, dass unser Schlagabtausch im Ring blieb und nie das Zwischenmenschliche beeinträchtigt hat. Auch danken möchte ich für Verständnis und Unterstützung in schwierigen Zeiten, womit nicht nur die Arbeit am Projekt, sondern auch die Vereinbarkeit mit dem Privatleben wunderbar funktionierten.

Weiterhin gilt mein Dank Prof. Dr. Gegenwart für die vielen guten und substanziellen Diskussionen rund um die Iridate und die Kooperation im Projekt. Dies gilt ebenso für die Unterstützung bei der gemeinsamen Veröffentlichung. Auch gilt mein Dank Prof. Dr. Stefan Mathias für die Übernahme des zweiten Gutachtens und anregender Diskussionen in den TAC-meetings. Außerdem danke ich Prof. Dr. Michael Seibt, Prof. Dr. Hans-Christian Hofsäss und PD Dr. Salvatore Manmana für die Bereitschaft, in meiner Prüfungskommission mitzuwirken.

Als nächstes möchte ich Ina-Marie Pietsch danken, die gemeinsam mit mir das Projekt betreut und bearbeitet hat. Vielen Dank für die Synthetisierung und Charakterisierung der Proben, ein offenes Ohr und viele schöne Gespräche. In diesem Zusammenhang danke ich auch Pascal Spreckelsen, Sarah Maamar, Hendrik Wrigge und Máté Stark für eure Tatkraft, Initiative bei den Abschlussarbeiten sowie die Freude, den wir zusammen hatten.

Besonders danken möchte ich allen Mitgliedern und Ehemaligen der AG Wenderoth. Es war eine schöne Zeit, mit klasse Atmosphäre und Spaß bei der Arbeit. Danke für die großartige Hilfsbereitschaft, die Kaffeepausen, die Gespräche rund um die Physik und alle anderen Themen der Welt. Am einfachsten zusammengefasst: danke für eure Freundschaft.

Ein besonderer Dank gilt Bernhard Spicher sowie dem ganzen technischen Support. Das Projekt beinhaltete den Bau und die Inbetriebnahme zahlreicher Anlagen und Bauteile. Vielen Dank für die Unterstützung dabei sowie die Geduld mit mir.

Dem unermüdlichen Dr. Jörg Malindretos möchte ich danken für den IT support und das offene Ohr. Gerade in Pandemiezeiten war das Gold wert.

Zum Schluss möchte ich noch meiner Frau Miriam und meiner Familie danken, die immer Geduld bewiesen, auch wenn der Feierabend mal in die Nacht rückte. Für all die bedingungslose Unterstützung: vielen Dank!

## 12 Curriculum Vitae

### Thomas Dziuba

Date of Birth: April 28<sup>th</sup>, 1988

Place of Birth: Gehrden

Nationality: German

### Academic Education

Since 11/2016 **PhD student**

Georg-August-Universität Göttingen, IV. Physikalisches Institut

Project: Probing predicted topological surface states of correlated transition-metal oxides

Supervisor: PD Dr. Martin Wenderoth

2014 – 2016 **Master of Science in Physics**

Georg-August-Universität Göttingen, I. Physikalisches Institut

Thesis: Lokale mechanische Eigenschaften von ultrastabilen metallischen Gläsern

Supervisor: Prof. Dr. Konrad Samwer

2011 – 2014 **Bachelor of Science in Physics**

Gottfried Wilhelm Leibniz Universität Hannover, Institut für Festkörperphysik, Abteilung Atomare und Molekulare Strukturen

Thesis: Aufbau eines Feldionenmikroskopes

Supervisor: Prof. Dr. Herbert Pfnür

### Publications:

T. Dziuba, Y. Luo, K. Samwer. *Local mechanical properties of an ultrastable metallic glass*, J. Phys.: Condens. Matter **32**, 345101 (2020)

T. Dziuba, I.-M. Pietsch, M. Stark, G. A. Traeger, P. Gegenwart, M. Wenderoth. *Surface Conductivity of the Honeycomb Spin–Orbit Mott Insulator  $\text{Na}_2\text{IrO}_3$* . physica status solidi (b), **258**, 1, 2000421 (2021).

## Presentations

T. Dziuba, M. Stark, I. Pietsch, P. Gegenwart, M. Wenderoth. *Unconventional Surface Conductivity in Correlated Honeycomb Transition Metal Oxide Mott Insulators*. DPG: SurfaceScience 2021, Online Conference

T. Dziuba, I. Pietsch, G. Traeger, F. Lüpke, P. Gegenwart, M. Wenderoth. *Surface Conductivity of the Correlated Oxide Honeycomb Alkali Metal Iridates*. SPP1666 Workshop – Abschlussmeeting, Berlin, 2019

T. Dziuba, I. Pietsch, P. Gegenwart, M. Wenderoth. *Investigation of honeycomb  $\text{Na}_2\text{IrO}_3$  surface structures by functionalized STM and STS probes*. 8<sup>th</sup> International Conference on Scanning Probe Spectroscopy (SPS), Hamburg, Germany, 2019

T. Dziuba, I. Pietsch, P. Gegenwart, M. Wenderoth. *Investigation of honeycomb  $\text{Na}_2\text{IrO}_3$  surface structures by functionalized STM and STS probes*. DPG Spring Meeting, Regensburg, Germany, 2019

T. Dziuba, F. Lüpke, F. Freund, S. Manni, P. Gegenwart, M. Wenderoth. *Investigation of Honeycomb-Iridate Surfaces by Means of STM and STS*. DPG Spring Meeting, Berlin, Germany, 2018

T. Dziuba, *Investigation of sodium iridate surfaces by means of STM and STS*. 654<sup>th</sup> Wilhelm-Else-Heraeus Seminar “Topological Insights into Nanoscience using Scanning Probes”, Bad Honnef, 2017

T. Dziuba, Y. Luo, K. Samwer. *Local mechanical properties of ultrastable metallic glass*. DPG Spring Meeting, Dresden, Germany, 2017